Analytical and Numerical Study of Plug Flow Inside Round/Concentric Microchannels

by

Yadi Cao

B. Eng., University of Science and Technology of China, 2016

A THESIS SUBMITTED IN PARTIAL FULFILLMENT OF
THE REQUIREMENTS FOR THE DEGREE OF

MASTER OF APPLIED SCIENCE

in

THE COLLEGE OF GRADUATE STUDIES

(Mechanical Engineering)

THE UNIVERSITY OF BRITISH COLUMBIA

(Okanagan)

September 2018

The following individuals certify that they have read, and recommend to the College of Graduate Studies for acceptance, a thesis entitled:

Analytical and Numerical Study of Plug Flow Inside Round/Concentric Microchannels

submitted by Yadi Cao in partial fulfillment of the requirements for the degree of Master of Applied Science in Mechanical Engineering

Dr. Sunny Ri Li, School of Engineering

Supervisor

Dr. Joshua Brinkerhoff, School of Engineering

Supervisory Committee Member

Dr. Clarie Yu Yan, School of Engineering

Supervisory Committee Member

Dr. Kenneth Chau, School of Engineering

University Examiner

Abstract

Plug flow can generate recirculating flow between interfaces of immiscible fluids. Depending on the phase used to segment flow, it can be gas-liquid plug flow or liquid-liquid plug flow. The recirculating flow can enhance heat transfer as compared to the continuous pipe flow, especially in the laminar regime such as the microchannel flow. The present work focuses on the flow and heat transfer of liquid plugs with low Reynolds numbers.

The flow is modeled by applying Stokes simplification, and the solution is obtained by solving fourth-order partial differential equation sets. Solutions of two types of plug flow are obtained: 1) the gas-liquid plug flow in the concentric microchannel; 2) the liquid-liquid plug flow in the circular microchannel. For the gas-liquid plug flow study, the flow patterns inside the liquid phase including the volume ratio of the inner and outer vortexes, the ratio of maximum-to-minimum stream functions, the averaged recirculation flux as well as the skin friction coefficient are investigated in details. Correlations for predicting the maximum and minimum of the stream function are developed. For the liquid-liquid plug flow study, the influences of plug lengths and the viscosity ratio upon the cap vortexes and the overall skin friction coefficient are studied in details.

The heat transfer of the gas-liquid plug flow in the concentric microchannel is simulated numerically in MATLAB. Three types of thermal boundary conditions are investigated. The developing process of the thermal field can be explained using a simple thermal network for each boundary condition. The influences of parameters including the plug aspect ratio, the channel inner-outer radius ratio and the Peclect number upon the thermal conductance and heat transfer enhancement to the single-phase flow are investigated systematically. Then a simplified model for the fully developed thermal field is extracted for the quick calculation need in the design work. The results obtained from about 12,000 cases form a database that can be used in the future design work of heat exchanger based upon this kind of flow.

Lay Summary

Plug flows can enhance the heat transfer inside the microchannels by generating recirculating flow between interfaces of immiscible fluids. In this thesis, the analytical solutions of the two kinds of plug flow are obtained, and the physics behind it is revealed. The flow field results are used in heat transfer simulation under a wide range of working conditions. The obtained database of both flow field and heat transfer results can help the design work of heat exchanger based on this configuration in the future.

Preface

The work outlined in this thesis was conducted by Yadi Cao under the supervision of Dr. Sunny Ri Li. It was supported by Natural Sciences and Engineering Research Council of Canada (NSERC). All the presented research work was finished in the Thermal Management and Multiphase Flows Laboratory in the School of Engineering at the University of British Columbia (Okanagan campus). Portions of this thesis have been published in journals as well as in conference proceedings.

- A part of chapter 2 has been published as a proceeding at a conference. Cao, Y.D., Li, R. Liquid Plug in Gas Flow in Annular Channel. *3rd American Society of Thermal and Fluids Engineers, Mar. 2018. (TFEC-2018-24337).*

- A part of chapter 2 has been accepted by the Physics of fluids. Cao, Y.D., Li, R. A Liquid Plug Moving in an Annular Pipe – Flow Analysis. *Physics of fluids. Jul. 2018. (POF18-AR-01493R).*

Table of Contents

List of Tables

List of Figures

List of Symbols

Symbols	Definitions
Parameters	
α	thermal diffusivity
β	aspect ratio ratio (eq. (2.11))
C	capacity for extensive properties
C_f	skin friction coefficient (eq. (2.32))
c_p	specific heat
D_h	hydraulic diameter
η	inner-outer radius ratio (eq. (2.11))
F_f	friction force (eq. (2.29))
γ	mixing index (eq. (3.24))
k	thermal conductivity
l	length, characteristic length (eq. (1.3))
λ	surface tension
μ	dynamic viscosity
P	static pressure
ψ	stream function
Q	heat flow
q''	heat flux
R_c	radius of curvature
ρ	density
σ	thermal conductance (eqs. (3.25) and (3.26))
t	time

u, $\boldsymbol{u}$, U	velocity scalar, velocity vector, plug moving/mean velocity
V	volume
z, r	axial index, radial index

Popular dimensionless parameters

Ca	Capillary number (eq. (2.1))
De	Dean number (eq. (1.2))
Ec	Eckert number (eq. (3.2))
f	Fanning friction factor (eq. (2.31))
Nu	Nusselt number (eq. (3.32))
Pe	Peclet number (eq. (3.10))
Pr	Prandtl number (eq. (1.4))
Re	Reynolds number (eq. (1.1))
We	Weber number (eq. (1.3))

Special values and coefficients

A, B, C, D, E, F	constant coefficients
ω, χ	eigenvalues

Special functions and operators

Δ	difference operator
$\mathcal{H}$	finite Hankel transformation (eq. (4.13))
I	modified Bessel function of the first
J	Bessel function of the first kind
K	modified Bessel function of the second kind
$\mathcal{L}_{-1}$	a linear operator (eq. (2.6))
∇	Nabla operator
∇^2	Laplace operator
$\mathcal{S}$	finite Fourier transformation (eq. (2.16))

Superscripts

$\hat{}$	dimensionless value
$\bar{}$	averaged value (eq. (3.23))

Subscripts

cap	(for) cap vortexes (inside plug)
f	fluid (eqs. (3.25) and (3.26)) or frictional (eq. (2.29))
i, j	makers for phases in chapter 4 ($i, j = 1, 2 \wedge i \neq j$)
in, out	(at) inner side, (at) outer side
l, m, n	series number
$plug$	(for) plug
rec	(for) recirculation (inside plug)
sp, $1D$	(for) single phased flow, (for) 1 dimensional flow
std	a standard value (for nondimensionalization)
w, v	(of) wall, (of) vortex

Acknowledgments

I gratefully appreciate the patient guidance from Dr. Ri Li.

The project is fully funded by the Natural Sciences and Engineering Research Council (NSERC).

I would also like to especially thank Dr. Xuan Gao for providing the initial motivation for the subject of this thesis.

It is an honor to have Dr. Joshua Brinkerhoff and Dr. Yu Yan as the committee members. Their advice during the annual report helped optimize this work.

Dedication

To the great love and the unconditional support from my parents.

Chapter 1

Introduction

1.1 Background

Driven by the fast development of applications including microelectronics,micro-reactors, micro-electro-mechanical systems(MEMS), the study of microfluidics has drawn much attention in recent years [5]. The applications of microfluidics includes environmental detection [6], chemical reaction [7–9], and drug delivery [10]. Despite the efficiency brought by MEMS and microfluidics, one of the biggest challenges faced by engineers is the heat generation in these devices. Traditional cooling methods have faced challenges owing to increasing heat flux and thermal resistance caused by the complicated internal structure of micro-size systems. Thus, the large heat flux removal methods for these devices have gained much attention in recent years [11]. Many modifications of traditional heat transfer methods have been done to suit the requirement of micro-sized systems. These modified methods include spray cooling [12–14], jet impingement cooling [15], falling film cooling [16] and heat pipes [17]. However, it has been pointed out that these methods are neither easily controllable nor cost-friendly [11, 18]. Other alternatives are needed for low-cost cooling methods.

The heat exchanger using microchannels has the advantage of small volume and large surface-volume ratio because of the small scale [19]. It also can be parallel configured and packaged to cooling capacity. Tuckerman and Pease [20] introduced the concept of the microchannel heat exchanger and they found out the heat removal limit for single phase flow was $0.79\,\mathrm{kW/cm^2}$. However, this limit is relatively lower comparing to the heat flux of current super-powered computing chips [21–23]. New efficient methods are needed for thermal design need in the future.

The heat transfer limit in the work of Tuckerman and Pease [20] can be explained using low Reynolds number (Re) (defined below) in microchannels. The Reynolds number (Re) is often used to determine the flow patterns in different situations, and it is defined using the ratio of inertial force and viscous force. In the case of internal flow, it can be written as below

$$\mathrm{Re} = \frac{\rho D_h U}{\mu}, \tag{1.1}$$

where ρ is the density of the fluid, D_h is the hydraulic diameter of the channel, and U is the mean velocity of the fluid, and μ is the dynamic viscosity of the fluid.

In microchannel, it requires extremely high pumping power to make Re high enough ($\sim 2,000$) to reach the turbulent regime owing to the small scale of D_h. Thus the laminar flow is often preferred, and heat transfer will be limited by the thermal diffusion process if there is no vortex inside to disturb the flow field. Since the extensive quantities like energy can be transported with flowing fluid, the mixing process including heat transfer can be enhanced by vortexes which disturb the flow field. Lots of previous studies have been focusing on generating vortexes inside single-phase flow. Another alternative, which has also gained attention, is to involve flow boiling inside the microchannel to make full use of the latent heat. In the next section, previous works related to both the options mentioned above will be reviewed.

1.2 Challenges faced by cooling in microchannel

Most studies have been aiming to generate vortexes in the single-phase flow by either putting vortex promoters or varying geometries of the channel. However, their studies still require quite high Re ($100 \sim 5,600$) in order to generate strong vortexes and have an apparent heat transfer enhancement. Hence, these methods will face a similar challenge of extremely high pumping power as triggering turbulent flow in microchannel does. Thus the application of these methods can be limited. The reviews of some selected works related to the above methods are presented below.

Vortex generators are obstacles with different geometry in the channel, and they can produce transverse flow due to flow separation on the interface between the obstacles and the fluid. In the numerical study of Meis, Varas, Velazquez, and Vega[24], obstacles with different shapes and orientations were installed inside a microchannel as vortex promoters. The Reynolds number required in their work above vary within $600 \sim 1,200$, and this design has a slightly higher heat transfer enhancement than pumping power penalty. In the experimental study of Wang, Houshmand, Elcock and Peles [25], Wang, Nayebzadeh, Yu, Shin and Peles[26], micropillar of different shapes/pin fins were put into the microchannel, respectively. The micro particle image velocimetry (μPIV) technique was used to observe flow structure downstream of a pillar, while resistance temperature detector (RTD) was used to measure the spatially averaged temperature. The triangular pillar has the best enhancement with Nusselt number vary within $17.7 \sim 88.9$, while the corresponding range for Reynolds number is $100 \sim 5,600$ in order to generate vortexes in the downstream of the pillar. Nevertheless, they do not include information about pressure loss.

Another way of introducing vortexes is by making the channel curved to obtain Dean vortexes. Dean vortexes are a kind of secondary flows (which always appear in a pair of counter-rotating vortexes) generated by the imbalance between centrifugal forces and radial pressure [27]. The dimensionless Dean number (De) can be used to describe the strength of Dean vortexes. It is defined as below

$$\mathrm{De} = \mathrm{Re}\sqrt{\frac{D_h}{2R_c}}, \tag{1.2}$$

where Re is the Reynolds number, D_h is the hydraulic diameter, and R_c is the radius of curvature of the path of the channel.

In the numerical studies of Sui, Teo, Lee, Chew, and Shu[28], wavy channel shapes were applied to generate Dean vortexes inside the microchannel. The Reynolds number required in these two works is within $100 \sim 400$ and $300 \sim 650$ respectively. The enhancement in Nusselt number is about $1.67 \sim 2.02$ times depending on the tunnel shape, while the pressure loss penalty is slightly lower than the heat transfer enhancement. In the numerical study of Xia, Jiang, Wang, Zhai, and Ma[29], besides applying wavy channel, reentrant cavities at the wall were added to provide more heat transfer area. Nevertheless that the drag area increased simultaneously, and the authors did not mention the efficiency of add-on cavities. Chai, Xia, Wang, Zhou, and Cui[30] investigated both numerically and experimentally the flow heat transfer inside microchannels with periodically expansion-constriction cross-sections. The interval for Re in their work is within $300 \sim 750$, and the Nusselt number can be enhanced by up to 180%, they did not provide details about pressure loss as well.

Experimental studies about flow in microchannel involving boiling have also been carried out in recent years due to the considerable latent heat of fluid. Despite many applications of cooling with phase change in electronics, the physics behind phase change is not clear, which leads to high complexity to flow control [18]. The reviews of selected works related to above are presented below.

The heat removal in a mini-channel can be as high as $10\,\mathrm{kW/cm^2}$ [31], where DI (deionized) water was used and the mass flow rate is $5,000 \sim 134,000\,\mathrm{kg/m^2s^{-1}}$. However, in the microchannel, the mass flow rate is much lower, and the critical heat flux (CHF) usually cannot reach this ultra high value. In the work of Deng, Wan, Qin, Zhang and Chu[32], Krishnamurthy and Peles[33], structured microchannel with micro pin fins (SM-MPF) were fabricated using a laser micro-milling method. Lots of tiny reentrant cavities increase nucleation site density (the number of sites where nucleation happens in a given area) for boiling. The mass flow rate is $200 \sim 300\,\mathrm{kg/m^2s^{-1}}$ and CHF can be $0.01 \sim 0.11\,\mathrm{kW/cm^2}$, which results in $10\% \sim 175\%$ enhancement comparing to flow boiling in straight microchannel depending on working liquids. Liu, Li, Liu and Gau[34] and Choi, Shin, Yu and Kim[35] investigated the influence of wettability of the wall upon boiling in the microchannel and found out that the heat transfer in hydrophobic microchannels is higher than that in hydrophilic ones. In hydrophobic channels, the nucleation site density is observed to be higher, and more departure bubbles can disturb the flow field inside the liquid film, making the liquid film unstable and enhance the heat transfer. Jaikumar and Kandlikar[36] aligned nucleating regions with non-nucleating ones in the feeder microchannel to separate pathways for returning liquid and upward floating vapor. The separate pathways led the fluid to refill the boiling nucleation to hinder the dry-out and thus can enhance the boiling efficiency. They found out an optimal alignment for enhancement, and the critical heat flux can be $0.39\,\mathrm{kW/cm^2}$ under this alignment.

Overall, introducing vortexes in the single-phase flow has the requirement of high Re while the mechanism of flow boiling is still not well understood, which makes flow boiling hard to predict and control. Thus, stable multiphase flow without phase change is preferred for prediction and easier control [18]. Among all the multiphase flow types without phase change, the plug flow has drawn attention in recent years [37]. The simple introduction to plug flow and the vortexes inside is made below.

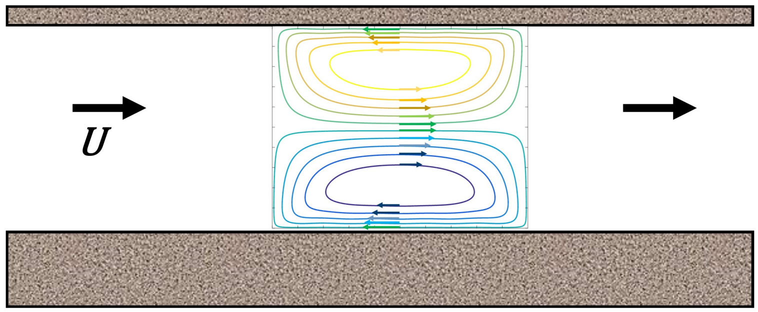

Figure 1.1: Schematic show for the recirculation in plug flow. The contour plot is from the results in chapter 2 in this thesis.

Plug flow is also called slug flow, Taylor flow or segmented flow, it is a flow structure where another kind of immiscible fluid segments the liquid into separate plugs. The liquid plug has a shape of plug and nearly takes all the cross-section of the channel [38]. In the reference sticking to a moving plug, the non-slip wall becomes a moving wall with a velocity in the transverse direction. The moving wall drives the fluid by viscous force, and then the flowing fluid bounces back at the interface at the rear end of the plug, then travels along the middle axial of the plug and bounces back again at the frontal end and finishes a circle of recirculation(fig. 1.1). Comparing to using vortex promoter or generating Dean vortexes, this method prefers the lower speed of the plug[39], and thus extremely high pumping power is not required. To explain this, a new dimensionless parameter, Weber number is written as below, where l is the characteristic length and λ is the surface tension,

$$\mathrm{We} = \frac{\rho\, u^2\, l}{\lambda}. \tag{1.3}$$

Weber number (We) represents the ratio between inertia and surface tension. When the velocity of the plug is small, We is small, and the interface tends to be more solid comparing to the momentum brought by the circulation, and thus the flow pattern inside tends to be more stable. Besides this advantage of not requiring high pumping power, plug flow also has the advantage of vortex size. Comparing to vortex promoters where vortexes are generated only after the obstacles, the vortexes in a liquid plug nearly takes up the whole cross-section [37] which indicates the possibility of better mixing ability.

1.3 Numerical/experimental studies of plug flow in microchannel

The heat transfer inside the plug flow has been investigated experimentally in the recent decades. In the experimental work of [40], Nitrogen gas was injected coaxially into DI (deionized) water for stable two-phase flow. The high-speed camera and thermocouples along the channel were used to measure the flow field and the temperature field respectively. The enhancement of the Nusselt number is 176% while the pressure loss penalty is around 22%. Though the intrusive thermocouples may disrupt the flow field and furthermore influence the heat transfer results. What is more, thermocouples can only collect the temperature at limited points instead of alongside the whole channel. Thus, the non-intrusive measuring technique that can collect data for an area is preferred.

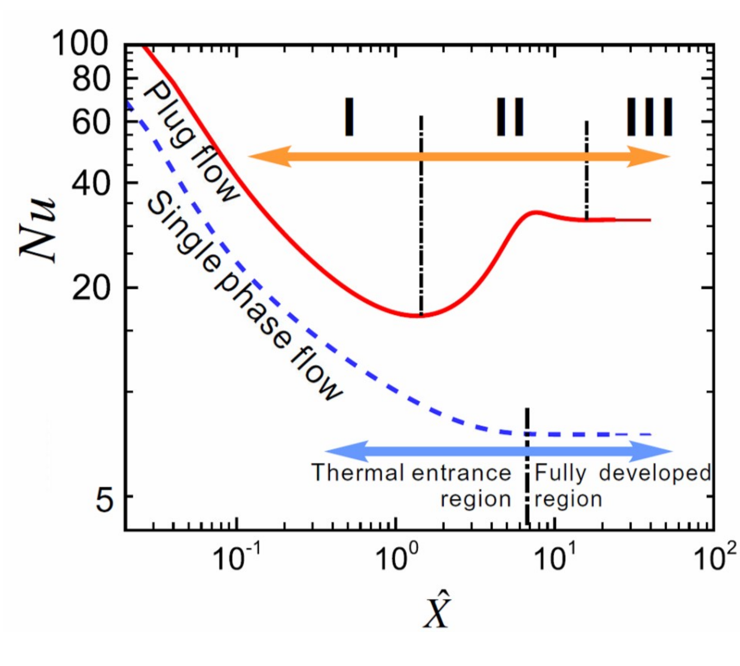

Figure 1.2: Schematic show for stages of the heat transfer of gas-liquid plug flow in a slit microchannel in [3]. For plug flow: (I) the thermal entrance region. (II) the transition region. (III) the fully developed region. For single-phase flow there is no transition region. Reprinted with permission.

A high-resolution infrared(IR) camera was used in [41] to collect the continuous temperature distribution of a stainless steel tube which contained plug flow inside. They found out the developing stages of the plug flow heat transfer with constant input heat flux can be summarized into following (also see the schematic show in fig. 1.2):

- In the entry region (about one plug length long), the Nusselt number for short or long plugs reaches the plug fully developed asymptotic limit, or the continuous flow limit respectively;
- In the transition region (about one period of internal circulation of the plug), Nusselt number oscillates for short plugs (validated in [3, 42]);
- In the fully developed stage, Nusselt number gradually becomes stable.

Despite their explicit reveal of the stages of plug flow heat transfer, the IR camera can only measure the surface temperature of the outer channel wall, the information inside for both flow and thermal field are missing.

The most precise optical measuring technique of the flow field to date is the micro particle image velocimetry (μPIV), and one can find literature reviews of visualization in microfluidics in the work of Wereley and Meinhart[43], Sinton[44]. The laser-induced fluorescence (LIF) method is ideal to measure the temperature field inside the flow field non-intrusively, which was adopted in the work of Ross, Gaitan and Locascio[45], Ghaini, Mescher, and Agar[1]. A third order polynomial correlation was set up to show the temperature distribution by the dye particle density in the microchannel, and the precision is about $2.5 \sim 3.4°C$ [45]. However, these optical methods meet challenges when the light tilts through the interfaces with different refractive indexes, which happens for curved channel walls [46]. The materials have to be chosen carefully to match the refraction coefficients in order to avoid the failure. To our best knowledge, there are very few investigations into plug flow heat transfer using both μPIV and LIF, and it could be a research point in the future.

A review for numerical work for the plug flow heat transfer are included in [47]. Most studies had focused on the plug flow heat transfer inside of circular [48, 49] or slit channels

[50–52], which can be a result of dramatically increasing the computational time when the field is unable to be simplified using symmetricity. Though, some works conducted in the 3-D domain also use techniques (such as the volume of fluid method, lattice Boltzmann method, level set method and moving grid method) to capture the interface between fluids [53–56]. Though these methods can capture details with high precision, the calculation time for them is too long. In the real design/optimization work where additional simulations besides the flow field will be conducted (for multiple times before finding out an optimum design), it is preferred using existing flow field results [3, 42, 57]or at least by pre-defining the interface shape [58] to save calculation time.

Despite many investigations of both gas-liquid and liquid-liquid plug flow heat transfer, it has been pointed out in the review works recently that significant gaps exist concerning both the measured values and the correlations for heat transfer coefficient and pressure drop between different pieces of literature, and there are little agreements among them [18, 47, 59]. The only scenario where some agreement is observed is the gas-liquid plug flow in the circular microchannel [59]. Most of the correlations did not reveal a clear picture for the physics of heat transfer, and were merely a collection of obtained results, and thus can not be applied when it exceeds their original conditions.

Since there still lacks reliable correlations for the plug flow heat transfer under various conditions, fast simulation and dense database can be an alternative. Unlike flow in macro size and under high speed, the Stokes simplification for slow viscous flow is very reliable because Reynolds number for plug flow is small ($\mathrm{Re} \ll 1$) in microchannel [38]. Thus, the only challenge of building up a dense database remains as calculation time. The normal procedure for simulating fluid flow heat transfer is by solving the flow field and thermal field simultaneously, which will result in a considerable amount of calculation time. Fortunately in the microchannel flow scenarios, the temperature difference does not need to be too much to reach a considerable temperature gradient owing to the small scale (i.e., the mean temperature difference between the inlet and the outlet is less than 9 K, the difference between the wall and the mean value is less than 2 K in [41]), the thermal properties can usually be assumed to be constant. If the Prandtl number (defined below, where k is thermal conductivity of the fluid) is large ($\mathrm{Pr} \gg 1$), the momentum diffusivity (ν) is much larger than thermal diffusivity (α), then the flow and thermal field can be decoupled to save calculation time [3, 42, 60].

$$\mathrm{Pr} = \frac{\nu}{\alpha} = \frac{c_p \mu}{k}. \tag{1.4}$$

Moreover, the analytical method can be applied in the microchannel with certain kinds of simple geometry to calculate the flow field with some simplifications, which has nearly no calculation time and therefore are preferred for building up the database. In the next section, a review of all existing analytical methods of plug flow in microchannels is prepared.

1.4 Analytical models of plug flows

The Graetz problem describes the steady-state heat transfer in fully developed internal flow, which implies the zero or the constant temperature derivative in the flow direction depending on boundary conditions. It applies the assumption of the constant thermal properties such as ρ, μ, k and c_p and incompressible Newtonian flow. This model has been applied in studying plug flow heat transfer, and the literature related will be presented below.

In the work of Shojaeian and Kosar [61, 62], a simple analytical model was adopted based on the Graetz problem while the velocity in the channel is assumed to be constant and uniform. Muzychka, Walsh, and Walsh [63] also made full of the Graetz problem by assuming the velocity is constant and uniform. They managed to conclude the influence of tunnel geometries by extracting a few key parameters of the cross-section shape. These methods could help estimate the heat transfer performance roughly. However, the assumption of uniform and constant velocity field drops the recirculation inside the plug and can highly underestimate the mixing ability of plug flow. A better way is to consider the vortexes formed inside plugs by modeling and solving the flow field in the 2-D cross-section.

In order to analytically obtain the vortex inside plugs, the Stokes flow assumption, which implies Reynolds number is very small ($\mathrm{Re} \ll 1$) and drops the convection of the momentum, was firstly used in gas-liquid plug flows by Sivasamy, Che, Wong, Nguyen, and Yobas [38]. In their work, the 2-D flow field was built and analytically solved using a fourth order partial differential equation set (PDEs). This model has been proved to be effective and convenient in microchannels with different shapes, such as in a slit microchannel [38], in a curved microchannel [64], and in a microchannel with circular cross-section [2]. Some numerical studies of heat transfer based upon the analytical flow field were carried out [3, 42], and the flow field results helped to understand the mechanism behind the heat transfer enhancement. The analytical model for the liquid plug train in a 2-D channel was proposed in [57]. The basic idea is the same as the gas-liquid plug flow in [38], though the friction force between two immiscible liquids increased the complexity on the interface. One of the simplified results of the liquid plug train, the liquid-liquid plug flow, was applied for the study of heat transfer performance for liquid-liquid plugs at asymmetric boundary conditions in [60].

1.5 Motivation and Objective

This thesis analytically and numerically studies the plug flow and heat transfer of this flow type.

With the fast developing of applications such as MEMS, the size of these devices shrinks dramatically, and the heat flux also increases considerably. Traditional flow cooling methods, which usually generate vortexes in turbulent flow regime, have faced the challenge brought by small characteristic length and small Reynolds number under micro scales. The plug flow shows promising potential for enhancing heat transfer because it can generate well-defined vortexes even in the Stokes regime ($\mathrm{Re} \ll 1$) resulting from the interface between another kind of immiscible fluid. Hence, plug flow based heat exchanger can be a solution to the future thermal management in MEMS. However, according to the previous section, there still lacks the analytical studies of plug flow in microchannels with many other kinds of geometry. For instance, one of the most commonly seen geometry in the traditional heat exchanger, the concentric tube, is not studied before. Moreover, in the previous studies, heat transfer simulations were mostly conducted using the transient method which leads to a quite long calculation time even provided with pre-stored flow field results and makes it hard and costly to build/extend the database.

Thus, the most primary objective of this thesis is to find the analytical solutions of plug flow in different geometries that people have not studied. The analytical flow field results can help understand the mechanism of heat transfer enhancement. The second objective is to systematically investigate the heat transfer within plug flows in these geometries, as well as the influences of geometrical parameters or other parameters upon the heat transfer performance. At last, optimally a simplified heat transfer model can be extracted to save calculation time so that I can build up a database/an empirical correlation to cover a massive amount of working conditions in an acceptable amount of time. The pre-stored database/pre-defined correlation can help the optimization without the need of running simulations for multiple times by the designers. Only a few times of accurate simulation are needed for calibration after they have found the optimal designs.

1.6 Organization of the Thesis

In chapter 2, I find the analytical solution of gas-liquid plug flow inside the concentric microchannel. The flow patterns like locations of vortex center, the stream functions of vortex centers, the radial transport velocity and recirculation period are investigated. The pumping power in the form of skin friction coefficient is studied.

In chapter 3, I carry out the heat transfer simulations in plug flow in chapter 2 at three different kinds of commonly seen asymmetric boundary conditions: The inner iso-flux boundaries (shorten as IFB), the iso-thermal boundaries (shorten as ITB), and the outer iso-flux boundaries (shorten as OFB). Simplified thermal networks for these heat transfer processes are extracted. The influences of plug aspect ratio, the inner-outer radius ratio as well as Peclect number upon heat transfer enhancement are analyzed. Finally, in this chapter, a simplified model for heat transfer at the fully developed stage is found to save calculation time. An extensive database containing results from about 12,000 working conditions are built up for future design work.

In chapter 4, I find the analytical solution of liquid-liquid plug flow inside microchannel with a round cross-section by modeling and solving the flow field in two immiscible fluids simultaneously. The focus is on flow patterns, among which stands out the secondary vortex inside the plug with low viscosity when the viscosity ratio is far from 1. The secondary vortex at the cap of the plug is resulting from the momentum transfer due to interface continuity. The influence of plug lengths and viscosity ratio upon the skin friction coefficients are analyzed in preparation for calculating the pressure loss in real design work.

In chapter 5, a summary of this thesis is made. The limitations of this work as well as those of the analytical modeling are also presented. Some suggestions for the potential work are provided in the end.

In appendix A, my supervisor Dr. Ri Li and I find out a correlation for calculating maximum and minimum stream functions in the plug flow in chapter 2. However, the correlations for heat transfer performance or enhancement is not established due to limited time. Hence, this part is recorded in an appendix as a secondary outcome of the thesis.

Chapter 2

Analytical study of gas-liquid plug flow in concentric microchannel

2.1 Mathematic modeling

2.1.1 Governing equations and boundary conditions

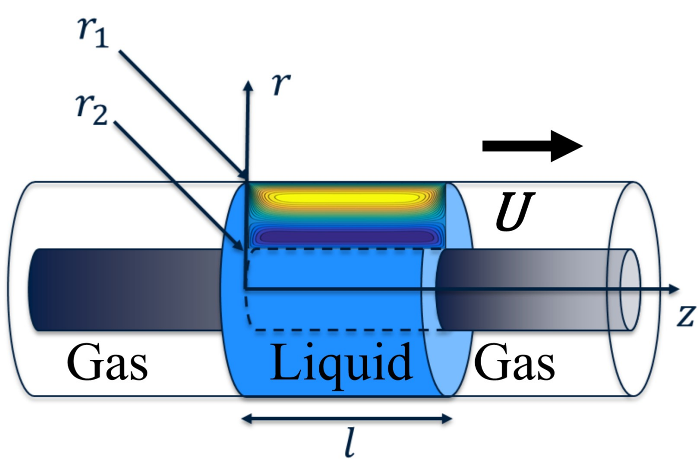

Figure 2.1: Schematic show for gas-liquid plug flow in concentric microchannel

The plug flow in the micro concentric tube is modeled under a cylindrical coordinate system, which is moving at the same speed as the liquid plug, using a fourth order PDE. The governing equations have the following assumptions: 1. the flow field is fully developed, 2. the liquid plug takes up the whole cross-section, 3. the interface between the liquid and the gas is flat, 4. the whole flow field is rotationally symmetric, 5. the fluid is Newtonian with uniform and isotropic physical properties, 6. the fluid obeys Stokes assumption ($\mathrm{Re} \ll 1$).

Before starting the modeling procedures, I would like to talk firstly about the gap between these assumptions and real scenario. To my best knowledge, the Stokes assumption is the most appropriate method to date for analytically calculating the flow field in plug flows. The request of low Reynolds number (Re $\ll 1$) can be easily reached under micro-scales. Meanwhile, it can capture the vortexes formed because the flow field is solved in the 2-D domain.

However, some assumptions above such as that the whole cross-section is taken up by the plug (no liquid film) can hardly be reached in real scenarios. It has been studied in [41, 51, 52, 54, 65] that the liquid film's thickness is very small and negligible only when Ca $\ll 1$ (capillary number Ca is defined below, the ratio of viscous force and the surface tension). Otherwise, the liquid film will be thicker and the plug shape will deform owing to the viscous force. The existence of liquid film can also lead to the slippery boundary between the plug boundary and the wall, which makes the modeling and deriving the solution more complicated.

$$\mathrm{Ca} = \frac{\mu U}{\lambda}. \tag{2.1}$$

The interface is also hard to be flat in the real cases. The influence of curvature upon the flow field was investigated in [2], where the author set the contact angels at two ends to be the same. It was found out that the flow field was not much affected when the contact angel is between $45^\circ \sim 135^\circ$. Under these cases the flat end assumption is valid and the contribution of surface tension upon, for instance, the pressure loss, can be de-coupled from the contributions from the frictional force. However, in real cases, the contact angle can be different at two ends, and it is also different at two walls if the channel is not symmetric (i.e., the meandering channel or the concentric channel in this work) which leads to too many combinations to validate.

As mentioned earlier in section 1.3, the capture of these detailed features can only be done by accurate multi-phase flow simulation with surface capturing methods if they are not pre-defined, which are also very time-consuming. Negotiation has to be made between the accuracy and efficiency. Hence, in this work, I will still adopt the analytical method with the Stokes flow model and the above assumptions because I aim to build either a quick method or a dense database for the design need. Though it is recommended that in the real design work, the analytical results in this chapter, the results from the simplified model of heat transfer in chapter 3 and the analytical results in chapter 4 can be used for primary searching to narrow down the range of optimal designs quickly. Then a few times of accurate simulation can be conducted to calibrate the influences brought by liquid film or curved interfaces.

Following the assumptions above, the continuity equation is,

$$\nabla \cdot \boldsymbol{u} = 0. \tag{2.2}$$

In the momentum equation, the convection term is neglected (Re $\ll 1$),

$$\mu \nabla^2 \boldsymbol{u} - \nabla P = \mathbf{0}. \tag{2.3}$$

By applying the Stokes stream function, the continuity equation eq. (2.2) is satisfied automatically, and the momentum equation eq. (2.3) is simplified as below by taking curve at both sides

$$\mathcal{L}^4_{-1} \psi = 0, \tag{2.4}$$

where the Stokes stream function ψ is defined as

$$u_r = -\frac{1}{r}\frac{\partial \psi}{\partial z},\ u_z = \frac{1}{r}\frac{\partial \psi}{\partial r}, \tag{2.5}$$

and the operator $\mathcal{L}^4_{-1}$ is

$$\mathcal{L}^4_{-1} = \left(\frac{\partial^2}{\partial z^2} + \frac{\partial^2}{\partial r^2} - \frac{1}{r}\frac{\partial}{r}\right)\left(\frac{\partial^2}{\partial z^2} + \frac{\partial^2}{\partial r^2} - \frac{1}{r}\frac{\partial}{r}\right). \tag{2.6}$$

Three assumptions are made here to obtain the boundary conditions: First, because of the continuity of the streamline, the stream function can be set to a constant value at all boundaries. For simplicity, it is set to zero. Second, there is no slip between the walls and the liquid plug. Thus, the axial velocity at walls is $-U$ in the moving reference. At last, there is no shear stress caused by the gas because usually, gas has low viscosity. As a result, the boundary condition can be written as,

$$\psi(0,r)=0,\ \psi(l,r)=0,\ \psi(z,r_1)=0,\ \psi(z,r_2)=0, \tag{2.7}$$

$$\frac{1}{r}\frac{\partial^2\psi}{\partial z^2}(0,r)=0,\ \frac{1}{r}\frac{\partial^2\psi}{\partial z^2}(l,r)=0, \tag{2.8}$$

$$\frac{1}{r}\frac{\partial\psi}{\partial r}(z,r_1)=-U,\ \frac{1}{r}\frac{\partial\psi}{\partial r}(z,r_2)=-U. \tag{2.9}$$

The nondimensionalization is done before solving the PDEs, and the aspect ratio β, the inner-outer radius ratio η and the eigenvalues ω_n are also defined by

$$\hat{z}\equiv\frac{z}{r_1},\ \hat{r}\equiv\frac{r}{r_1},\ \hat{u}_z\equiv\frac{u_z}{U},\ \hat{u}_r\equiv\frac{u_r}{U},\ \hat{\psi}\equiv\frac{\psi}{Ur_1^2}, \tag{2.10}$$

$$\eta=\frac{r_2}{r_1}=\hat{r}_2,\ \beta=\frac{\hat{l}}{1-\eta},\ \omega_n=\frac{n\pi}{\hat{l}}, \tag{2.11}$$

Substitute eqs. (2.10) and (2.11) into eqs. (2.4) and (2.7) to (2.9) to obtain the dimensionless governing equation and boundary conditions

$$\hat{\mathcal{L}}^4_{-1}\hat{\psi}=0, \tag{2.12}$$

$$\hat{\psi}(0,\hat{r})=0,\ \hat{\psi}(\hat{l},\hat{r})=0,\ \hat{\psi}(\hat{z},1)=0,\ \hat{\psi}(\hat{z},\eta)=0, \tag{2.13}$$

$$\frac{1}{\hat{r}}\frac{\partial^2\hat{\psi}}{\partial\hat{z}^2}(0,\hat{r})=0,\ \frac{1}{\hat{r}}\frac{\partial^2\hat{\psi}}{\partial\hat{z}^2}(\hat{l},\hat{r})=0, \tag{2.14}$$

$$\frac{1}{\hat{r}}\frac{\partial\hat{\psi}}{\partial\hat{r}}(\hat{z},1)=-1,\ \frac{1}{\hat{r}}\frac{\partial\hat{\psi}}{\partial\hat{r}}(\hat{z},\eta)=-1. \tag{2.15}$$

2.1.2 Analytical solution

Strong periodicity can be observed focusing the boundary conditions at the two plug ends in eqs. (2.13) and (2.14) Thus, the finite Fourier transformation can be applied here.

Due to the zero value of the function at these ends, the Sine transformation is chosen

$$\mathcal{S}_n[\hat{\psi}] = \frac{2}{\hat{l}} \int_0^{\hat{l}} \hat{\psi} \sin(\frac{n\pi}{\hat{l}}\hat{z}) \mathrm{d}\hat{z} = g_n(\hat{r}). \tag{2.16}$$

The anti-transformation can be applied to obtain the original function, which is the universal solution to the PDEs.

$$\hat{\psi} = \sum_{n=1}^{\infty} \hat{\psi}_n = \sum_{n=1}^{\infty} \sin(\frac{n\pi}{\hat{l}}\hat{z}) g_n(\hat{r}). \tag{2.17}$$

The properties of the Sine transformation are listed below.

$$\mathcal{S}_n[\frac{\partial^2 \hat{\psi}}{\partial \hat{z}^2}] = -\omega_n^2 g_n + \frac{2\omega_n}{\hat{l}}[\hat{\psi}(0,\hat{r}) - (-1)^n \hat{\psi}(\hat{l},\hat{r})] = -\omega_n^2 g_n, \tag{2.18}$$

$$\mathcal{S}_n[\frac{\partial^4 \hat{\psi}}{\partial \hat{z}^4}] = -\omega_n^2 \mathcal{S}_n[\frac{\partial^2 \hat{\psi}}{\partial \hat{z}^2}] + \frac{2\omega_n}{\hat{l}}[\frac{\partial^2 \hat{\psi}}{\partial \hat{z}^2}(0,\hat{r}) - (-1)^n \frac{\partial^2 \hat{\psi}}{\partial \hat{z}^2}(\hat{l},\hat{r})] = \omega_n^4 g_n, \tag{2.19}$$

$$\mathcal{S}_n[\frac{\partial \hat{\psi}}{\partial \hat{r}}] = \frac{\mathrm{d}g_n}{\mathrm{d}r}. \tag{2.20}$$

Substitue eqs. (2.16) and (2.18) to (2.20) into eqs. (2.12) to (2.15), the system then becomes a 4th order, linear and homogeneous ordinary differential equation one (ODEs).

$$(\frac{\mathrm{d}^2}{\mathrm{d}r} - \frac{1}{r}\frac{\mathrm{d}}{\mathrm{d}r} - \omega_n^2)(\frac{\mathrm{d}^2}{\mathrm{d}r} - \frac{1}{r}\frac{\mathrm{d}}{\mathrm{d}r} - \omega_n^2) g_n = 0, \tag{2.21}$$

$$g_n(\eta) = 0,\ g_n(1) = 0, \tag{2.22}$$

$$g_n'(\eta) = -\frac{2\eta[1-(-1)^n]}{\hat{l}\omega_n},\ g_n'(1) = -\frac{2[1-(-1)^n]}{\hat{l}\omega_n}, \tag{2.23}$$

The universal solution of the ODEs eq. (2.21) is

$$g_n(\hat{r}) = A_n \hat{r}^2 \mathrm{I}_2(\omega_n \hat{r}) + B_n \hat{r} \mathrm{I}_1(\omega_n \hat{r}) + C_n \hat{r}^2 \mathrm{K}_2(\omega_n \hat{r}) + D_n \hat{r} \mathrm{K}_1(\omega_n \hat{r}), \tag{2.24}$$

where $\mathrm{I}_\nu, \mathrm{K}_\nu$ are the νth order of first and second modified Bessel functions respectively.

Also, obviously, for series n being even numbers, only zero solution will be obtained. In this chapter, the series n is by default set to be odds without further notice. For odd series, the constant coefficients can be mounted using the boundary condition eqs. (2.22) and (2.23). The system is formed with n linear and homogeneous subsystems each with a dimension of 4×4, which can all be solved easily by Cramer's rule [66].

$$\begin{pmatrix} \mathrm{I}_2(\omega_n) & \mathrm{I}_1(\omega_n) & \mathrm{K}_2(\omega_n) & \mathrm{K}_1(\omega_n) \\ \eta\mathrm{I}_2(\omega_n\eta) & \mathrm{I}_1(\omega_n\eta) & \eta\mathrm{K}_2(\omega_n\eta) & \mathrm{K}_1(\omega_n\eta) \\ \mathrm{I}_1(\omega_n) & \mathrm{I}_0(\omega_n) & -\mathrm{K}_1(\omega_n) & -\mathrm{K}_0(\omega_n) \\ \eta\mathrm{I}_1(\omega_n\eta) & \mathrm{I}_0(\omega_n\eta) & -\eta\mathrm{K}_1(\omega_n\eta) & -\mathrm{K}_0(\omega_n\eta) \end{pmatrix} \begin{pmatrix} A_n \\ B_n \\ C_n \\ D_n \end{pmatrix} = \begin{pmatrix} 0 \\ 0 \\ -\frac{4}{\hat{l}\omega_n^2} \\ -\frac{4}{\hat{l}\omega_n^2} \end{pmatrix}. \tag{2.25}$$

A series solution of the eqs. (2.12) to (2.15) can be traced back finally by putting eq. (2.24) into eq. (2.17). Then, the velocity field is obtained using the definition of the stream function in eq. (2.5).

$$\hat{\psi} = \sum_{n=1,3,5...} \sin(\omega_n \hat{z})[A_n \hat{r}^2 \mathrm{I}_2(\omega_n \hat{r}) + B_n \hat{r} \mathrm{I}_1(\omega_n \hat{r}) + C_n \hat{r}^2 \mathrm{K}_2(\omega_n \hat{r}) + D_n \hat{r} \mathrm{K}_1(\omega_n \hat{r})], \tag{2.26}$$

$$\hat{u}_z = \sum_{n=1,3,5...} \omega_n \sin(\omega_n \hat{z})[A_n \hat{r} \mathrm{I}_1(\omega_n \hat{r}) + B_n \mathrm{I}_0(\omega_n \hat{r}) - C_n \hat{r} \mathrm{K}_1(\omega_n \hat{r}) - D_n \mathrm{K}_0(\omega_n \hat{r})], \tag{2.27}$$

$$\hat{u}_r = -\sum_{n=1,3,5...} \omega_n \cos(\omega_n \hat{z})[A_n \hat{r} \mathrm{I}_2(\omega_n \hat{r}) + B_n \mathrm{I}_1(\omega_n \hat{r}) + C_n \hat{r} \mathrm{K}_2(\omega_n \hat{r}) + D_n \mathrm{K}_1(\omega_n \hat{r})]. \tag{2.28}$$

As mentioned earlier, the pumping power is a key factor in evaluating the performance and efficiency of a heat exchanger. Thus, the pressure difference ΔP and the skin friction coefficient C_f are derived in the following for later study.

To be noted that there are too many factors affecting the skin friction coefficient C_f to be all included (like the capillary number Ca, Weber number We and the interface curvature).

Here, only the friction force caused by the radial gradient of the internal recirculation is considered. The influences of these interface geometry parameters are neglected due to the assumption of the two flat ends.

$$F_f = 2\pi\mu(r\int_0^l \frac{\partial u_z}{\partial r}\mathrm{d}z)\Big|_{r_2}^{r_1}, \tag{2.29}$$

$$\Delta P = \frac{F_f}{\pi(r_1^2 - r_2^2)}. \tag{2.30}$$

The Fanning friction factor and the skin friction coefficient are defined as below, where $D_h = \frac{4\pi(r_1^2-r_2^2)}{2\pi(r_1+r_2)} = 2(r_1 - r_2)$,

$$f = \frac{1}{4}\frac{D_h\frac{\Delta P}{l}}{\frac{1}{2}\rho V^2} = \frac{D_h\Delta P}{2\rho l V^2}, \tag{2.31}$$

$$C_f = f\mathrm{Re}. \tag{2.32}$$

eqs. (1.1) and (2.29) to (2.32) yield the result for the Fanning skin friction coefficient

$$C_f = \frac{8}{\beta(1+\eta)}\sum_{n=1,3,5...}\omega_n[A_n\hat{r}^2\mathrm{I}_0(\omega_n\hat{r}) + B_n\hat{r}\mathrm{I}_1(\omega_n\hat{r}) + C_n\hat{r}^2\mathrm{K}_0(\omega_n\hat{r}) + D_n\hat{r}\mathrm{K}_1(\omega_n\hat{r})]\Big|_1^\eta. \tag{2.33}$$

The sensitivity study is carried out, where the skin friction coefficient C_f is used as the objective. It is clearly shown in fig. 2.2 that C_f becomes stable after the series number is higher than 101. For security, for all of the calculations, I set the series number to 101 to ensure accuracy.

2.2 Results and discussions

2.2.1 Verify solution accuracy using CFD Results

A comparison to the numerical simulation conducted in the Fluent 16.2 (ANSYS, inc. USA) is made to verify the accuracy of the analytical results. The inner-outer radius ratio

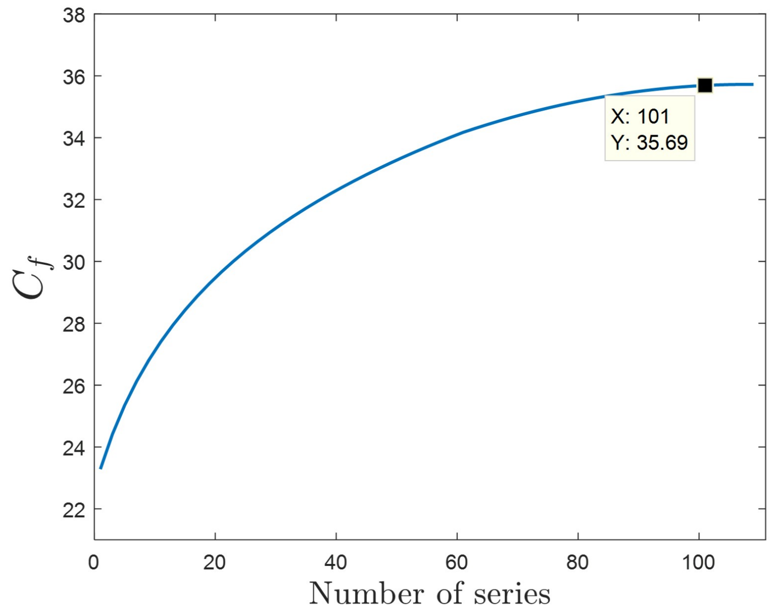

Figure 2.2: The sensitivity study for the analytical solution. Variation of C_f with the growing series number. $\beta = 2$, $\eta = 0.5$.

is $\eta =$, 0.5, 0.75 , and the aspect ratio is $\beta = 1$. The frontal and rear ends of the plug are set to be planar to fit the assumption of the analytical model. The laminar flow model is applied, the Reynolds number is set to be 0.5. Water is chosen as the operating fluid. The number of meshes for all three cases are about 5×10^5, which passes the mesh independence check. The outer and the inner walls are set to moving wall condition with $-10\,mm/s$. For the two ends between the liquid plug and the gas, no shear wall condition is applied. The absolute criteria for convergence are set to be 10^{-3} for continuity and velocity in all three directions. Since the model is axisymmetric, I randomly choose a slice which passes the axial. Then the data for the flow field on these slices are exported for comparison.

From fig. 2.3.(a) and .(b), the velocity field of the analytical model and that of the CFD simulation corresponds well with each other. No obvious difference could be found. The comparison here can be treated as a verification to the analytical solution's accuracy.

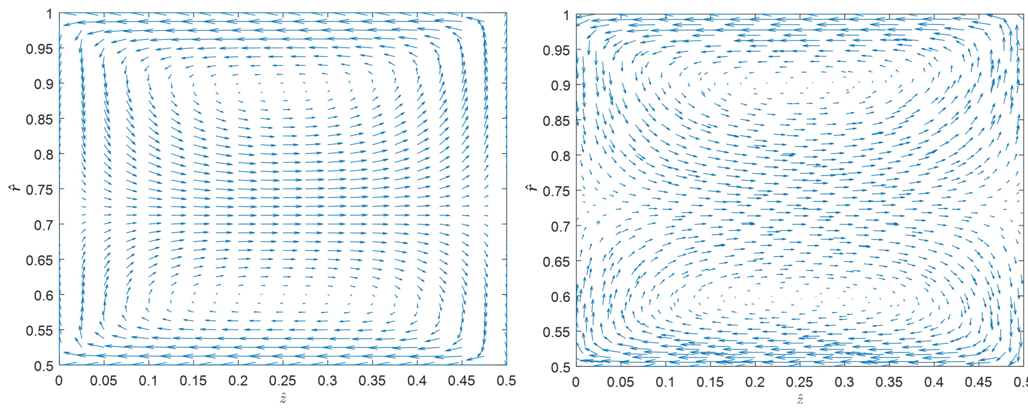

Figure 2.3: The velocity vector plot of (a). the analytical model and (b). the CFD results, $\beta = 1,\ \eta = 0.50$

2.2.2 Validate using continuous flow(1-D model)

To validate the analytical model using continuous flow, the flow field of fully developed Stokes flows in the concentric annulus was calculated in [67],

$$\hat{u}_{1D}(\hat{r}) = \frac{2(\hat{r}^2 - 1)\ln\eta - 2(\eta^2 - 1)\ln\hat{r}}{\eta^2 - 1 - (\eta^2 + 1)\ln\eta} - 1. \tag{2.34}$$

The stream function can be integrated from eq. (2.34) and the constant term could be bounded using the zero value boundary condition.

$$\hat{\psi}_{1D}(1) = \hat{\psi}_{1D}(\eta) = 0, \tag{2.35}$$

$$\hat{\psi}_{1D}(\hat{r}) = \frac{[(\hat{r}^2 + \eta^2 - 1)\ln\eta - (2\eta^2 - 1)\ln\hat{r}]\hat{r}^2 + \hat{r}^2\ln\hat{r} - \eta^2\ln\eta}{2(\eta^2 - 1 - (\eta^2 + 1)\ln\eta)}. \tag{2.36}$$

The skin friction coefficient for 1-D model is also be derived in a similar fashion (eqs. (1.1), (2.29) to (2.32) and (2.34))

$$C_{f,1D} = \frac{16(1 - \eta)^2\ln\eta}{\eta^2 - 1 - (\eta^2 + 1)\ln\eta}. \tag{2.37}$$

Especially, the skin friction coefficient can be calculated under 2 asymptotic situations where the inner radius is zero (in a circular tube, $\eta \to 0, C_{f,1D} \to 16$) and is infinitely close to the outer radius (in a slit channel, $\eta \to 1, C_{f,1D} \to 24$), respectively. The results for $C_{f,1D}$ will be used as a validation between continuous flow and very long plugs in section 2.2.6.

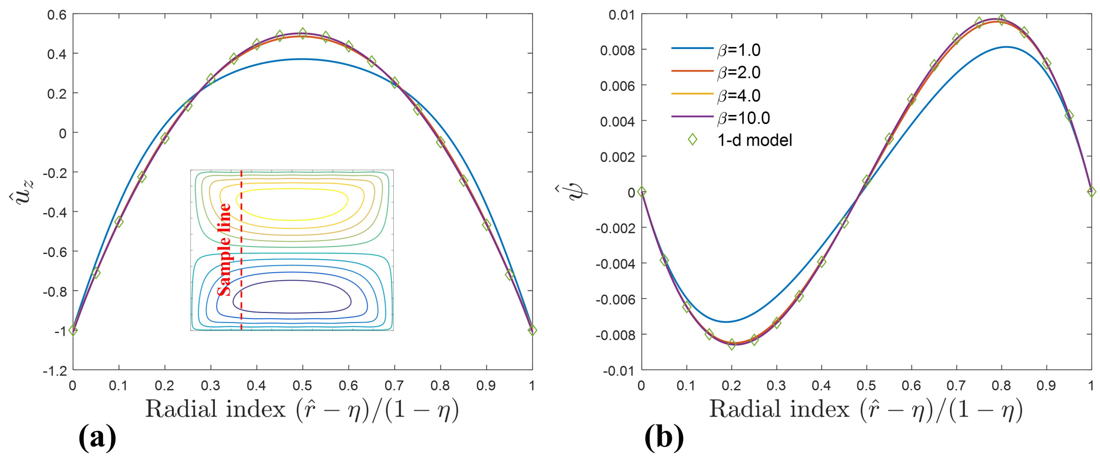

Figure 2.4: The comparison between plugs with different aspect ratio β and the 1-D model of (a) the axial velocity $\hat{u}_z$. (b) The stream function $\hat{\psi}$. The sample line is at $\hat{z} = 0.25\,\hat{l}$, and the inner-outer radius ratio is $\eta = 0.90$.

The comparison between the axial velocity and the stream function on the sample line ($\hat{z} = 0.25\,\hat{l}$) of the plug flow model and these of the continuous 1-D model is plotted in fig. 2.4. When the plug is short (i.e., $\beta = 1.0$), a maximum difference of 0.2 and 0.0025 can be observed for $\hat{u}_z$ and $\hat{\psi}$, respectively. When $\beta = 2.0$, the difference becomes very small but still visible. When the plug is long enough (i.e., $\beta = 10.0$), the axial velocity distribution, as well as that of stream function, will be infinitely close to those of the 1-D model. Thus, the result here can be considered as a validation under the asymptotic scenarios.

2.2.3 Two asymmetric vortexes

The vortexes in plug flow are forced vortexes resulting from the driving force of the moving wall (in the plug reference) and the interface between fluids. Hence, the flow pattern inside the plug can be influenced by the geometry parameters including the inner-outer radius ratio η of the channel and the aspect ratio β of the plug.

A group of contours of the stream function is presented in fig. 2.5. Two asymmetric vortexes can be observed. The one closer to the inner wall is referred to as the inner vortex, while the other is called the outer vortex. Obvious variation such as the size of the two vortexes, the location of their centers and the maximum/minimum stream function values can be observed with growing η. Thus, discussions upon these phenomena will be conducted in this subsection.

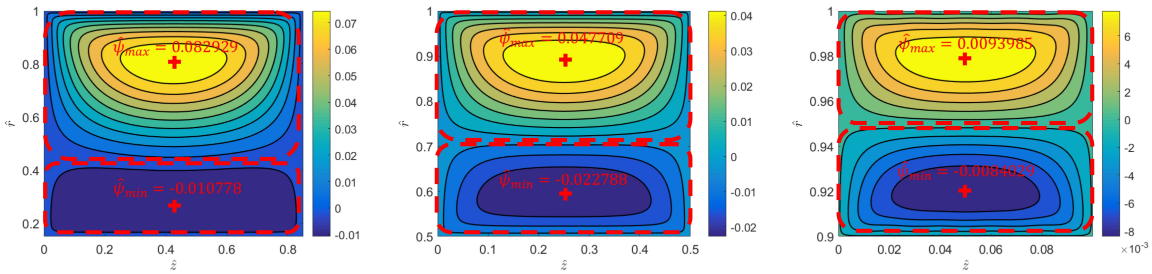

(a) η=0.15 (b) η=0.50 (c) η=0.90

Figure 2.5: The contour plots for stream function in plugs with different η, the cross shape marker are the locations for vortex centers.

Since the inner and the outer vortex have different orientations, they can be classified using the signal of their stream functions. Due to the rotationally symmetric system, I can set the polar angel interval to be $0 \sim 1$ for simplification. Then, the size or the volume taken up by the inner vortex can be numerically integrated using the formula below, where sgn is the signal function,

$$\hat{V}_{in,v} = \int_0^{\hat{l}} \int_\eta^1 \frac{1 - \mathrm{sgn}(\hat{\psi})}{2} \hat{r} \mathrm{d}\hat{r} \mathrm{d}\hat{z}. \tag{2.38}$$

Similarly, the volume of the outer vortex can be written as,

$$\hat{V}_{out,v} = \int_0^{\hat{l}} \int_\eta^1 \frac{1 + \mathrm{sgn}(\hat{\psi})}{2} \hat{r} \mathrm{d}\hat{r} \mathrm{d}\hat{z}. \tag{2.39}$$

The total volume of the plug is,

$$\hat{V}_{plug} = \hat{V}_{in,v} + \hat{V}_{out,v} = \int_0^{\hat{l}} \int_\eta^1 \hat{r} \mathrm{d}\hat{r} \mathrm{d}\hat{z} = \frac{(1 - \eta^2)\hat{l}}{2}. \tag{2.40}$$

The volume ratio between the inner and the outer vortex $\hat{V}_{in,v}/\hat{V}_{out,v}$ is plotted in fig. 2.6. $\hat{V}_{in,v}/\hat{V}_{out,v}$ is always smaller than 1 and it is a increasing function of η. When $\eta \to 1$ two vortexes become nearly identical to each other, the volume ratio $\hat{V}_{in,v}/\hat{V}_{out,v}$ becomes close to 1, which is like the plug flow in a slit channel. $\hat{V}_{in,v}/\hat{V}_{out,v}$ is also a decreasing function of the aspect ratio β, especially when it is short ($\beta < 2$). This indicates the inner vortex can take up more space when $\beta < 2$. When $\beta > 2$, volume ratio becomes nearly stable and the influence of β is not obvious.

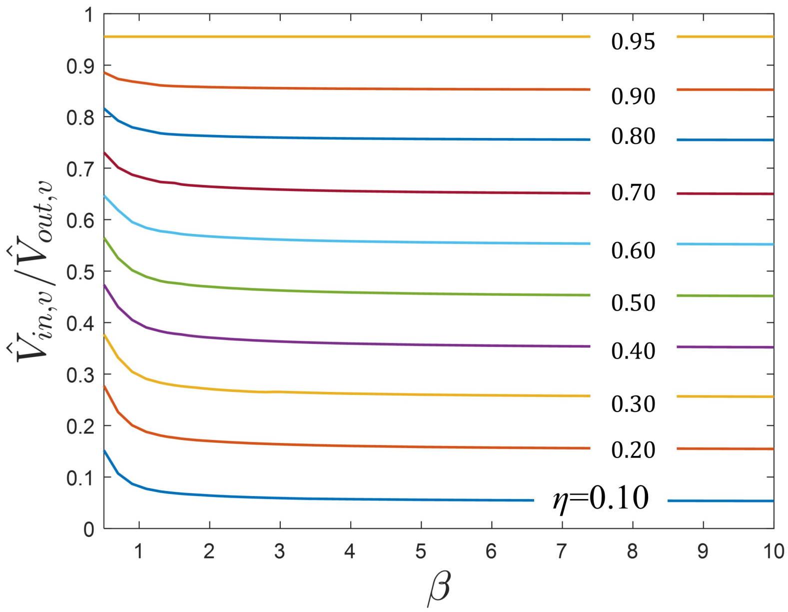

Figure 2.6: The volume ratio between the inner and the outer vortex $\hat{V}_{in,v}/\hat{V}_{out,v}$.

The volume change of vortexes can also lead to the swift locations of their centers. The centers always locate at the middle (axial direction) of the plug, and the radial index are where stream function reaches maximum/minimum value ($\hat{r}_{\psi_{max}}, \hat{r}_{\psi_{min}}$). Define the index for the relative locations in the radial direction of vortex centers as below,

$$I_{out,v} = \frac{\hat{r}_{\psi_{max}} - \eta}{1-\eta},\ I_{in,v} = \frac{\hat{r}_{\psi_{min}} - \eta}{1-\eta}. \tag{2.41}$$

The indexes $I_{out,v}$ and $I_{in,v}$ are plotted in fig. 2.7. When η increases, both $I_{out,v}$ and $I_{in,v}$ increases, which means both centers move towards the outer wall. As shown in fig. 2.6, the inner vortex takes more volume of the whole and expands when η increases, it is natural for the inner vortex center to shift away from the inner wall. Meanwhile, the outer vortex shrinks and the center should move towards the outer wall for the similar reason. Moreover, the indexes also become independent of the aspect ratio when $\beta > 2$.

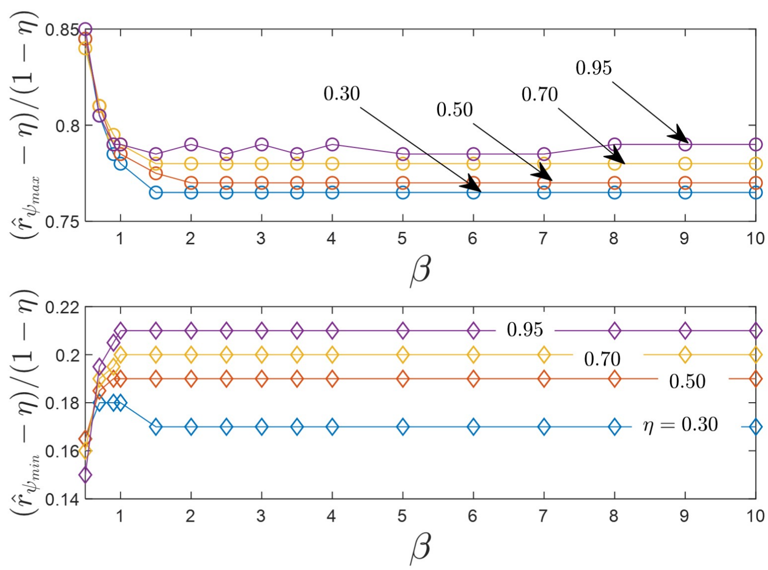

Figure 2.7: The index for relative location in radial direction of vortex centers.

The strength difference between the two vortexes is also of interest. Thus, the absolute value of the ratios of minimum and maximum stream functions $|\hat{\psi}_{min}/\hat{\psi}_{max}|$ are plotted in fig. 2.8. $|\hat{\psi}_{min}/\hat{\psi}_{max}|$ has nearly the same variations to those of the volume ratio $\hat{V}_{in,v}/\hat{V}_{out,v}$ (in fig. 2.6). Thus there is no need to describe these variations again. However, the ratios of both volumes and the stream functions only reveals the difference between the inner and the outer vortex in the same plug, and it can not be used to describe the magnitudes of circulation cross multiple cases with different geometry parameters. The magnitudes of circulation inside the plug thus will be discussed in the next subsection.

2.2.4 Quantify radial transport using the averaged recirculation flux

Che, Wong, and Nguyen [3] have pointed out in their research that the heat transfer enhancement inside the plug flow (in a slit channel) is due to the internal recirculation and the transverse flow near the front and the rear ends. They plotted out the transverse velocity distribution on the sample lines which cross the vortex centers for investigation.

Here I adopt the similar strategy by putting sample lines through the two vortex centers. However, instead of using the radial velocity, the product of velocity and radius $\hat{r}\hat{u}_r$ (referred to as the recirculation flux) is studied owing to the changing cross-section area at different $\hat{r}$

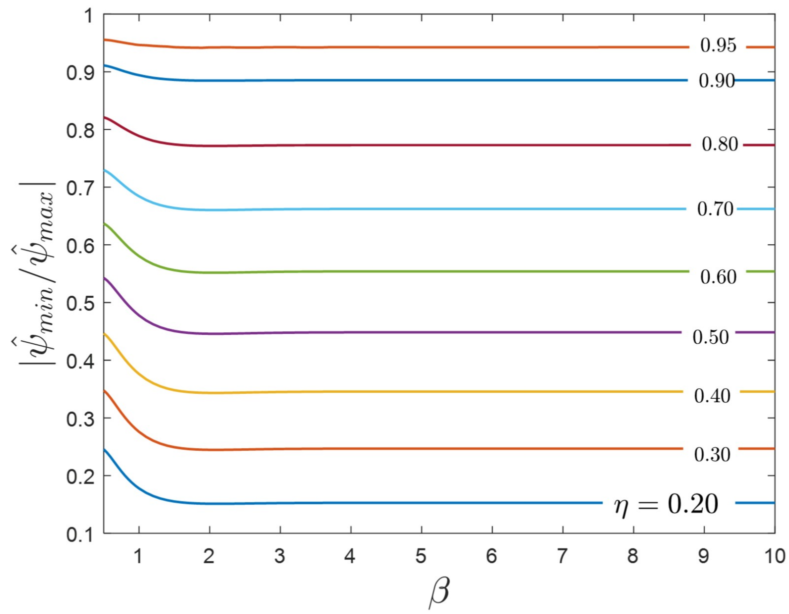

Figure 2.8: The stream function ratio between the inner and the outer vortex centers $\hat{\psi}_{min}/\hat{\psi}_{max}$.

in the cylindrical coordinator. Moreover, the averaged value of $\hat{r}\hat{u}_r$ at inner/outer vortexes are studied instead of their distributions for the convenient comparison between multiple cases. The averaged recirculation flux can be calculated by concerning the volumetric flow rate (the change of stream function defined by eq. (2.5)) on the right half of sample lines,

$$\hat{\psi}_{max/min} = \hat{\psi}_{max/min} - 0 = \int_{\hat{l}}^{\hat{l}/2} (-\hat{r}\hat{u}_r)\mathrm{d}\hat{l}\,\bigg|_{\hat{r}_{\hat{\psi}_{max/min}}} = \int_{\hat{l}/2}^{\hat{l}} \hat{r}\hat{u}_r\mathrm{d}\hat{l}\,\bigg|_{\hat{r}_{\hat{\psi}_{max/min}}}.$$

Reorganize the equation above and define the averaged recirculation flux $(\hat{r}\hat{\bar{u}}_r)_{out,v/in,v}$ of two vortexes, where the signal of it represents the direction of rotation only.

$$(\hat{r}\hat{\bar{u}}_r)_{out,v/in,v} = \frac{\hat{\psi}_{max/min}}{\hat{l} - \hat{l}/2} = \frac{2\hat{\psi}_{max/min}}{\hat{l}}. \tag{2.42}$$

As shown in fig. 2.9 recirculation flux at both vortexes are decreasing functions of aspect ratio β, which is referred to as the diminishing effect when the plug length increases. In the small subplot in fig. 2.9, the recirculation at the outer always vortex is stronger than that of the inner vortex. When the inner-outer radius ratio η increases, the averaged recirculation flux of the inner vortexes becomes stronger, and that of the outer vortex becomes weaker. When $\eta \to 1$, they become nearly the same in absolute value because the channel tends to be a slit one and the flow field becomes symmetric.

Overall, the averaged recirculation flux $(\hat{r}\hat{\hat{u}}_r)_{out,v/in,v}$ can describe and compare the magnitudes of vortexes under multiple cases. This parameter can help understand the heat transfer enhancement.

2.2.5 Recirculation period

As mentioned earlier in section 1.3, the recirculation period is an important factor for evaluate procedures of heat transfer in plug flow such as estimating the entrance region. However, the definition of the recirculation period is not consistent. For example, it was roughly defined as one plug length plus twice of the hydraulic diameter of the tube ($l_{plug} + 2D_h$) in [41] because this definition can suit his explanation for experiment results, while more accurate trajectory simulations were conducted in [3, 42] to record the distribution of recirculation period. Here I applied the latter way to investigate the recirculation period.

The recirculation periods are recorded by numerically tracing some passive points which are initially put on the central plane until they finish one period of recirculation. The nondimensionalization is conducted as below,

$$\hat{t} = \frac{tU}{(r_1 - r_2)}. \tag{2.43}$$

The distributions of recirculation period $\hat{t}$ on the central plane(in axial direction, $\hat{z} = \hat{l}/2$) are plotted in fig. 2.10. When β increases, the amplitude of $\hat{t}_{rec}$ increases exponentially owing to the diminishing effect mentioned earlier, which can lead to weaker heat transfer enhancement. The double-arrow marks are the boundaries between the inner and the outer vortexes, and it also moves slightly towards the inner wall, which indicates a smaller volume ratio $\hat{V}_{in,v}/\hat{V}_{out,v}$. This matches well with the conclusion made in fig. 2.6.

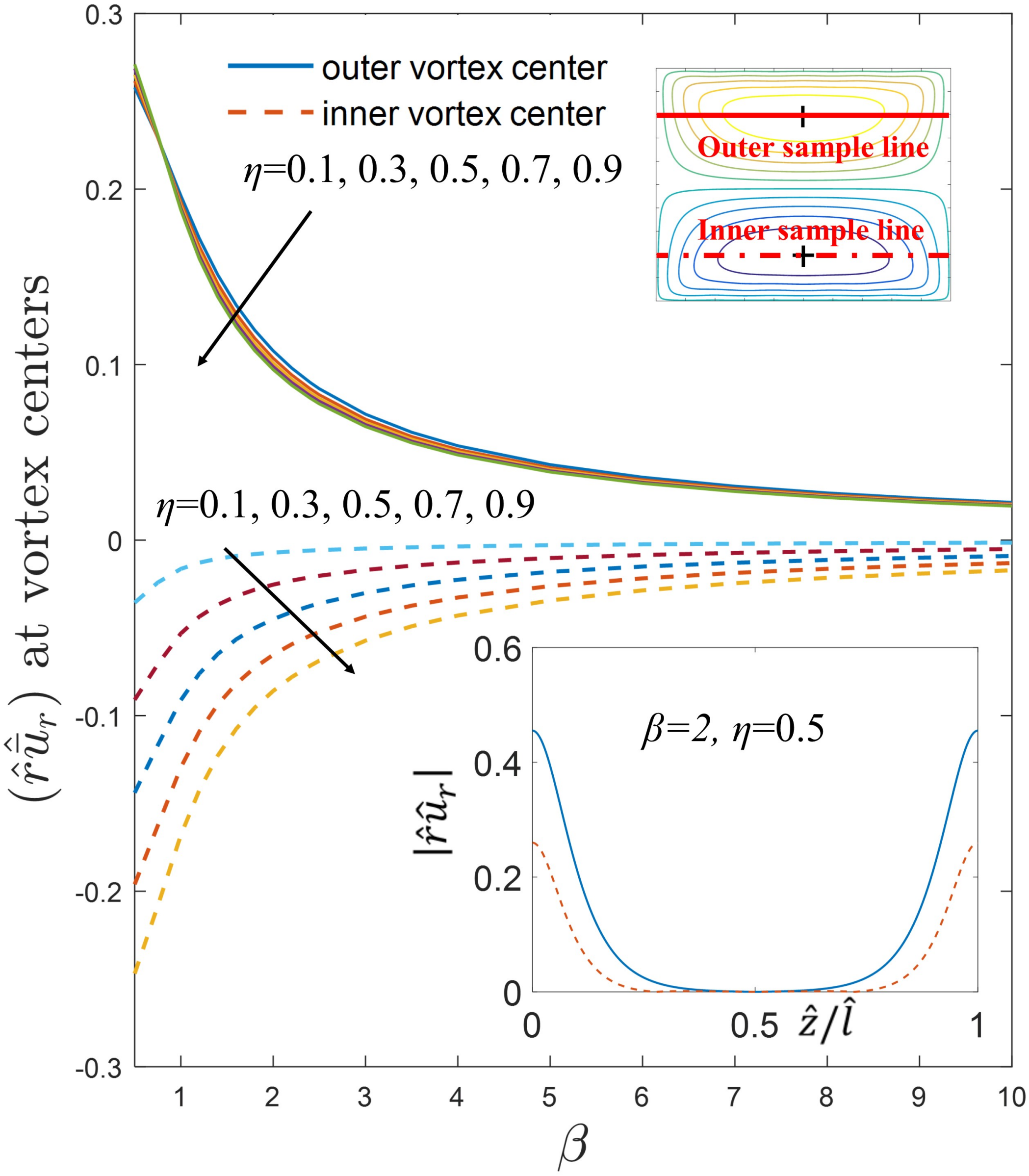

Figure 2.9: The recirculation flux $\hat{r}\hat{u}_r$ of the inner vortex and the outer vortex. Main plot is the averaged value, the small subplots show where the sample line is (right-top), and a detailed distribution on the sample line for $\beta = 2$, $\eta = 0.5$ (right-bottom), respectively.

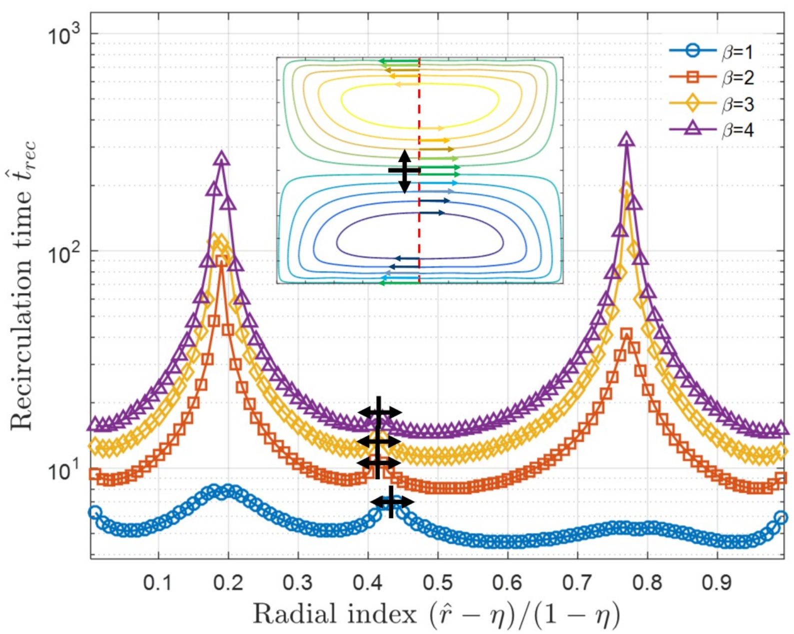

Figure 2.10: The distribution of recirculation time $\hat{t}$ on the central of the plug ($\hat{z} = \hat{l}/2$). The double-arrows mark the boundaries between the inner and the outer vortexes. $\beta = 1,\ 2,\ 3,\ 4$, $\eta = 0.5$.

2.2.6 The skin friction coefficient

The influences of β are presented in fig. 2.11.(a). under selected η. With the increasing β, C_f drops down dramatically owing to the diminishing effect of the recirculation. The dash lines in fig. 2.11.(a). are the results for the 1-D model calculated through eq. (2.37). The 1-D results are infinitely close to those of long plugs and it can be treated as a validation. When $\beta > 46$ the gap between the C_f of the plug flow and the 1-D model is lower than 1%. Thus, C_f can be simply evaluated using the results from 1-D model (eq. (2.37)) when the plug is long enough ($\beta > 46$). An asymptotic case with $\eta = 10^{-5}$ is also conducted to compare with the C_f in plug flow with circular cross-sections [2]. And, the results show a perfect agreement.

The influences of η are presented in fig. 2.11.(b). under selected β. Overall, C_f increases as η grows. The trend is more obvious for relatively longer plugs. For instance, C_f increases about $12.5\%, 25\%$ and 50% for $\beta = 2, 10, 100$ when η increases from 0.05 to 0.95, respectively. For long plugs the internal recirculation is quite weak, thus the influence of different curvature of the 2 walls plays an important role. While for short plugs ($\beta = 1$) the flow is almost characterized by the recirculation, thus C_f is less dependent on η.

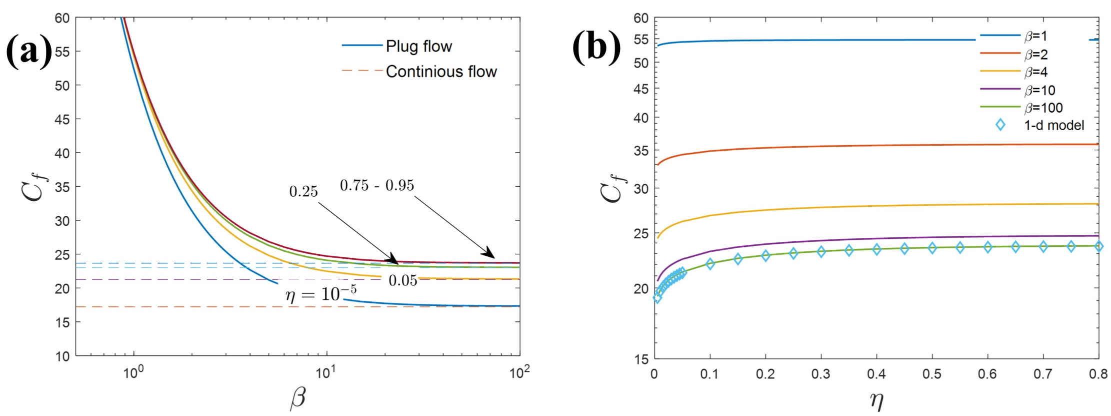

Figure 2.11: The skin friction coefficient (a). versus β for selected η and (b). versus η for selected β

2.3 Summary of this chapter

The plug flow has two well-defined vortexes due to the immersible interfaces between the liquid and the gas, which can potentially enhance the mixing ability and heat transfer. In this work, the plug flow in the concentric microchannel is modeled using a 4th order PDE set. The series solution for the set is found, and the flow field is investigated in detail. Focuses are made upon the influence of the geometry parameters (the aspect ratio β, and the inner-outer radius ratio η) upon the flow pattern such as vortex center location I, intensity ratio $|\hat{\psi}_{min}/\hat{\psi}_{max}|$, the volume ratio $\hat{V}_{in,v}/\hat{V}_{out,v}$, the averaged recirculation flux $\hat{r}\hat{\bar{u}}_r$ of two vortexes and the recirculation period $\hat{t}$. The influences upon the skin friction coefficient C_f are also studied. These findings are summarized as below:

- The flow pattern is greatly influenced by the inner-outer radius ratio η. The higher η makes the flow tend to be like plug flow in a 2-D microchannel with symmetric patterns ($\hat{V}_{in,v}/\hat{V}_{out,v} \rightarrow 1$, $|\hat{\psi}_{min}/\hat{\psi}_{max}| \rightarrow 1$). At lower η, however, two different vortexes were generated. The outer vortex is similar to that in the microchannel with round cross-section which takes up most of the volume in the plug, while the inner vortex is weaker and takes up the smaller volume ($\hat{V}_{in,v}/\hat{V}_{out,v} < 1$, $|\hat{\psi}_{min}/\hat{\psi}_{max}| < 1$).

- The radial transport phenomena can be quantified using the averaged recirculation flux. At the inner vortex, the averaged recirculation flux grows stronger with increasing η, while that at outer vortex becomes weaker. The averaged recirculation fluxes of both vortexes decrease dramatically when β increases, which leads to exponentially increasing recirculation period with increasing β. This is referred to as the diminishing effect of recirculation with increasing β.

- The skin friction coefficient C_f can be influenced by both β and η. Overall C_f drops nearly exponentially with growing β. It increases with growing η, though this trend is more obvious for relatively longer plugs. For instance, C_f increases about $12.5\%, 25\%$ and 50% for $\beta = 2, 10, 100$ respectively when η increases from 0.05 to 0.95.

Chapter 3

Numerical study of heat transfer inside plug flow in chapter 2 at asymmetric boundary conditions

3.1 Modeling for transient heat transfer process in plug flow

3.1.1 Governing equation and initial/boundary conditions

The governing equation for transient heat transfer for a single plug can be written as below, where $\alpha = k/\rho c_p$ represents the thermal diffusivity, k is the conductivity and c_p is the specific heat of the fluid.

$$\frac{\partial T}{\partial t} + \frac{1}{r}\frac{\partial (u_r T r)}{\partial r} + \frac{\partial (u_z T)}{\partial z} = \alpha[\frac{1}{r}\frac{\partial}{\partial r}(r\frac{\partial T}{\partial r}) + \frac{\partial^2 T}{\partial z^2}]. \tag{3.1}$$

It should be noted that the influences of viscous dissipation, body forces, and pressure difference are all neglected by assuming the Eckert number is small (Ec $\ll 1$). The physical meaning of Ec is the ratio of the kinetic energy to the enthalpy driving force ($c_p \Delta T$) for heat transfer (ΔT is the temperature difference between the wall and the mean value of fluid). This assumption is reasonable and can be validated by calculating Ec using parameters from previous studies. For example, in the experimental work of Asthana, Zinovik, Weinmueller and Poulikakos[22] the velocity is $U = 1$ m/s, the working liquid is water with $c_p = 4186\text{J}/(\text{K}\cdot\text{kg})$, $\Delta T \cong 2.55\text{K}$. Thus the Eckert number is $\text{Ec} = 0.9\text{E}{-5} \ll 1$ and the effects of above can be neglected.

$$\mathrm{Ec} = \frac{U^2}{c_p \Delta T}. \tag{3.2}$$

In the real cases, the initial condition should be a steady-state temperature distribution, which is determined by the boundaries before the heating part of the channel. Though using the real initial condition can help improve the accuracy of the developing process of the field, it requires much more input pieces of information and adds more complexity to our investigation. Hence for the initial condition in this work, the whole plug is set to have a uniform temperature distribution.

$$T = T_i. \tag{3.3}$$

There are many kinds of boundary conditions in reality, and it is costly to evaluate the heat transfer performance at all of these boundary conditions. Hence, three typical boundary types are chosen to study in this thesis and they are listed as below.

- The inner iso-flux boundaries (shorten as IFB). It represents the plug enters a heat exchanger with constant heat flux at the inner wall, while the outer wall is isolated.
- The iso-thermal boundaries (shorten as ITB). It represents the plug enters a heat exchanger with constant inner and outer wall temperatures.
- The outer iso-flux boundaries (shorten as OFB). This boundary type is basically the same as IFB, the only difference is the orientation of the heat transfer that constant heat flux is loaded from the outer wall, while the inner wall is isolated.

The schematic show for transient heat transfer is plotted in fig. 3.1. As the liquid plug moves towards the downstream of the channel, it gradually accumulates heat. The thermal field inside also develops. The development of the thermal field, as well as heat transfer ability, is of interest.

The boundary condition for IFB

$$-k\frac{\partial T}{\partial r}(z, r_2) = q'', \ -k\frac{\partial T}{\partial r}(z, r_1) = 0. \tag{3.4}$$

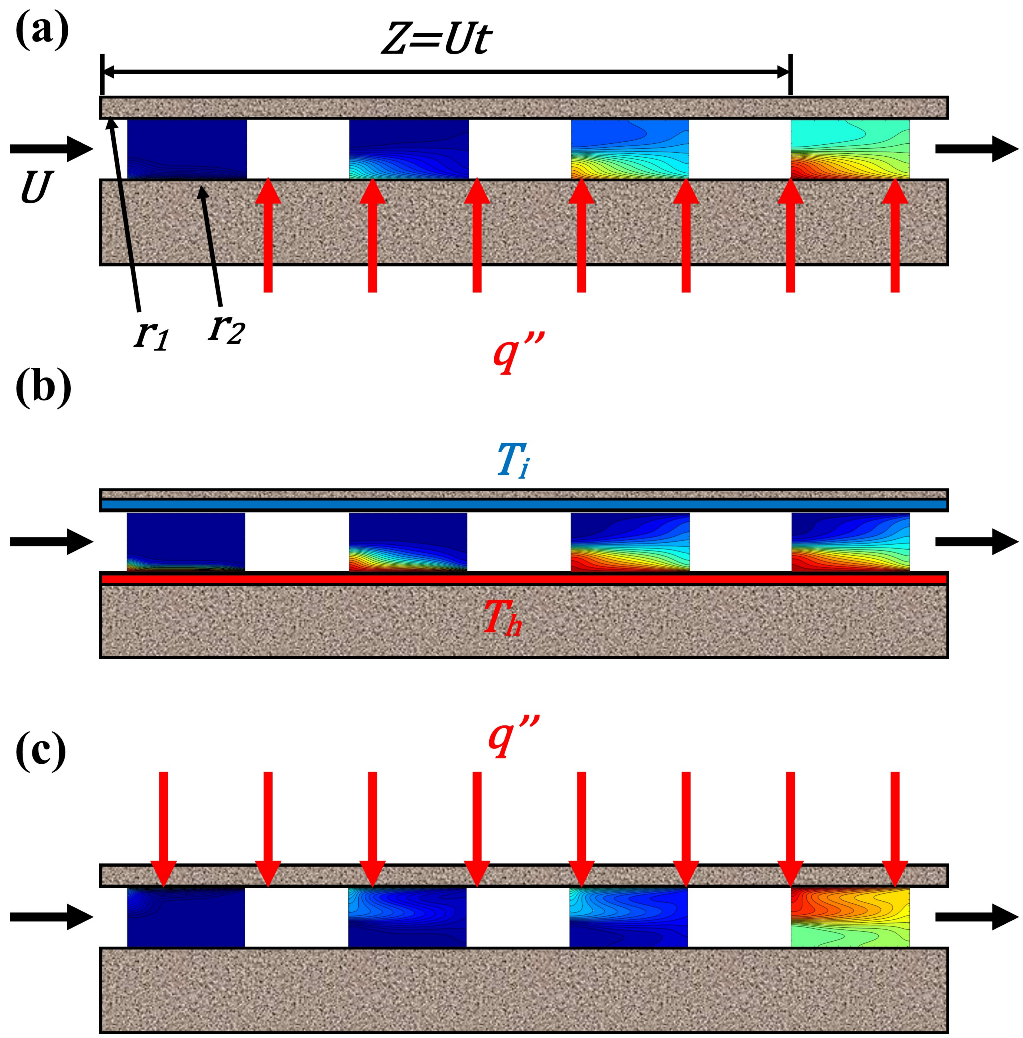

Figure 3.1: The schematic show of boundary conditions (a). The inner iso-flux boundaries (IFB). (b). The iso-thermal boundaries (ITB). (c). The outer iso-flux boundaries (OFB). The contours are taken at $\hat{t} = (1, 6, 25, 40)$ (eq. (2.43)) under these 3 boundary types correspondingly. $(\beta, \eta, \mathrm{Pe}) = (2, 0.5, 100)$.

For ITB

$$T(z, r_2) = T_h,\ T(z, r_i) = T_i. \tag{3.5}$$

For OFB

$$-k\frac{\partial T}{\partial r}(z, r_2) = 0,\ -k\frac{\partial T}{\partial r}(z, r_1) = -q''. \tag{3.6}$$

The heat transfer at two ends of the plug is neglected because its segmented by gas. Thus the adiabatic condition at the two ends of the plug is as below,

$$\frac{\partial T}{\partial z}(0, r) = 0,\ \frac{\partial T}{\partial z}(l, r) = 0. \tag{3.7}$$

3.1.2 Nondimensionalization

The nondimensionalization for governing equations and boundary conditions could be conducted using the parameters below

$$\hat{T} \equiv \frac{T - T_i}{\Delta T_{std}}, \tag{3.8}$$

where the standard temperature difference $\Delta T_{std} = \frac{q''(r_1 - r_2)}{k}$ is for the IFB and OFB, $\Delta T_{std} = T_h - T_i$ for ITB.

Substitute eqs. (2.10), (2.11), (2.43) and (3.8) into eqs. (3.1) and (3.3) to (3.6) to obtain the the dimensionless governing equations

$$\frac{\partial \hat{T}}{\partial \hat{t}} + (1 - \eta)\left(\frac{\hat{u}_r}{\hat{r}}\frac{\partial(\hat{T}\hat{r})}{\partial \hat{r}} + \hat{u}_z\frac{\partial \hat{T}}{\partial \hat{z}}\right) = \frac{(1-\eta)^2}{\mathrm{Pe}}\left[\frac{1}{\hat{r}}\frac{\partial}{\partial \hat{r}}\left(\hat{r}\frac{\partial \hat{T}}{\partial \hat{r}}\right) + \frac{\partial^2 \hat{T}}{\partial \hat{z}^2}\right], \tag{3.9}$$

where Pe is the Peclet number. Pe represents the ratio between advection ability and diffusion ability,

$$\mathrm{Pe} = \frac{U(r_1 - r_2)}{\alpha}. \tag{3.10}$$

The initial condition

$$\hat{T} = 0. \tag{3.11}$$

Grids	$\hat{T}$: vertex centered, uniform grids $\hat{\boldsymbol{u}}$: staggered grids, pre-stored analytical results
N_r, N_z $\Delta\hat{t}$	200, $\beta * 200$ $\frac{1}{8}\min(1/N_r, \mathrm{Pe}/N_r^2)$
Advection terms	Linear upwind differential scheme (LUDS)
Diffusion terms	Central differential scheme (CS)
Temporal terms	First order forward in time (1^{st} FT)

Table 3.1: Set-up for numerical solution of heat transfer

The boundary condition for IFB

$$\frac{\partial \hat{T}}{\partial \hat{r}}(\hat{z}, \eta) = -\frac{1}{1-\eta}, \ \frac{\partial \hat{T}}{\partial \hat{r}}(\hat{z}, 1) = 0. \tag{3.12}$$

For ITB

$$T(\hat{z}, \eta) = 1, \ T(\hat{z}, 1) = 0. \tag{3.13}$$

For OFB

$$\frac{\partial \hat{T}}{\partial \hat{r}}(\hat{z}, \eta) = 0, \ \frac{\partial \hat{T}}{\partial \hat{r}}(\hat{z}, 1) = \frac{1}{1-\eta}. \tag{3.14}$$

And, the adiabatic condition at the two ends of the plug

$$\frac{\partial \hat{T}}{\partial \hat{z}}(0, \hat{r}) = 0, \ \frac{\partial \hat{T}}{\partial \hat{z}}(\hat{l}, \hat{r}) = 0. \tag{3.15}$$

The eqs. (3.9) and (3.11) to (3.15) are discretized using the finite volume method, then coded to be simulated in MATLAB 2016A. As illustrated in section 1.3, the flow field and the thermal field is decoupled under the scenarios where $\mathrm{Pr} \gg 1$. The simulation uses the pre-stored flow field results obtained by the analytical method in chapter 2. More details about the setup of the numerical solving can be examined in table 3.1.

3.2 Modeling for the asymptotic case - continuous Stokes flow heat transfer

When discussing the heat transfer performance of the plug flow configuration, usually that of the single-phase flow is also derived for comparison. For instance, the ratio of the

Nusselt number Nu of the two kinds of configurations can be used to show the enhancement by plug flow.

To obtain the fully developed thermal field of the continuous Stokes flow heat transfer inside the concentric tube, firstly a Euler reference sticking to the ground is used for simplification. Under this reference, the fully developed thermal field is a function of spatial indexes $(\hat{z}, \hat{r})$ only, and the axial derivative $\frac{\partial \hat{T}}{\partial \hat{z}}$ becomes constant and independent of the radial index $\hat{r}$ [68]. The derivation of the solution for the fully developed thermal field at IFB is shown as below, while those at other two boundary types can also be obtained in a similar fashion.

With the help of the control volume method, it is found out that

$$\frac{\partial \hat{T}}{\partial \hat{z}} = \frac{2\eta}{\mathrm{Pe}(1-\eta^2)}. \tag{3.16}$$

A simplified version of eq. (3.9) is used to describe the thermal field by substitute eq. (3.16) into it, plus by setting the radial velocity $\hat{u}_r = 0$, the axial diffusion term $\frac{\partial^2 \hat{T}}{\partial \hat{z}^2} = 0$, and the temporal term $\frac{\partial \hat{T}}{\partial \hat{t}} = 0$.

$$\frac{2\eta}{(1+\eta)(1-\eta)^2}(\hat{u}_z \hat{r}) = \frac{1}{\hat{r}}\frac{\partial}{\partial \hat{r}}(\hat{r}\frac{\partial \hat{T}}{\partial \hat{r}}). \tag{3.17}$$

To be noted here the $\hat{u}_z$ is the dimensionless velocity to the ground, thus it equals to $\hat{u}_{1D}(\hat{r}) + 1$ in the Euler reference sticking to the plug in eq. (2.34). For simplification, the form of the velocity field is reorganized for later derivation.

$$\hat{u}_z = E\hat{r}^2 + F\ln\hat{r} - E, \tag{3.18}$$

where the constant coefficients E, F are

$$E = \frac{2\ln\eta}{\eta^2 - \eta^2\ln\eta - \ln\eta - 1},\ F = \frac{2(1-\eta^2)}{\eta^2 - \eta^2\ln\eta - \ln\eta - 1}. \tag{3.19}$$

Substitute eqs. (3.18) and (3.19) into eq. (3.17), then integrate twice to obtain the fully developed thermal field in the form of difference between local temperature and that of the inner wall $\hat{T} - \hat{T}_{in,w}$. Since in the internal flow, heat transfer performance is usually described using dimensionless parameters (like Nusselt number Nu or thermal resistance σ) based upon temperature difference and spatial derivative, the distribution of $\hat{T} - \hat{T}_{in,w}$ is enough for calculation.

$$\hat{T} - \hat{T}_{in,w} = \frac{2\eta}{(1+\eta)(1-\eta)^2} \left(\frac{E}{16}\hat{r}^4 + \frac{F}{4}\hat{r}^2 \ln \hat{r} - \frac{E+F}{4}\hat{r}^2 + \frac{E+F}{4} \ln \hat{r} \right) \Big|_{\eta}^{\hat{r}}. \tag{3.20}$$

Using a similar fashion, the results under the inner iso-thermal and the outer iso-flux boundaries can also be obtained.

For ITB,

$$\hat{T} = \log_{\eta} \hat{r}. \tag{3.21}$$

For OFB,

$$\hat{T} - \hat{T}_{out,w} = \frac{2}{(1+\eta)(1-\eta)^2} \left(\frac{E}{16}\hat{r}^4 + \frac{F}{4}\hat{r}^2 \ln \hat{r} - \frac{E+F}{4}\hat{r}^2 + \frac{E+F+2-2\eta}{4} \ln \hat{r} \right) \Big|_{1}^{\hat{r}}. \tag{3.22}$$

The calculation was conducted in MATLAB 2016A, and results were stored in the compatible style as these from plug flows, so they can be quoted for the same post-processing (such as calculating Nu), and then compared with each other. In the following sections, subscript $_{sp}$ represents that the results are taken from single-phase/continuous Stokes flow heat transfer.

3.3 Heat transfer performance at inner iso-flux boundary (IFB)

In this section, the heat transfer process at IFB is presented versus the dimensionless time $\hat{t}$. Then a simplified thermal network is introduced, where several dimensionless parameters such as the dimensionless thermal conductance σ_{plug} are defined to evaluate the heat transfer performance. The enhancement by applying plug flow configuration is calculated by comparing to the single-phase flow in the form of conductance ratio $\sigma_{plug}/\sigma_{sp}$, and influences of dimensionless inputs η, β and Pe are presented and discussed.

3.3.1 Processes of heat transfer and its simplified thermal network

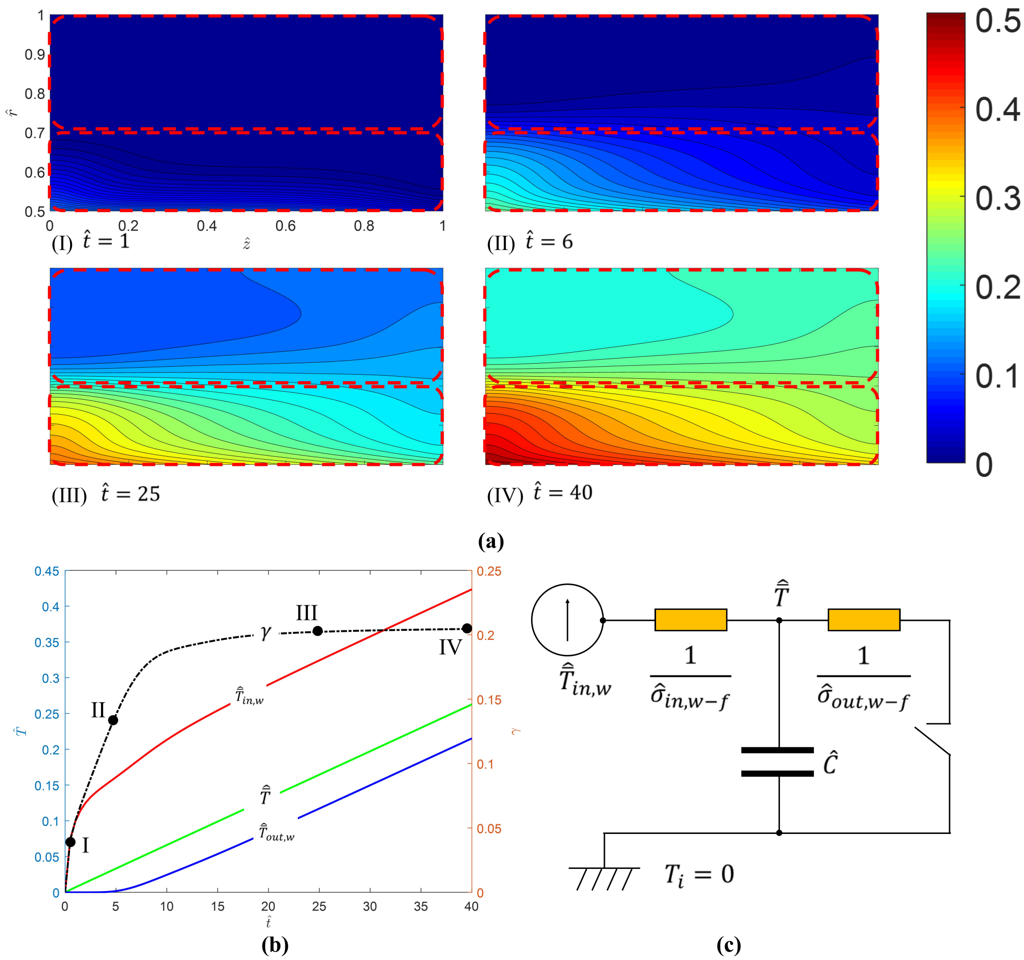

Figure 3.2: Heat transfer process at IFB, $(\beta, \eta, \mathrm{Pe}) = (2, 0.5, 100)$. (a). (I) $\sim$ (IV) Sequence of dimensionless temperature $\hat{T}$ distribution at $\hat{t}_{\mathrm{I}\sim\mathrm{IV}} = (1, 6, 25, 40)$. (b). Variation of dimensionless temperature at the inner wall $\hat{T}_{in,w}$, at the outer wall $\hat{T}_{out,w}$ and the mean value $\hat{\bar{T}}$, and the mixing index γ. The black solid points correspond to the examples shown in (a). (c). Simplified thermal network for IFB.

A typical sequence of the developing thermal field of a plug $(\beta, \eta, \mathrm{Pe}) = (2, 0.5, 100)$ at IFB is plotted in fig. 3.2. After entering the heating channel with a uniform initial temperature, the thermal boundary layer first develops within the inner vortex with the help of both advection and diffusion (fig. 3.2 (a). (I).). The mean temperature $\hat{\bar{T}}$ (defined below) and the inner wall average temperature $\hat{\bar{T}}_{in,w}$ both increase (fig. 3.2 (b).). At this beginning stage, there is nearly no heat input into the outer vortex yet, thus no obvious increase is observed for the outer wall average temperature $\hat{\bar{T}}_{out,w}$.

$$\hat{\bar{T}} = \frac{\int_{r_2}^{r_1}\int_0^l r u_z T \mathrm{d}z\mathrm{d}r}{\int_{r_2}^{r_1}\int_0^l r u_z \mathrm{d}z\mathrm{d}r} = \frac{\int_{\eta}^{1}\int_0^{\hat{l}} \hat{r}\hat{u}_z \hat{T} \mathrm{d}\hat{z}\mathrm{d}\hat{r}}{\int_{\eta}^{1}\int_0^{\hat{l}} \hat{r}\hat{u}_z \mathrm{d}\hat{z}\mathrm{d}\hat{r}}. \tag{3.23}$$

The expansion of the thermal layer continues and reaches the boundary between the inner and the outer vortexes (fig. 3.2 (a). (II).). Then there occurs an obvious heat transfer between the inner and the outer vortex. The heat transferred through the vortex boundary is considered as the input into the outer vortex, and it initiates the increase of the outer wall average temperature $\hat{\bar{T}}_{out,w}$ (fig. 3.2 (b).) with the help of the advection and diffusion of the outer vortex.

After developing with the help of the convection in the inner vortex, the heat transfer through the vortex boundary and the convection in the outer vortex, the relative shape of the temperature contour gradually becomes steady (fig. 3.2 (a). (III) and (IV).). This yields the steady and identical growth rate of $\hat{\bar{T}}$, $\hat{\bar{T}}_{in,w}$ and $\hat{\bar{T}}_{out,w}$. The mixing index γ is defined to describe the relative location of $\hat{\bar{T}}$ between the interval of $\hat{\bar{T}}_{in,w}$ and $\hat{\bar{T}}_{out,w}$. At this stage, the mixing index γ becomes steady due to the identical growth rate of $\hat{\bar{T}}$, $\hat{\bar{T}}_{in,w}$ and $\hat{\bar{T}}_{out,w}$. Thus, the fully thermal developed field is considered to be reached here.

$$\gamma = \frac{\hat{\bar{T}} - \hat{\bar{T}}_{out,w}}{\hat{\bar{T}}_{in,w} - \hat{\bar{T}}_{out,w}}. \tag{3.24}$$

The result in fig. 3.2 reveals the process of heat transfer at IFB: (1). The convection inside the inner vortex. (2). The development of the heat transfer through the boundary between the inner and the outer vortexes. (3). The convection in both vortexes and (4). The fully thermal developed field. Under the fully thermal developed field, a simplified thermal network is proposed in fig. 3.2 (c). to describe the heat transfer performance inside the plug flow. The thermal resistance $1/\hat{\sigma}_{in,w}$ and $1/\hat{\sigma}_{out,w}$ are defined as below to evaluate the overall heat transfer ability between the inner wall and the fluid, the outer wall and the fluid respectively. Since the outer wall is adiabatic under this boundary condition, the route for $1/\hat{\sigma}_{out,w}$ is cut, and all the heat flows into the capacitor (plug) to increase the mean temperature $\hat{\bar{T}}$.

$$\hat{\sigma}_{in,w-f} = -\frac{\eta}{\beta}\frac{\int_0^{\hat{l}}(\frac{\partial \hat{T}}{\partial r})_{\hat{r}=\eta}\mathrm{d}\hat{z}}{\hat{\bar{T}}_{in,w} - \hat{\bar{T}}}. \tag{3.25}$$

$$\hat{\sigma}_{out,w-f} = \frac{1}{\beta}\frac{\int_0^{\hat{l}}(\frac{\partial \hat{T}}{\partial r})_{\hat{r}=1}\mathrm{d}\hat{z}}{\hat{\bar{T}}_{out,w} - \hat{\bar{T}}}. \tag{3.26}$$

Substitute eq. (3.12) into eq. (3.25), the thermal resistance under this boundary condition (IFB) is obtained below. The simple relationship in eq. (3.27) indicates that the higher the conductance is, the relatively lower inner wall temperature (comparing to the mean temperature) is achieved, and it is less possible to cause device failure due to local high temperature.

$$\hat{\sigma}_{plug} = \hat{\sigma}_{in,w-f} = \frac{\eta}{1-\eta}\frac{1}{\hat{\bar{T}}_{in,w} - \hat{\bar{T}}}. \tag{3.27}$$

Since both the heat input and the total plug capacity are proportional to the plug length $\hat{l}$. It is better to define $\hat{C}_{plug}$ as the thermal capacity per length for comparison between cases with different lengths. Then $\hat{C}_{plug}$ can be calculated using control volume method (with the results in eq. (3.16)),

$$\hat{C}_{plug} = \frac{\mathrm{Pe}(1-\eta^2)}{2} = \frac{\mathrm{Pe}\hat{V}_{plug}}{\hat{l}}. \tag{3.28}$$

Since the properties has been assumed to be constant and uniform, the thermal capacity for the volume taken up by the inner and the outer vortex can also be calculated by comparing eqs. (2.38) to (2.40) and (3.28),

$$\hat{C}_{in,v} = \frac{\mathrm{Pe}\hat{V}_{in}}{\hat{l}}. \tag{3.29}$$

$$\hat{C}_{out,v} = \frac{\mathrm{Pe}\hat{V}_{out}}{\hat{l}}. \tag{3.30}$$

It is easily validated that $\hat{C}_{in,v}/\hat{C}_{out,v} = \hat{V}_{in,v}/\hat{V}_{out,v}$. This actually applies to any extensive physical properties as long as they are distributed uniformly. Thus in the later discussions, no specific difference needs to be addressed between one kind of capacity ratio and another such as the thermal capacity ratio and the mass capacity (volume) ratio.

In the following subsections, the influences of the plug aspect ratio β, the inner-outer radius ratio η, and the Peclect number Pe are taken into account. Considering that in the heat exchanger design work, the thermal field is fully developed for the most part of the device, only influences at this stage are investigated. Thus, the mixing index γ is recorded to assure that the thermal fully developed field is reached before the investigation.

3.3.2 Influences of the inner-outer radius ratio η

In fig. 3.3 (a). there presents the developing of the thermal conductance $\hat{\sigma}_{plug}$ under varying inner-outer radius ratios η, while the other two parameters are fixed at $(\beta, \mathrm{Pe}) = (2, 200)$ during the simulations. $\hat{\sigma}_{plug}$ experiences a decreasing process after the starting of the heat transfer and reaches a constant value after a period of time. The dimensionless time for sampling here is $\hat{t} = 58$, and the conductance $\hat{\sigma}_{plug}$ for all thermal fields are independent of $\hat{t}$ afterwards, thus the fully developed stage is reached.

The influence of the inner-outer radius ratio η is plotted in fig. 3.3 (b). The thermal conductance $\hat{\sigma}_{plug}$ increases with increasing η, because (1). the increasing averaged recirculation flux $(\hat{r}\hat{\bar{u}}_r)$ at the inner vortex enhances the advection near the inner wall (fig. 2.9), (2). the capacity ratio $\hat{C}_{in,v}/\hat{C}_{out,v}$ of the inner vortex increases (fig. 2.6), and the plug mean temperature $\hat{\bar{T}}$ is therefore closer to the average inner wall temperature $\hat{\bar{T}}_{in,w}$, $\hat{\bar{T}}_{in,w} - \hat{\bar{T}}$ is relatively lower, $\hat{\sigma}_{plug}$ is therefore higher (eq. (3.27)).

The conductance for single-phase flow heat transfer $\hat{\sigma}_{sp}$ and the enhancement denoted by $\hat{\sigma}_{plug}/\hat{\sigma}_{sp}$ are plotted in fig. 3.3 (b). It is found that the enhancement to single-phase flow $\hat{\sigma}_{plug}/\hat{\sigma}_{sp}$ first increases when η increases, it reaches a peak value of 2.78 at $\eta = 0.55$, and then decreases when η increases furthermore. All of the enhancements at different η are larger than 1.46 (obtained at η=0.90), which means there exist enhancement to the single-phase flow for all the inner-outer radius ratio η.

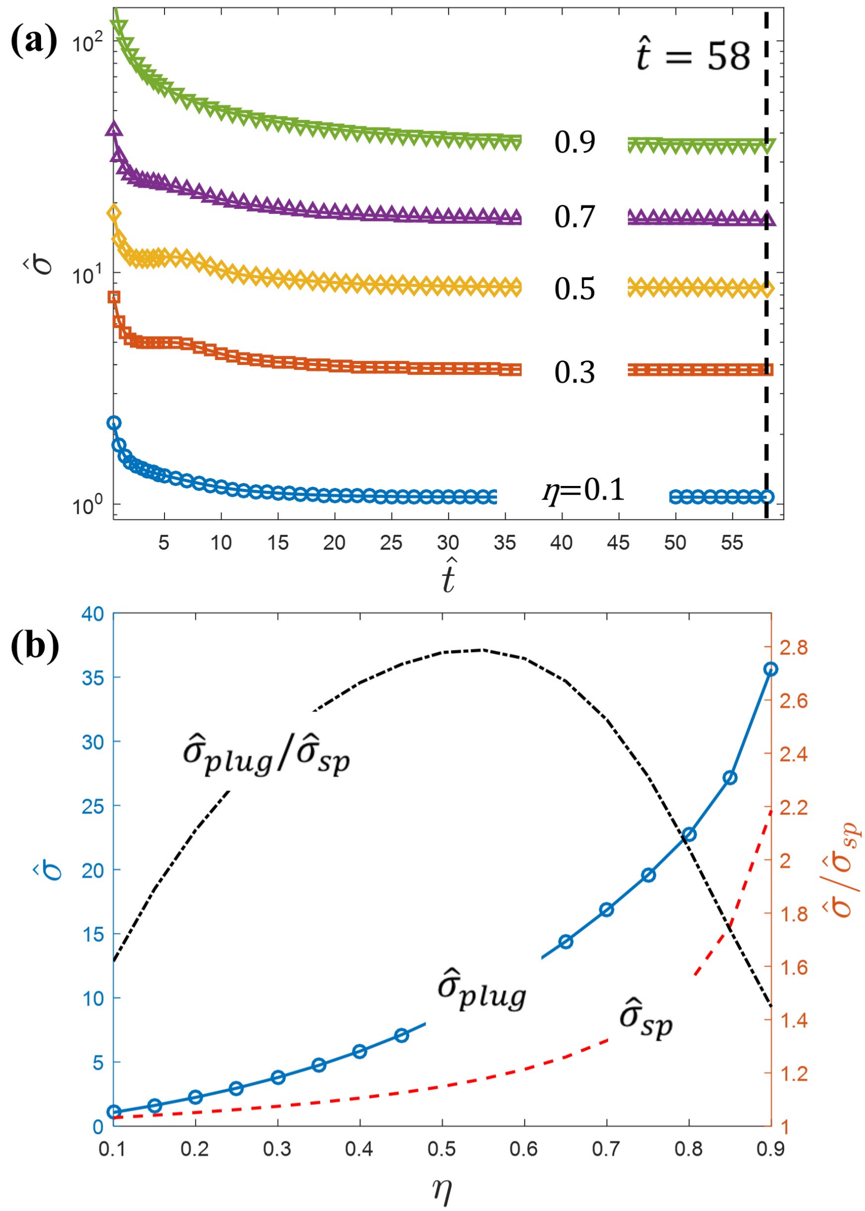

Figure 3.3: (a). Development of the thermal conductance $\hat{\sigma}_{plug}$, (b). influence of the inner-outer radius ratio η upon $\hat{\sigma}_{plug}$ and the enhancement by plug flow comparing to the single-phase flow heat transfer $\hat{\sigma}_{plug}/\hat{\sigma}_{sp}$. $(\beta, \mathrm{Pe}) = (2, 100)$

3.3.3 Influences of the aspect ratio β

In fig. 3.4 it plots the influence of plug dimensionless length β upon the thermal conductance $\hat{\sigma}_{plug}$, while the Peclet number Pe is fixed at Pe=200 during the simulations. In fig. 3.3 (a). $\hat{\sigma}_{plug}$ decreases when β increases, while its increasing trend with increasing η remains still.

This decreasing effect with growing β is already predicted earlier in both section 2.2.4 and section 3.3.1. Since the recirculation velocity, which determines the strength of advection, decreases with growing β. Moreover, the increasing length also increases the distance for each recirculation trajectory, which highly increases the recirculation period $\hat{t}_{rec}$ (fig. 2.10), reduces the recirculation frequency, and reduces the heat transfer enhancement.

In fig. 3.4 (b). the enhancement comparing to the single-phase flow heat transfer $\hat{\sigma}_{plug}/\hat{\sigma}_{sp}$ decreases when β increases. When $\eta = 0.9$, $\hat{\sigma}_{plug}/\hat{\sigma}_{sp}$ drops slightly and remains about 1.42 when β increases from 1 to 10. While at η=0.1, $\hat{\sigma}_{plug}/\hat{\sigma}_{sp}$ drops from 2.02 to 1.10 when β experiences the same increase. This indicates that for the lower inner-outer radius ratio η, the enhancement tends to be more affected by the plug length β. One of the reason can be that, at lower η the capacity ratio $\hat{\sigma}_{plug}/\hat{\sigma}_{sp}$ decreases more obviously with the growing β (fig. 2.6), and the plug mean temperature $\hat{\bar{T}}$ is thus away from inner wall temperature $\hat{\bar{T}}_{in,w}$, the difference $\hat{\bar{T}}_{in,w} - \hat{\bar{T}}$ increases more, and $\hat{\sigma}_{plug}$ drops more (eq. (3.27)).

Under each β, the enhancement still increases first, reaches the peak and then decreases again with the growing η. The peak value of each $\hat{\sigma}_{plug}/\hat{\sigma}_{sp}$ curve drops due to the diminishing of the internal recirculation, while the η to reach the peak value also increases when β increases. This interaction of β and η makes the enhancement to single-phase flow more complex, and thus the findings here can be used to search for the optimum design.

3.3.4 Influences of the Peclet number Pe

The influence of Pe is plotted in fig. 3.5 while the dimensionless plug length is fixed at β=2 during the simulations. In fig. 3.5 (a). the thermal conductance $\hat{\sigma}_{plug}$ increases when Pe grows. Meanwhile, it is observed in fig. 3.5 (b). that the enhancement to the single-phase flow $\hat{\sigma}_{plug}/\hat{\sigma}_{sp}$ also increases greatly when Pe grows. The mathematic explanation behind this is obvious that the total capacity of the plug $\hat{C}_{plug} = \text{Pe}(1 - \eta^2)/2$ is proportional to

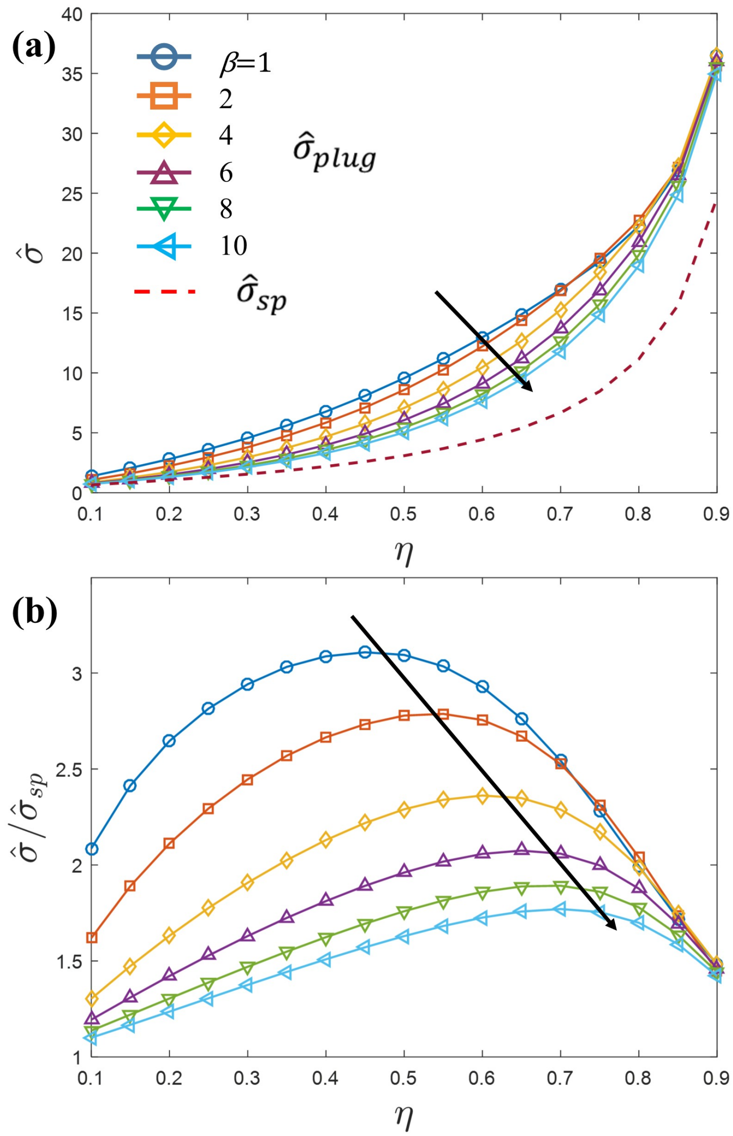

Figure 3.4: Influence of plug dimensionless length β upon (a). the thermal conductance $\hat{\sigma}_{plug}$, (b). the enhancement by plug flow comparing to the single-phase flow heat transfer $\hat{\sigma}_{plug}/\hat{\sigma}_{sp}$. The arrows in figures mark the direction of increasing β. Pe $= 100$.

the increasing Pe (eq. (3.27)), the amplitude of temperature difference $\hat{\hat{T}}_{in,w} - \hat{\hat{T}}$ then shall decreases with comparable scale, and the conductance therefore becomes higher (eq. (3.27)). The physics behind this explanation is that higher Pe means relatively higher heat capacity or convection ability, more portion of heat is carried by the hot fluid directly into the colder area away from the wall. Instead of diffusion in a single direction (inner wall-outer wall), this portion of heat diffuses into the vortex center/the outer vortex when advected by the fluid on the closed stream line, the diffusion area is larger, and thus the overall heat transfer performance is stronger. In fig. 3.5 (b). η to reach the peak value increases when Pe increases. The result is similar to that in fig. 3.3 (b). and is therefore useful for the design work.

Despite the findings in this section at IFB. In the real heat exchangers, there exist more types of boundary conditions and the whole process can be more complex. Thus, the discussions of the heat transfer at 2 other typical boundary conditions are carried out in the following 2 sections. Lots of the conclusion at this 3 boundary conditions are similar, and more focus will be made upon the differences between them.

3.4 Heat transfer performance at the inner iso-thermal boundaries (ITB), comparison to IFB

Unlike the inner iso-flux boundary condition, the outer wall here is not adiabatic and there exists the heat output through the outer wall. The developments of the heat input $\hat{Q}_{in}$, the heat through the vortex boundary $\hat{Q}_b$ and the heat output $\hat{Q}_{out}$ for a typical plug are plotted in fig. 3.6 (a)., while the other working conditions are the same as in fig. 3.2 The heat input $\hat{Q}_{in}$ reaches a high value as soon as the heat transfer starts and gradually decreases. Heat through the vortex boundary $\hat{Q}_b$ initiates at about $\hat{t} = 0.5$ and gradually increases. At last, heat output through the outer wall $\hat{Q}_{out}$ initiates at $\hat{t} = 3.0$ and gradually increases. Three heat transfer rates obey the following relationship $\hat{Q}_{out} \leq \hat{Q}_b \leq \hat{Q}_{in}$, which yield positive heat accumulation and temperature growing in both vortexes ($\hat{Q}_{in} - \hat{Q}_b \geq 0$ and $\hat{Q}_b - \hat{Q}_{out} \geq 0$). The equitation is obtained when the thermal field develops long enough ($\hat{t} > 26.0$), and there exists zero heat accumulation in the plug ($\hat{Q}_{out} = \hat{Q}_b = \hat{Q}_{in}$),

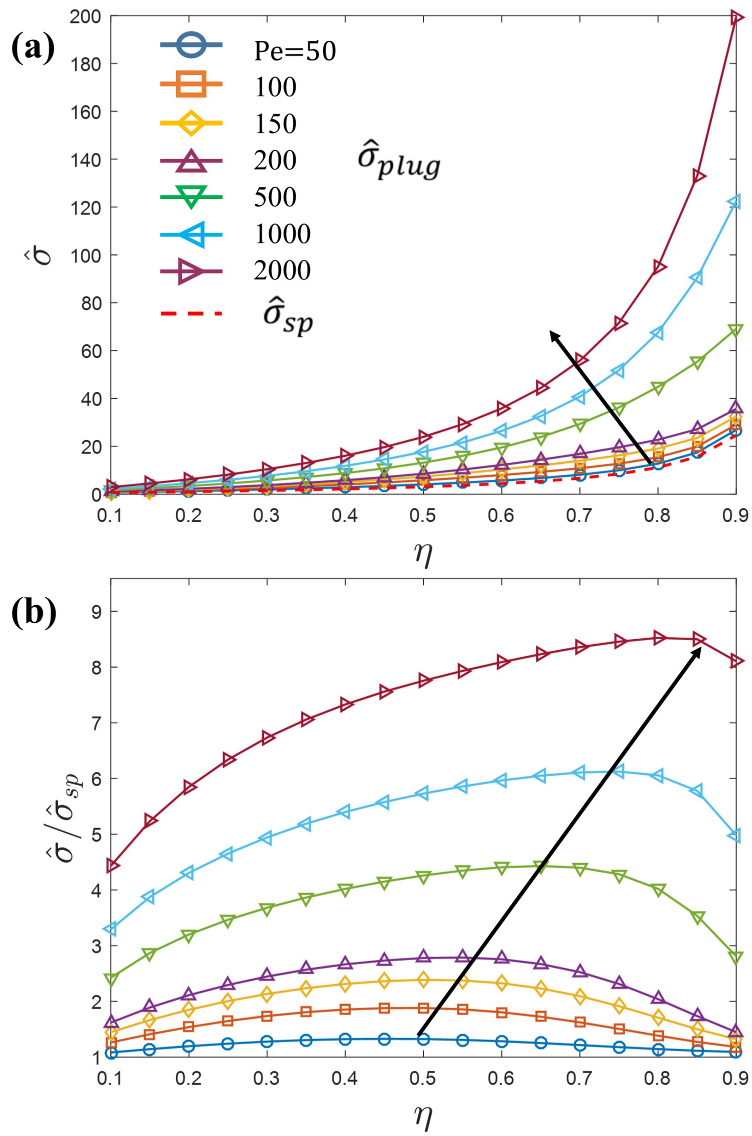

Figure 3.5: Influence of Peclet number Pe upon (a). the thermal conductance $\hat{\sigma}_{plug}$, (b). the enhancement by plug flow comparing to the single-phase flow heat transfer $\hat{\sigma}_{plug}/\hat{\sigma}_{sp}$. The arrows in figures mark the direction of increasing Pe. $\beta = 2$.

the mean temperature $\hat{\bar{T}}$ will no longer increase as well. Since the mixing index can be simplified into the plug mean temperature at ITB $\gamma = \frac{\hat{\bar{T}} - \hat{T}_{out,w}}{\hat{T}_{in,w} - \hat{T}_{out,w}} = \frac{\hat{\bar{T}} - 0}{1-0} = \hat{\bar{T}}$, the mean temperature $\hat{\bar{T}}$ can be used as the index to assure the thermal fields are fully developed during the simulations.

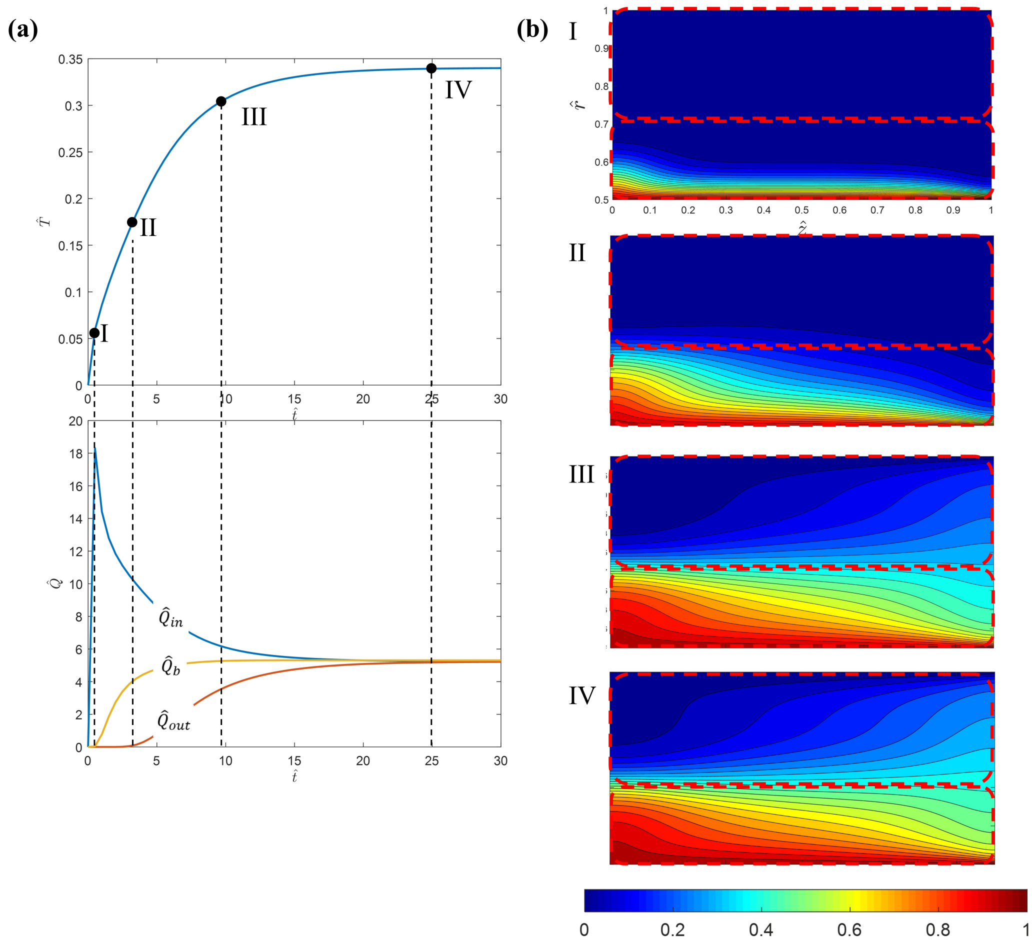

Figure 3.6: Heat transfer process at ITB, $(\beta, \eta, \mathrm{Pe}) = (2, 0.5, 100)$. (a). Variation of the mean temperature $\hat{\bar{T}}$, and the dimensionless heat flow at the inner wall $\hat{Q}_{in}$, at the outer wall $\hat{Q}_{out}$ and at the boundary between two vortexes $\hat{Q}_b$. The black solid points correspond to the examples shown in (b)., (b). (I) $\sim$ (IV) Sequence of dimensionless temperature $\hat{T}$ distribution at $\hat{t}_{\mathrm{I}\sim\mathrm{IV}} = (0.5, 3, 9.5, 25)$.

The thermal network for the iso-thermal boundary condition is then extracted and plotted in fig. 3.7 (b). Comparing to that under the inner iso-flux boundary condition in fig. 3.7 (a). the power source is changed from constant flux into constant temperature

$\hat{\bar{T}}_{out,w} = 1$. There exists both the resistance between the inner wall and the fluid, and that between the fluid and the outer wall since the outer wall is not adiabatic. The total resistance is thus $1/\hat{\sigma}_{in,w-f} + 1/\hat{\sigma}_{out,w-f} = (\hat{\sigma}_{in,w-f} + \hat{\sigma}_{out,w-f})/(\hat{\sigma}_{in,w-f}\hat{\sigma}_{out,w-f})$, which yields the overall plug conductance $\hat{\sigma}_{plug} = (\hat{\sigma}_{in,w-f}\hat{\sigma}_{out,w-f})/(\hat{\sigma}_{in,w-f} + \hat{\sigma}_{out,w-f})$ under the iso-thermal boundary condition. At the stage of the fully thermal developed field, there is zero flow into the capacitor $\hat{C}_{plug}$, which exactly corresponds to zero heat accumulation in the whole plug.

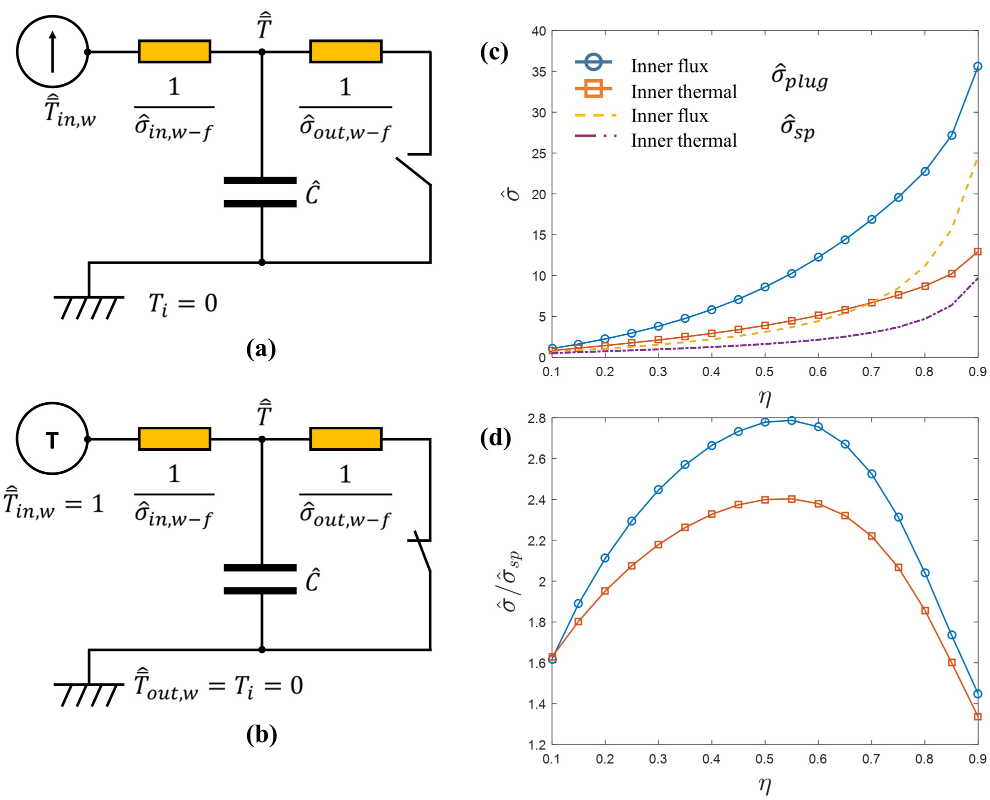

Figure 3.7: Comparison between IFB and ITB (a) (b). the thermal networks, (c). the thermal conductance $\hat{\sigma}_{plug}$, (d). the enhancement by plug flow comparing to the single-phase flow heat transfer $\hat{\sigma}_{plug}/\hat{\sigma}_{sp}$. The working condition is the same as in fig. 3.3.

The plug conductance, as well as the enhancement comparing to the single-phase flow, are then plotted in fig. 3.7 (c). and (d). respectively. It can be concluded that changing the boundary condition to the iso-thermal type only lowers the amplitude of the thermal conductance $\hat{\sigma}_{plug}$ and the enhancement $\hat{\sigma}_{plug}/\hat{\sigma}_{sp}$, while their trends versus varying working conditions like η are not much affected. The reason can be the existence of an additional resistor between the outer wall and the fluid $1/\hat{\sigma}_{out,w-f}$, which has been discussed above.

3.5 Heat transfer performance at the outer iso-flux boundaries (OFB), comparison to IFB

If the heat is loaded at the outer wall, the overall heat transfer performance should vary as well, because the heat path has reversed, and because the two vortexes are not symmetric to each other. In the thermal network (fig. 3.8 (a). and (b).), the overall plug conductance is not the same one at two boundary types. For the inner iso-flux boundary condition $\hat{\sigma}_{plug} = \hat{\sigma}_{in,w-f}$ is the conductance between the inner wall and the fluid, while $\hat{\sigma}_{plug} = \hat{\sigma}_{out,w-f}$ is that between the outer wall and the fluid for the outer iso-flux boundary condition.

The plug conductance for both boundary types are plotted in fig. 3.8 (c). that $\hat{\sigma}_{plug}$ is always higher under the outer iso-flux boundary condition. This is due to the stronger outer vortex with higher radial transport velocity (fig. 2.9) and higher capacity (fig. 2.6). The difference of $\hat{\sigma}_{plug}$ between two boundary types gradually decreases when η grows, because the difference between the two vortexes gradually diminishes.

In fig. 3.8 (d). it is found that the enhancement comparing to the single-phase flow $\hat{\sigma}_{plug}/\hat{\sigma}_{sp}$ is a decreasing function of the inner-outer radius ratio η under the outer iso-flux boundary condition. This is a result of both decreasing (1). the recirculation flux ($\hat{r}\hat{\bar{u}}_r$) (fig. 2.9), and (2). The capacity of the outer vortex $\hat{C}_{out,v}$ (fig. 2.6). When $\eta \to 1$ the two vortexes become nearly identical to each other, thus $\hat{\sigma}_{plug}/\hat{\sigma}_{sp}$ under two boundary types have a trend to converge with each other, both of which can be replaced using the results in a slit channel.

The results in this section enhance the fact that different thermal conductance and enhancement to the single-phase flow vary with the different boundary types [18], it also varies when the heat is loaded from the outside or the inside due to the asymmetric vortexes. Since the correlations for plug flow heat transfer is far away from being sufficient for designing the plug flow-based heat exchanger [59], if any correlations are to be proposed in the future work, these effects should be taken into consideration.

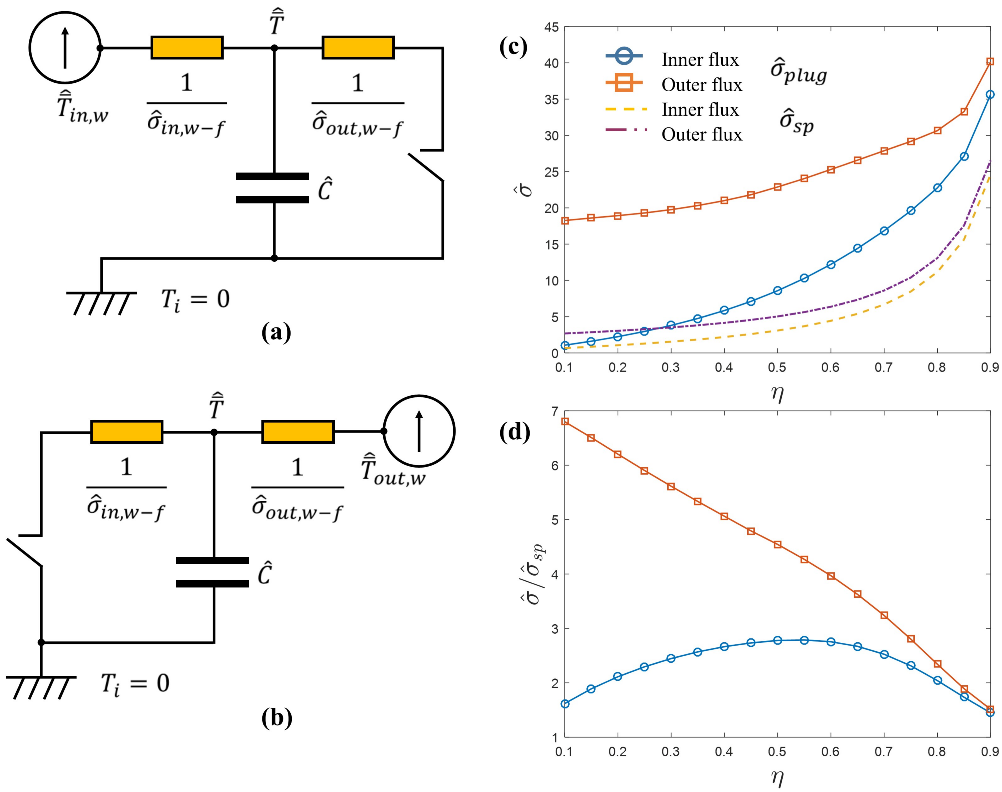

Figure 3.8: Comparison between IFB and OFB (a) ~ (b). the thermal networks, (c). the thermal conductance $\hat{\sigma}_{plug}$, (d). the enhancement by plug flow comparing to the single-phase flow heat transfer $\hat{\sigma}_{plug}/\hat{\sigma}_{sp}$. The working condition is the same as in fig. 3.3.

3.6 Results for steady heat transfer under fully developed stage

3.6.1 Simplification based upon control volume method

An interesting observation is in section 3.3.1, that the growth rate of $\hat{\bar{T}}$, $\hat{\bar{T}}_{in,w}$ and $\hat{\bar{T}}_{out,w}$ is identical at fully developed stage. It indicates a possibility that the conclusion for single phased flow mentioned in [68], that $\frac{\partial \hat{T}}{\partial \hat{Z}}$ is uniform inside the channel, also suits for the 2-D scenario in plug flow heat transfer. To examine that, the distribution of $\frac{\partial \hat{T}}{\partial \hat{t}}$ at the fully developed stage as below under the same condition as in fig. 3.2 is plotted out. The standard deviation of $\frac{\partial \hat{T}}{\partial \hat{t}}$ is also calculated.

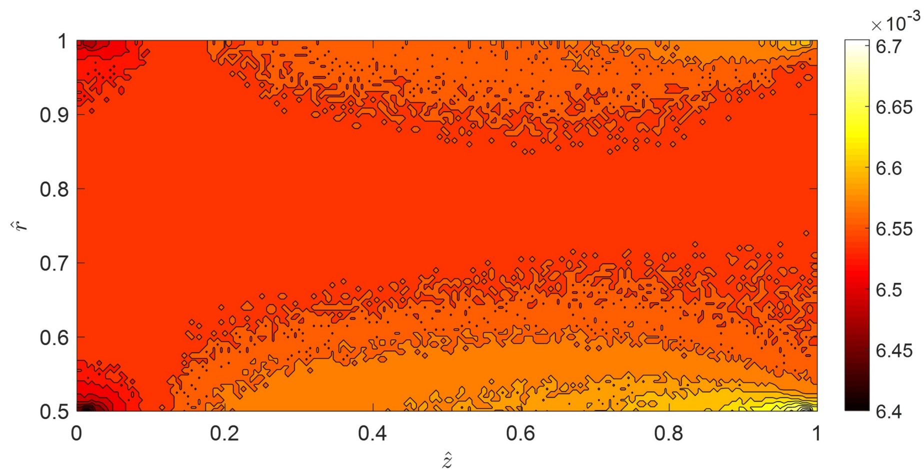

Figure 3.9: Temporal derivative of the thermal field $\frac{\partial \hat{T}}{\partial \hat{t}}$ at $\hat{t} = 50$,at IFB, all other parameters are same as in fig. 3.2

As shown in fig. 3.9, the distribution of $\frac{\partial \hat{T}}{\partial \hat{t}}$ is quite uniform, the value is about $6.7 \times 10^{-3} = \frac{2\times 0.5}{100\times(1+0.5)} = \frac{2\eta}{\mathrm{Pe}(1+\eta)}$, and the standard deviation of $\frac{\partial \hat{T}}{\partial \hat{t}}$ is as low as 1.4431×10^{-5}, which is 0.2202% of the mean value of $\frac{\partial \hat{T}}{\partial \hat{t}}$. This can be a validation to the hypothesis that the uniform distribution of $\frac{\partial \hat{T}}{\partial \hat{t}}$ is obtained in the plug flow heat transfer under the fully developed stage. With the help of above conclusion, a demonstration of deriving the solution of fully developed thermal field at IFB will be presented below, while the other two boundary conditions can be processed using a similar fashion.

At IFB, the growth rate can be calculated by the control volume method, which is $\frac{2\eta}{\mathrm{Pe}(1+\eta)}$. The governing equation under fully developed stage is

$$\frac{2\eta}{\mathrm{Pe}(1-\eta^2)} + (1-\eta)(\frac{\hat{u}_r}{\hat{r}}\frac{\partial(\hat{T}\hat{r})}{\partial\hat{r}} + \hat{u}_z\frac{\partial\hat{T}}{\partial\hat{z}}) = \frac{(1-\eta)^2}{\mathrm{Pe}}[\frac{1}{\hat{r}}\frac{\partial}{\partial\hat{r}}(\hat{r}\frac{\partial\hat{T}}{\partial\hat{r}}) + \frac{\partial^2\hat{T}}{\partial\hat{z}^2}]. \tag{3.31}$$

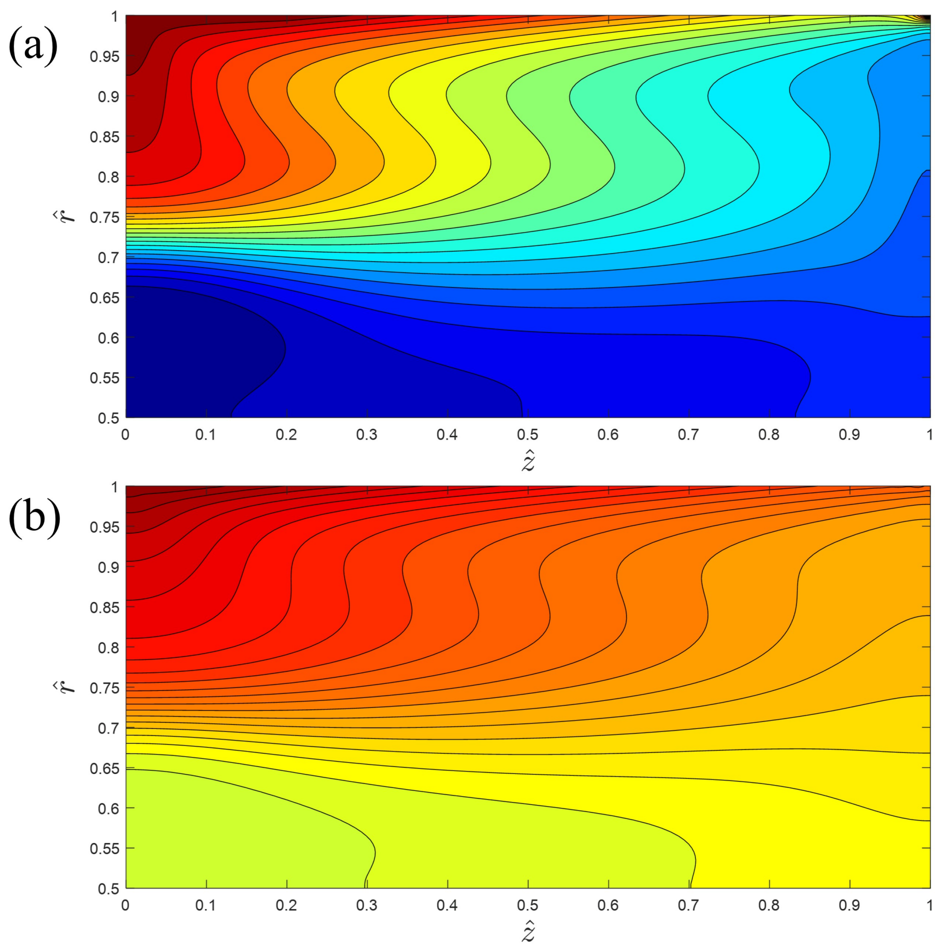

Figure 3.10: Comparison between (a). thermal field under simplified model for fully developed stage, and (b). that at $\hat{t} = 60$ using transient method, at OFB, all other parameters are same as in fig. 3.2

Where the definition for the the dimensionless temperature $\hat{T} = \frac{T}{\Delta T_{std}} - \frac{2\eta}{\mathrm{Pe}(1+\eta)}\hat{t} - const$, which is independent of the developing time $\hat{t}$. As mentioned earlier, when evaluating the heat transfer performance the relative shape, or say the spatial distribution instead

Range of Pe	SOR
$0 \sim 500$	$1-(3/2500)\mathrm{Pe}$
$500 \sim 1000$	$200/\mathrm{Pe}-\mathrm{Pe}/4000+1/8$
>1000	$75/\mathrm{Pe}$

Table 3.2: Set-up for relaxation ratio (SOR) for steady state heat transfer

of the absolute value is important. Thus, taking away the term $\frac{2\eta}{\mathrm{Pe}(1+\eta)}\hat{t}$ will not effect the calculation of, for example, $\hat{\sigma}_{in,w-f}$ in eq. (3.25). Other boundary conditions are the same as in eq. (3.12), though it should be noted that there lack the boundary condition for temperature values. To bound the system, the temperature at a certain location is artificially set to zero ($\hat{T}(\eta,0)=0$). Then eq. (3.31) is discretized using the finite volume method (details provided in table 3.1), though the time step is not involved in this problem. The equation is iterated using the Jacobi method with a relaxation ratio (SOR) based upon Pe. Details about SOR are provided in table 3.2.

A comparison between the result of this method at OFB and that from the transient method at $\hat{t}=60$ is plotted as below. There exist nearly no difference in the relative shape between two contours, the results based on spatial distribution such as $\hat{\sigma}$ will not be affected at all. Thus this can be treated as a validation.

With the help of this simplified model, calculating the thermal field under $3\times19\times19\times11=11,913$ kinds of commonly seen working conditions (coefficients are for numbers of boundary conditions, β, η, Pe respectively) was conducted in an acceptable time, and the results are stored in a database for later study.

3.6.2 Some results and potential future design work

A popular dimensionless parameter Nusselt number (Nu) is chosen to describe the results under all $11,913$ working conditions. The definition of Nu is

$$\mathrm{Nu}=\frac{hD_h}{k}. \tag{3.32}$$

Where h is the convective heat transfer coefficient, and $D_h=\frac{4\pi(r_1^2-r_2^2)}{2\pi(r_1+r_2)}=2(r_1-r_2)$. For IFB and ITB,

$$h = \frac{\int_0^l (-k\frac{\partial T}{\partial r})_{r=r_1} \mathrm{d}z}{\int_0^l (T_{in,w} - \bar{T})_{r=r_1} \mathrm{d}z}. \tag{3.33}$$

For OFB,

$$h = \frac{\int_0^l (-k\frac{\partial T}{\partial r})_{r=r_2} \mathrm{d}z}{\int_0^l (T_{in,w} - \bar{T})_{r=r_2} \mathrm{d}z}. \tag{3.34}$$

Substitute eqs. (3.4) to (3.6) and (3.24) into eqs. (3.33) and (3.34)

For IFB,

$$\mathrm{Nu} = \frac{2}{\bar{T}_{in,w} - \hat{\bar{T}}}. \tag{3.35}$$

For ITB,

$$\mathrm{Nu} = -\frac{2}{\beta} \frac{\int_0^{\hat{l}} (\frac{\partial \hat{T}}{\partial \hat{r}})_{\hat{r}=\eta} \mathrm{d}\hat{z}}{1 - \hat{\bar{T}}}. \tag{3.36}$$

For OFB,

$$\mathrm{Nu} = \frac{2}{\bar{T}_{out,w} - \hat{\bar{T}}}. \tag{3.37}$$

It is easily validated that $\mathrm{Nu}/\mathrm{Nu}_{sp} = \sigma/\sigma_{sp}$, because one can derive from, for instance, eqs. (3.25) and (3.35) that $\mathrm{Nu} = f(\eta)\sigma$ and $\mathrm{Nu}_{sp} = f(\eta)\sigma_{sp}$, where $f(\eta)$ only depends on the boundary for sampling. Thus, mathematically speaking its equivalent to use either of them to describe the heat transfer enhancement. Here Nu is chosen only due to its popularity among engineers and there is no need to analyze the thermal network in this subsection. The distribution of Nu versus β and η is plotted using the mesh plot function in MATLAB 2016A, where each subplot is under a certain Pe.

These plots along with the datasets can be quoted in the future design work, which is preferred especially for optimization/inverse problem. For example, when Pe for a particular working condition is near anyone in our database, one can efficiently use the interpolation to obtain the required outputs. Even if Pe exceeds any of those in the database, calculating the thermal field is quite fast with the help of analytical flow field solution and our simplified

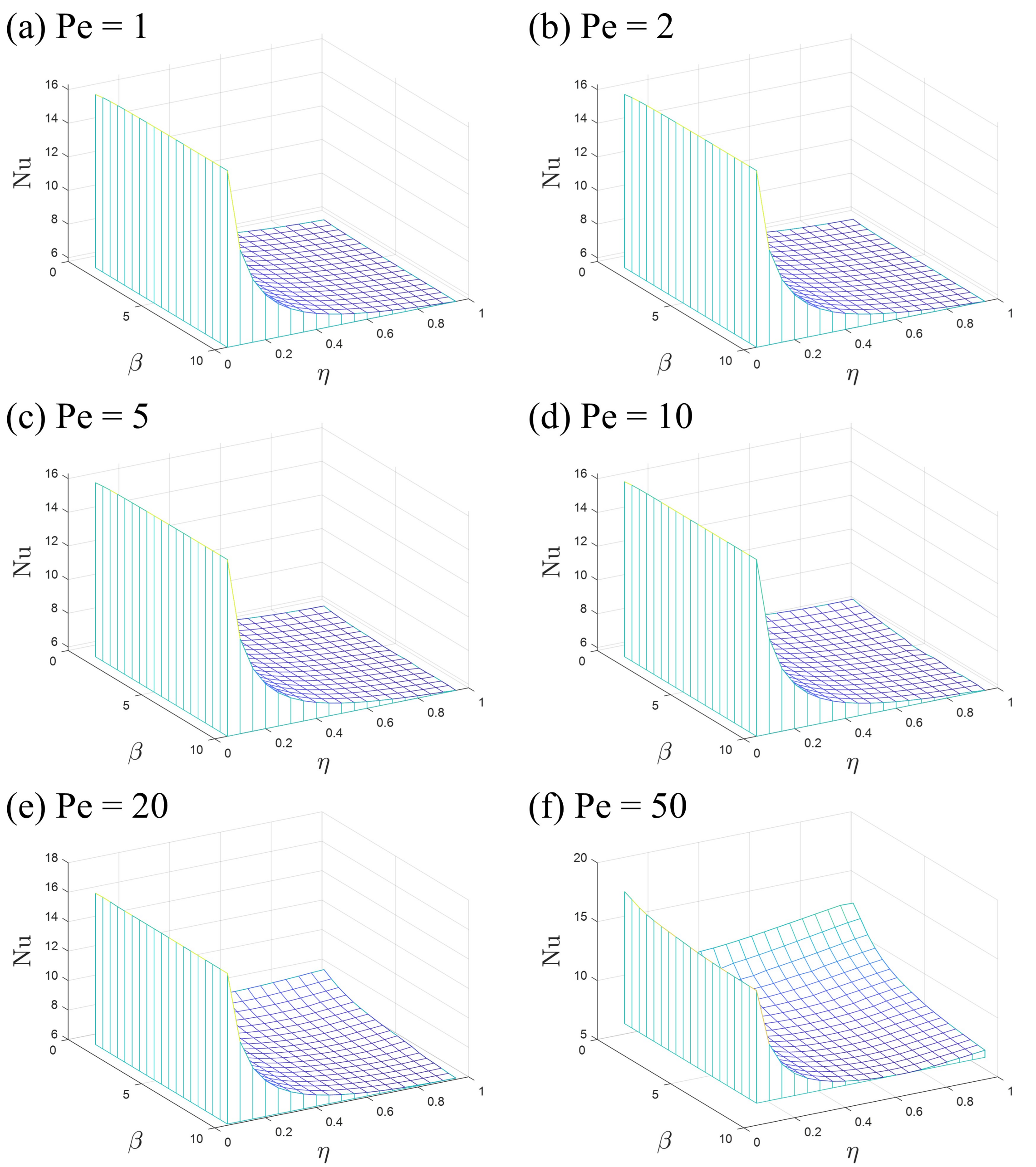

Figure 3.11: I of II: The sequence of plots for Nu under Pe $= 1, 2, 5, 10, 20, 50$ at IFB condition.

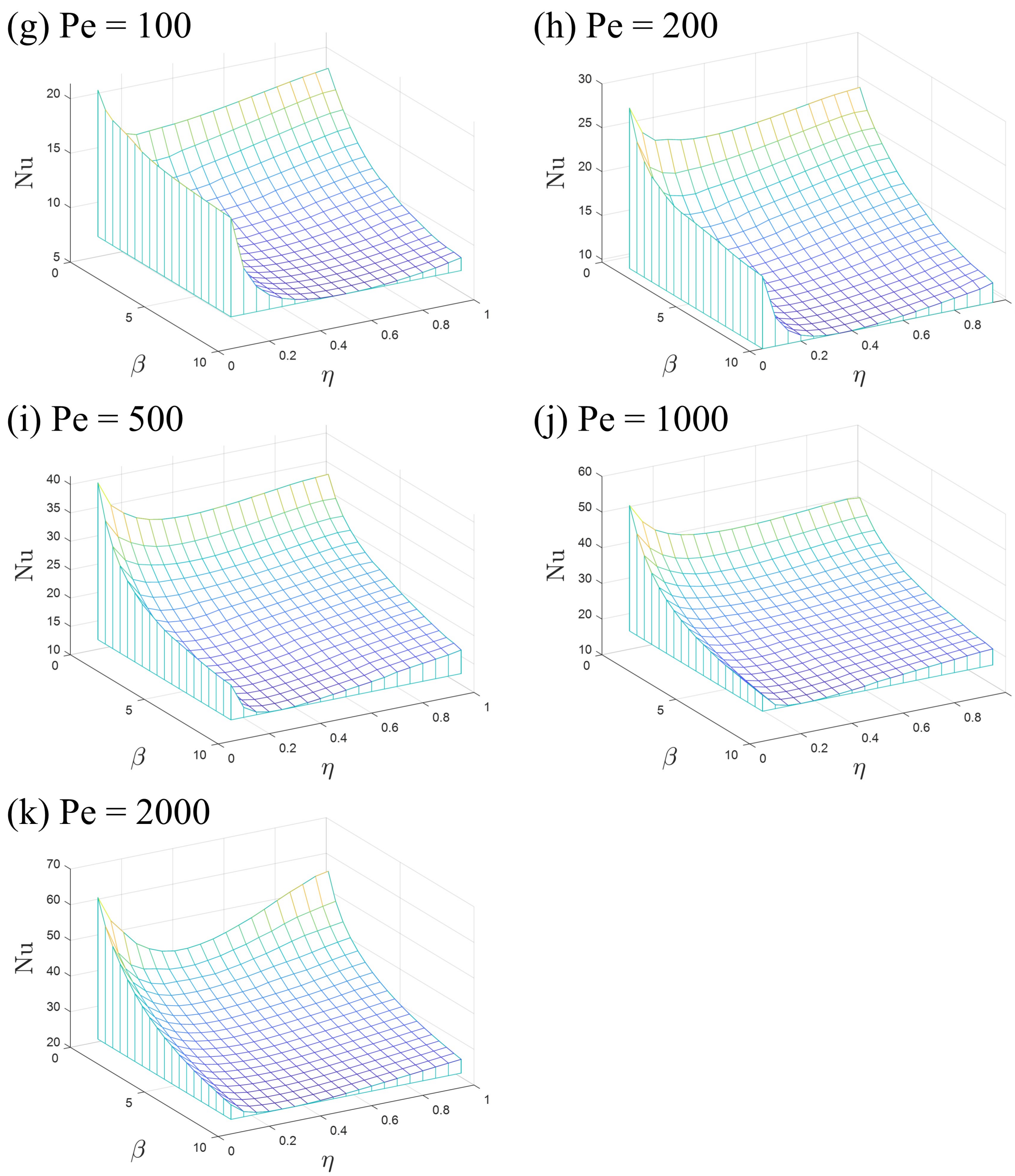

Figure 3.12: II of II: The sequence of plots for Nu under Pe $= 100, 200, 500, 1000, 2000$ at IFB condition.

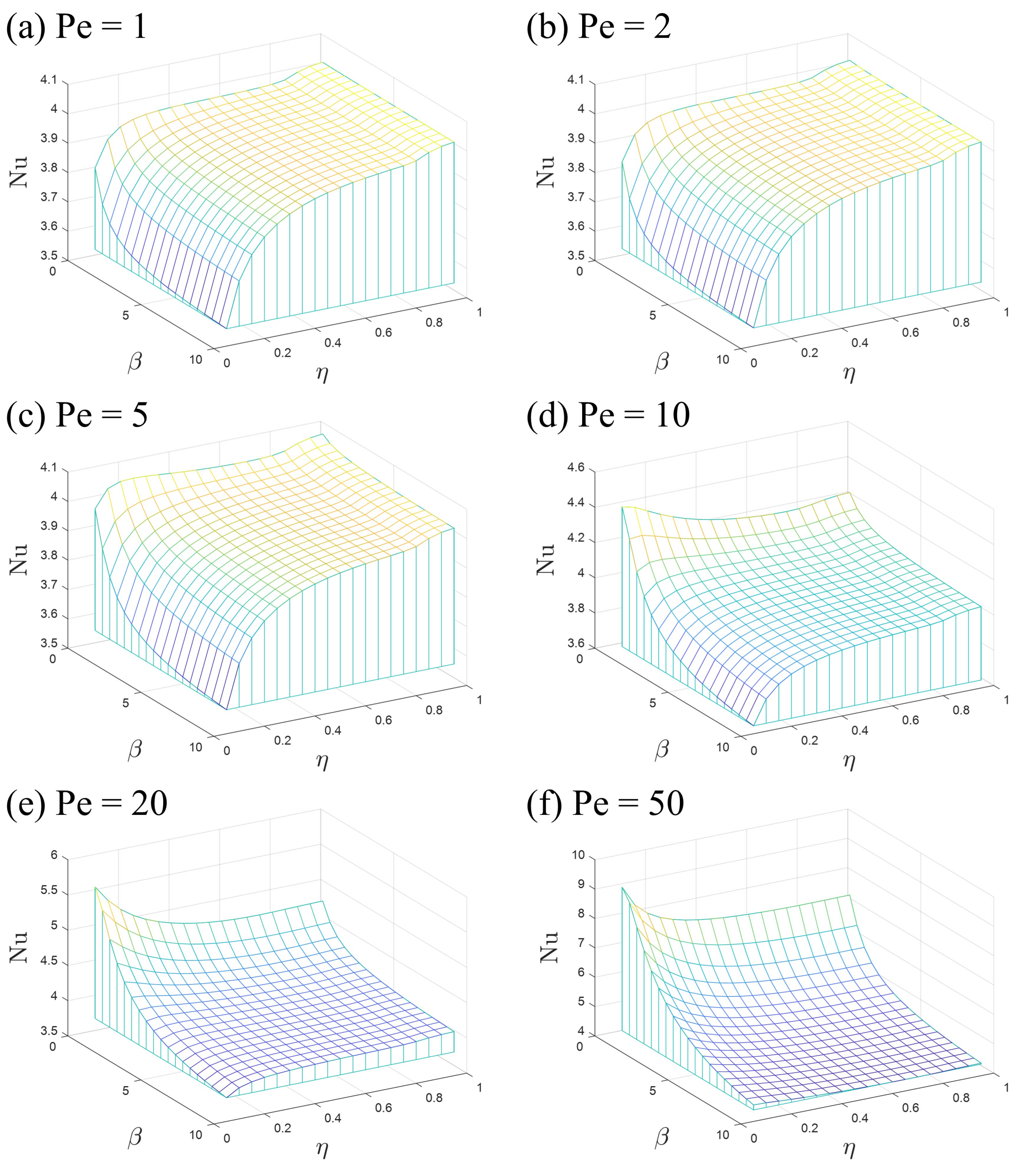

Figure 3.13: I of II: The sequence of plots for Nu under Pe $= 1, 2, 5, 10, 20, 50$ at ITB condition.

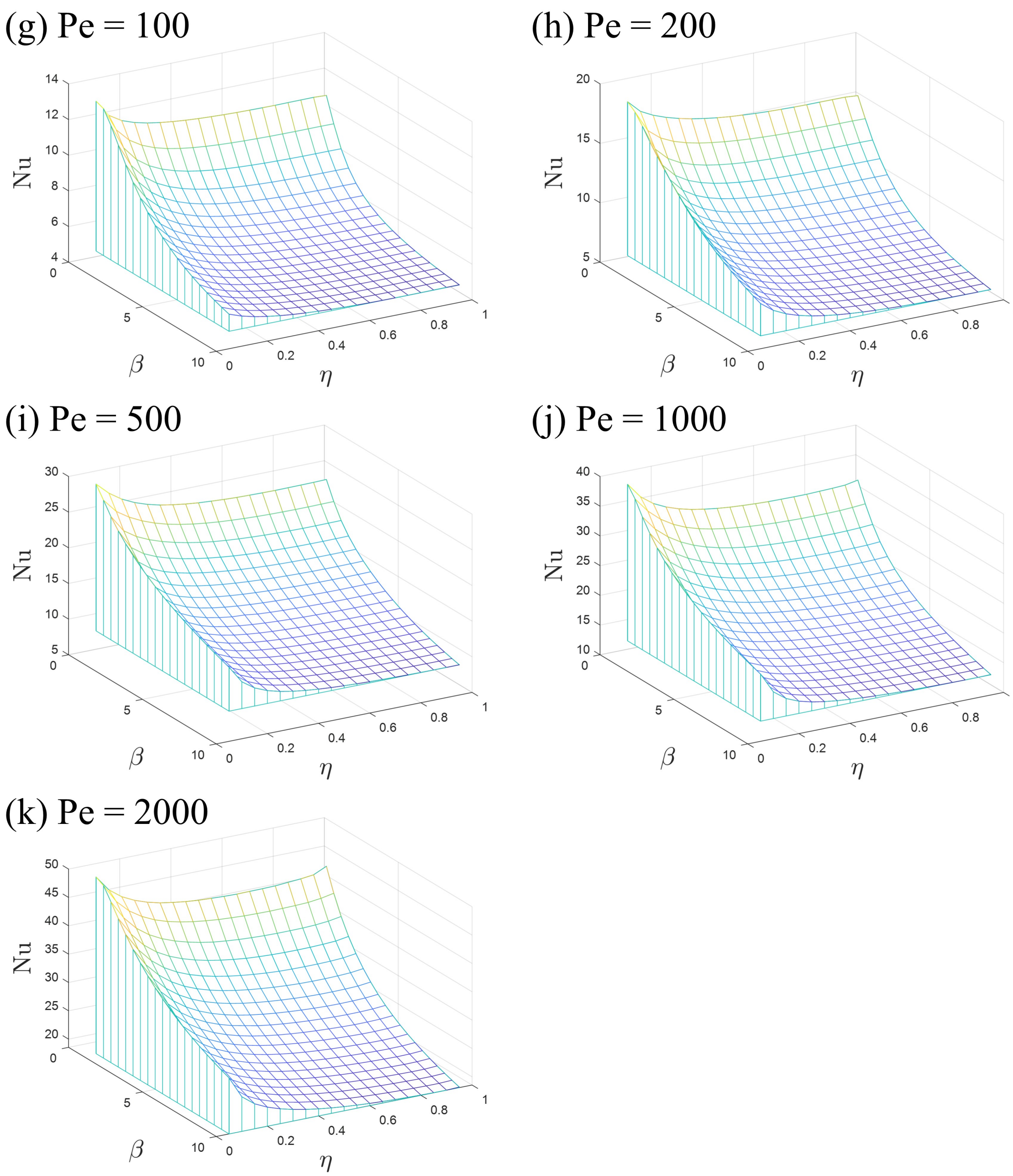

Figure 3.14: II of II: The sequence of plots for Nu under Pe = 100, 200, 500, 1000, 2000 at ITB condition.

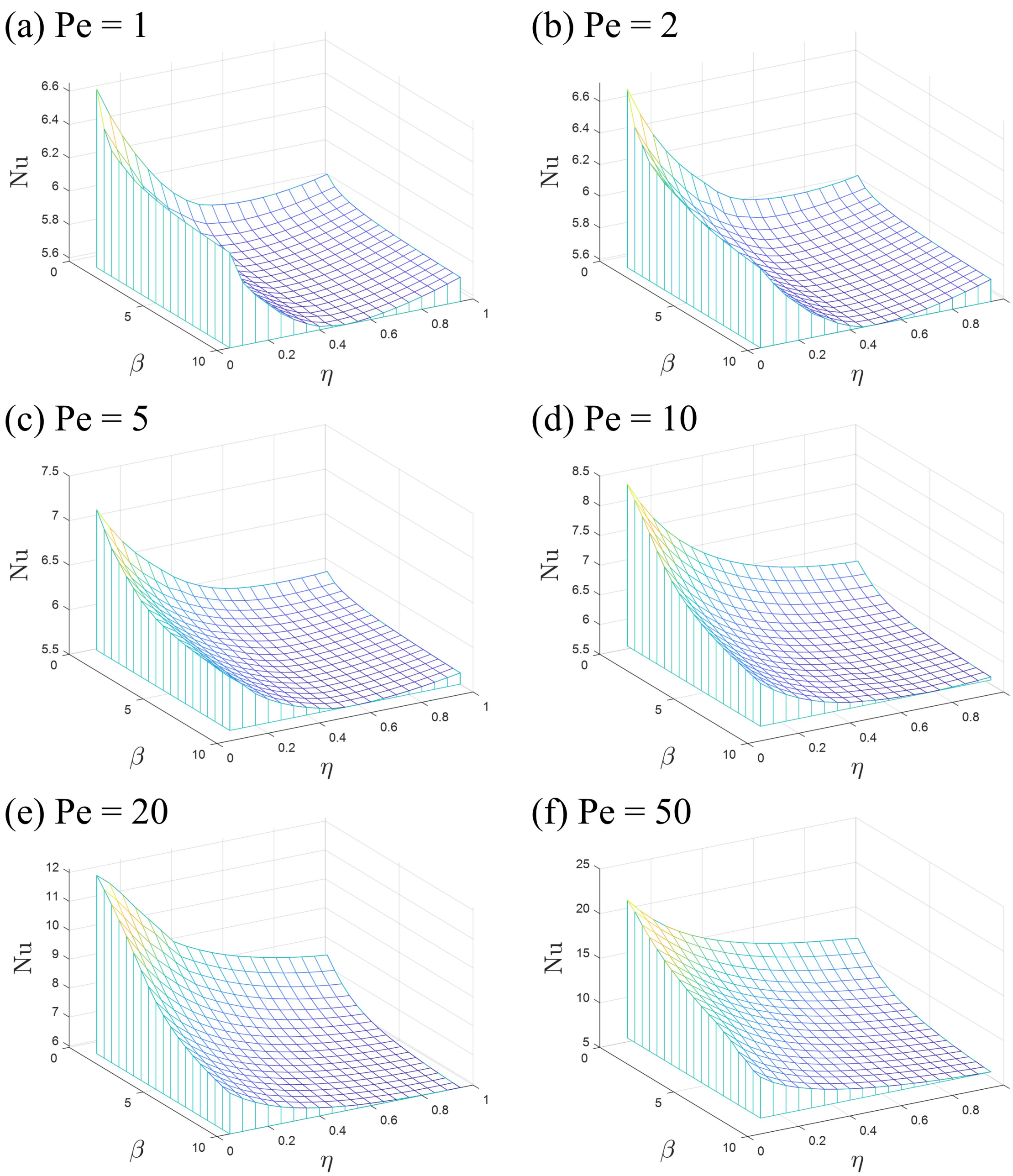

Figure 3.15: I of II: The sequence of plots for Nu under Pe = $1, 2, 5, 10, 20, 50$ at OFB condition.

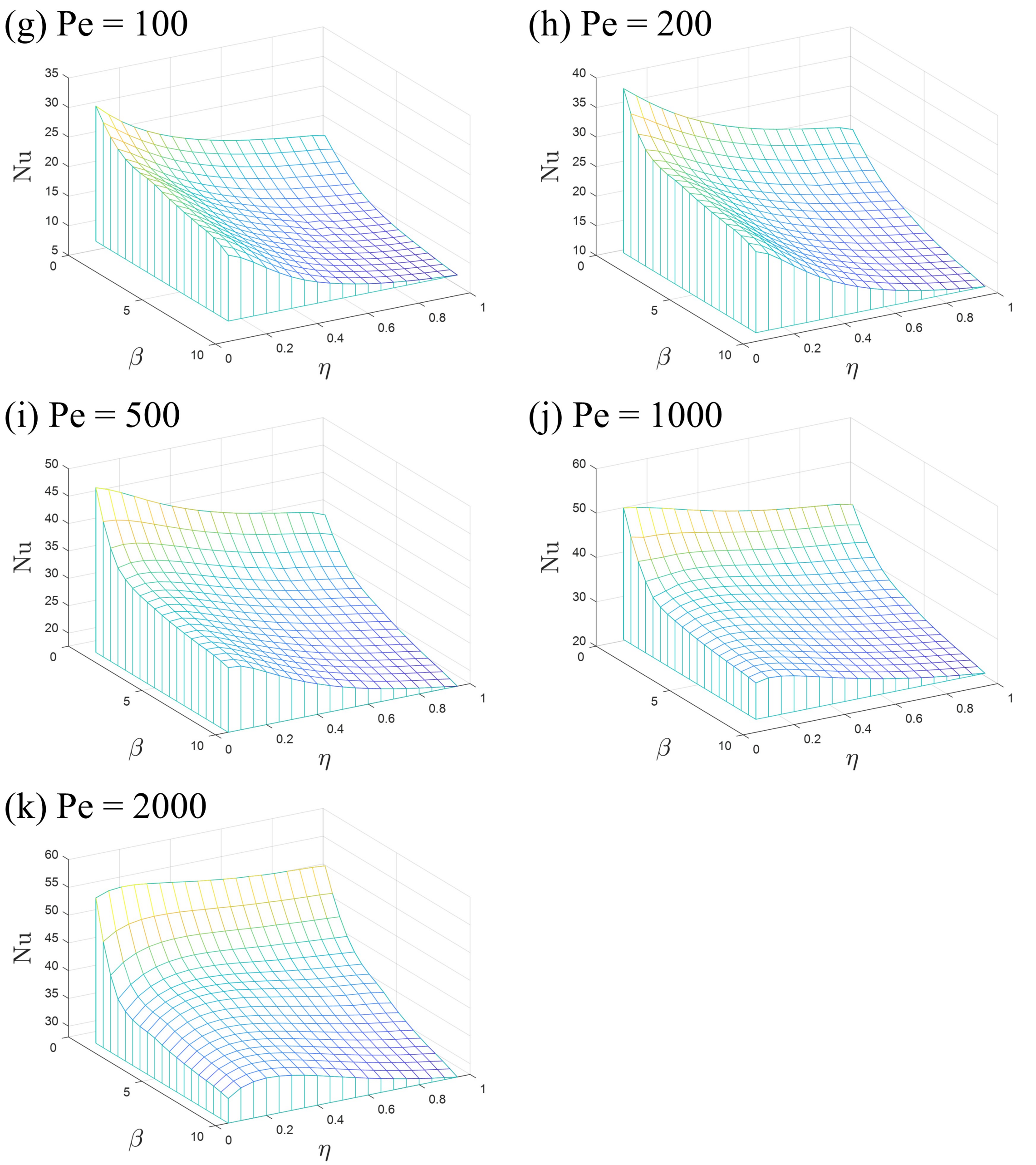

Figure 3.16: II of II: The sequence of plots for Nu under Pe $= 100, 200, 500, 1000, 2000$ at OFB condition.

model. The advantage would be more evident with the increasing amounts of working conditions needed in order to search for an optimal design.

3.7 Summary of this chapter

The numerical simulation for the heat transfer process at three kinds of boundary conditions in gas-liquid plug flow in tube-in-tube microchannels is carried out in MATLAB 2016A. The heat transfer process is analyzed and extracted into simplified thermal networks. The mixing index γ is used to assure the simulation is continuing until the thermal field is fully developed. At the fully thermal developed field, the influences of the plug length β, the inner-outer radius ratio η and the Peclet number Pe upon the plug thermal resistance $\hat{\sigma}_{plug}$ and upon the enhancement to the single-phase flow $\hat{\sigma}_{plug}/\hat{\sigma}_{sp}$ are investigated. The difference between heat transfer performance between the inner iso-flux boundaries and other two boundaries are presented and explained using their thermal networks. Summary of findings are listed as follows:

- The process of heat transfer inside the plug flow at a certain boundary type can be simplified using a thermal network. Different boundary conditions determine whether some routes containing resistors should be cut, they also determine the location and the type of the heat source, as well as the orientation of the heat transfer path.

- At the inner iso-flux condition (IFB), growing η leads to the higher thermal capacity ratio of the inner vortex $\hat{C}_{in,v}/\hat{C}_{out,v}$ as well as higher recirculation flux $(\hat{r}\hat{\hat{u}}_r)$ at the inner vortex, which lowers the temperature gap between the inner wall and the mean value of the plug $\hat{\hat{T}}_{in,w} - \hat{\hat{T}}$ and increases the thermal conductance $\hat{\sigma}_{plug}$. The variation of the enhancement to single-phase flow heat transfer with varying η is not singular, and the peak enhancement is reached at about $\eta = 0.55$ when $(\beta, \mathrm{Pe}) = (2, 100)$.

- Longer plugs have lower $\hat{\sigma}_{plug}$ and $\hat{\sigma}_{plug}/\hat{\sigma}_{sp}$, which is caused by lower $(\hat{r}\hat{\hat{u}}_r)$ and dramatically longer recirculation period $\hat{t}_{rec}$. With growing β, the η corresponding to the peak of $\hat{\sigma}_{plug}/\hat{\sigma}_{sp}$ also increases.

- Higher Pe increases the thermal capacity of the whole plug $\hat{C}_{plug}$, which leads to more portion of heat being directly advected into the plug and enhances the combining effect of advection and diffusion, $\hat{\sigma}_{plug}$ and $\hat{\sigma}_{plug}/\hat{\sigma}_{sp}$ are enhanced, therefore.

- At the iso-thermal boundary condition (ITB), lower amplitudes of both $\hat{\sigma}_{plug}$ and $\hat{\sigma}_{plug}/\hat{\sigma}_{sp}$ are reached comparing to those at the inner iso-flux boundary condition. However, their trends versus different working conditions like η are not affected. This variance in the amplitudes is caused by an additional resistor between the outer wall and the fluid $1/\hat{\sigma}_{out,w-f}$.

- At the outer iso-flux boundaries (OFB), both $\hat{\sigma}_{plug}$ and $\hat{\sigma}_{plug}/\hat{\sigma}_{sp}$ are always higher than those under the inner iso-flux boundary condition, because both the capacity of the outer vortex $\hat{C}_{out,v}$ and the recirculation flux $(\hat{r}\hat{\bar{u}}_r)$ of the outer vortex are larger than those of the inner vortex. When $\eta \to 1$, all these parameters tend to converge at both IFB and OFB because now the plug is like the plug inside of a slit channel. The difference between these three boundary types enhances the fact that different correlations should be developed when the boundary condition type changes, or the heat transfer path reverses. It can be a focus of the future work.

- A simplified model for heat transfer at the fully thermal developed stage was introduced to save simulation time. About $12,000$ cases were simulated in an acceptable time, Nusselt number of which were extracted and mesh plotted for design work need in the future.

Chapter 4

Analytical study of liquid-liquid plug flow in circular microchannel

The liquid-liquid plug flow in microchannel has different boundary conditions comparing to the gas-liquid plug flow. In gas-liquid flow, the viscous force at the two ends of the liquid plug is neglected since the low viscosity of the gas plug. In liquid-liquid plug flow, this interfacial interaction between the two plugs can no longer be ignored. Also, it makes the boundary condition, along with the analytical solutions, more complicated.

In this chapter, firstly the focus is on the mathematical modification towards the boundary conditions, as well as towards the process of obtaining the analytical solutions in the liquid-liquid plug flow in the microchannel with a round cross-section. Then, some discussions are made upon phenomena caused by the interface interaction. Finally, the influence of the viscosity ratio of the two plugs upon the skin friction coefficient will be presented.

4.1 Mathematic modeling

4.1.1 Governing equations and boundary conditions

Apply the same basic assumptions in chapter 2, and use two moving coordinators sticking to each plug respectively, the liquid-liquid plug flow can be modeled using two PDEs with the plug index $i = 1, 2; j = 2, 1$ in the substrate respectively. Here the nondimensionalization process has been skipped since it is basically the same as in chapter 2.

$$\{\hat{\mathcal{L}}^4_{-1}\hat{\psi}\}_i = 0, \tag{4.1}$$

Two of the assumptions about boundary conditions can be still adapted from chapter 2:

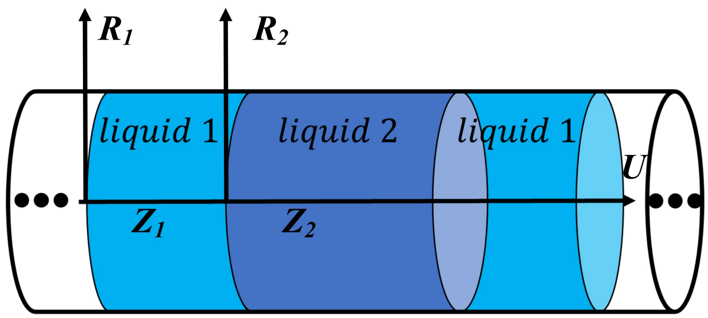

Figure 4.1: Schematic show for liquid-liquid plug flow in microchannel with round cross-section.

1. The stream function is zero at all boundaries, 2. there is no slip between the walls and liquid plug.

$$\{\hat{\psi}(0,\hat{r})\}_i = 0,\ \{\hat{\psi}(\beta,\hat{r})\}_i = 0,\ \{\hat{\psi}(\hat{z},1)\}_i = 0 \tag{4.2}$$

$$\{\frac{1}{\hat{r}}\frac{\partial\hat{\psi}}{\partial\hat{r}}(\hat{z},1)\}_i = -1, \tag{4.3}$$

However, at the two ends of each plug, there exists viscous force due to the velocity gradients. They can be described using: 1. continuity for velocities at two sides of the interface, 2. continuity for the viscous force at two sides of the interface.

$$\{\frac{1}{\hat{r}}\frac{\partial\hat{\psi}}{\partial\hat{z}}(0,\hat{r})\}_i = \{\frac{1}{\hat{r}}\frac{\partial\hat{\psi}}{\partial\hat{z}}(\beta,\hat{r})\}_j, \tag{4.4}$$

$$\frac{\mu_i}{\mu_j}\{\frac{1}{\hat{r}}\frac{\partial^2\hat{\psi}}{\partial\hat{z}^2}(0,\hat{r})\}_i = \{\frac{1}{\hat{r}}\frac{\partial^2\hat{\psi}}{\partial\hat{z}^2}(\beta,\hat{r})\}_j. \tag{4.5}$$

From eqs. (4.4) and (4.5) it can be seen that PDEs for plug 1 and 2 are coupled together, thus two systems should be solved simultaneously.

4.1.2 Analytical solution

To obtain the series solution of eqs. (4.1) to (4.5), similar fashion can be found from a more general problem from [4]: the Stokes flow in a 2-D cavity given boundary conditions on both top/bottom walls and front/rear walls. In this work, the authors used 2 infinite series under 2 orthogonal basis functions of x, y respectively to describe the flow field. Any distribution in the x direction, such as boundary condition on the top or on the bottom, has an unique position in the functional space containing the orthogonal basis $\boldsymbol{M}(x) = \langle M_1(x), M_2(x)\cdots\rangle = \langle M_m(x)\rangle$. Where $\boldsymbol{M}(x)$ is found through the eigenvalue problem. Then the index function for each basis can be found by substituting the basis into original PDEs, denoted as $\boldsymbol{g}(y) = \langle g_1(y), g_2(y)\cdots\rangle = \langle g_m(y)\rangle$. Coefficients for $\boldsymbol{g}(y)$ can be bounded by getting the inner product of the boundary condition and each basis $M_m(x)$ respectively, because of the orthogonality, only the terms of series m will be kept. Similarly, any distribution in the y direction has an unique position in the functional space containing the orthogonal basis $\boldsymbol{L}(y) = \langle L_l(y)\rangle$, which comes with an index function in this space $\boldsymbol{f}(x) = \langle f_l(x)\rangle$. The sum of 2 infinite series $\boldsymbol{M}(x)\cdot\boldsymbol{g}(y) + \boldsymbol{L}(y)\cdot\boldsymbol{f}(x)$ thus can fit any distributions on both direction x, y, thus can fit any given boundary conditions on both top/bottom and front/rear walls.

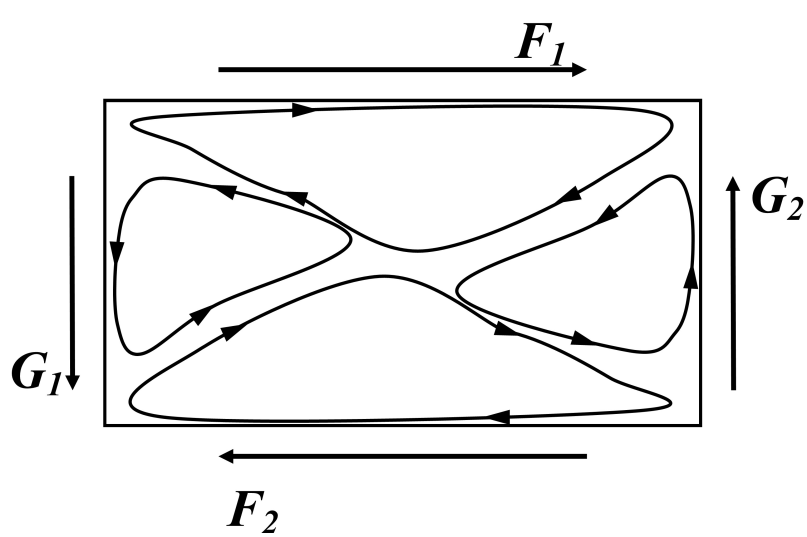

Figure 4.2: Schematic show for Stokes flow in a cavity with moving walls, a demonstration of the problem in [4]. $\boldsymbol{F}, \boldsymbol{G}$ are generic boundary conditions.

Thus here the sum of 2 infinite series is used to describe the flow field,

$$\hat{\psi} = \boldsymbol{M}(\hat{r}) \bullet \boldsymbol{g}(\hat{z}) + \boldsymbol{L}(\hat{z}) \bullet \boldsymbol{f}(\hat{r}).$$

The orthogonal basis $\boldsymbol{L}(\hat{z})$ must obey

$$\frac{\partial^2}{\partial \hat{z}^2}\boldsymbol{L} = -\boldsymbol{\Omega}^2\boldsymbol{L}, \tag{4.6}$$

where $\boldsymbol{\Omega}$ is the eigenvalue matrix,

$$\boldsymbol{\Omega} = \begin{pmatrix} \omega_1 & & \\ & \omega_2 & \\ & & \ddots \end{pmatrix}.$$

The boundary condition for this set of basis is

$$\boldsymbol{L}(0) = \boldsymbol{L}(\beta) = \boldsymbol{0}. \tag{4.7}$$

The basis from eqs. (4.6) and (4.7) is $\boldsymbol{L}(\hat{z}) = \langle \sin(\omega_1\hat{z}), \sin(\omega_2\hat{z}) \cdots \rangle = \langle \sin(\omega_l\hat{z}) \rangle$, where $\omega_l = l\pi/\beta$. This has been obtained already in chapter 2. Then the index vector should obey

$$(\frac{\partial^2}{\partial \hat{r}^2} - \frac{1}{\hat{r}}\frac{\partial}{\hat{r}} - \boldsymbol{\Omega}^2)(\frac{\partial^2}{\partial \hat{r}^2} - \frac{1}{\hat{r}}\frac{\partial}{\hat{r}} - \boldsymbol{\Omega}^2)\boldsymbol{f} = \boldsymbol{0}. \tag{4.8}$$

From eq. (4.8), the index function can be obtained

$$\boldsymbol{f}(\hat{r}) = \langle f_l(\hat{r}) \rangle = \langle \begin{pmatrix} \hat{r}\mathrm{I}_1(\omega_l\hat{r}) \\ \hat{r}^2\mathrm{I}_2(\omega_l\hat{r}) \end{pmatrix} \bullet \begin{pmatrix} E_l \\ F_l \end{pmatrix} \rangle,$$

which is part of that in chapter 2. The terms of $\hat{r}\mathrm{K}_1(\omega_l\hat{r}), \hat{r}^2\mathrm{K}_2(\omega_l\hat{r})$ are dropped because here the flow is in the circular tube in stead of concentric tube, and these terms approach the infinity when $\hat{r} = 0$.

The orthogonal basis in $\hat{r}$ direction can also be found in a similar fashion, which is

$$(\frac{\partial^2}{\partial \hat{r}^2} - \frac{1}{\hat{r}}\frac{\partial}{\hat{r}})\boldsymbol{M} = -\mathbf{X}^2\boldsymbol{M}, \tag{4.9}$$

where the eigenvalue matrix is

$$\mathbf{X} = \begin{pmatrix} \chi_1 & & \\ & \chi_2 & \\ & & \ddots \end{pmatrix}.$$

The boundary condition is

$$\boldsymbol{M}(0) = \boldsymbol{M}(1) = \mathbf{0}. \tag{4.10}$$

The solution of eqs. (4.9) and (4.10) is $\boldsymbol{M}(\hat{z}) = \langle \hat{r}\mathrm{J}_1(\chi_1\hat{r}), \hat{r}\mathrm{J}_1(\chi_2\hat{r})\cdots\rangle = \langle \hat{r}\mathrm{J}_1(\chi_m\hat{r})\rangle$, where χ_m is the mth zero root of $\mathrm{J}_1(\chi)$ and J_ν is the νth order of Bessel function of the first kind. The index vector here obeys

$$(\frac{\partial^2}{\partial\hat{z}^2} - \mathbf{X}^2)(\frac{\partial^2}{\partial\hat{z}^2} - \mathbf{X}^2)\boldsymbol{g} = \mathbf{0}. \tag{4.11}$$

From eq. (4.11), the index function can be obtained

$$\boldsymbol{g}(\hat{z}) = \langle g_m(\hat{z})\rangle = \langle \begin{pmatrix} \sinh(\chi_m\hat{z}) \\ \cosh(\chi_m\hat{z}) \\ \hat{z}\sinh(\chi_m\hat{z}) \\ \hat{z}\cosh(\chi_m\hat{z}) \end{pmatrix} \boldsymbol{\cdot} \begin{pmatrix} A_m \\ B_m \\ C_m \\ D_m \end{pmatrix} \rangle.$$

Thus, the universal solution is the sum of 2 series,

$$\begin{aligned} \hat{\psi} = \boldsymbol{M}(\hat{r}) \boldsymbol{\cdot} \boldsymbol{g}(\hat{z}) + \boldsymbol{L}(\hat{z}) \boldsymbol{\cdot} \boldsymbol{f}(\hat{r}) = \sum_{l=1}^{\infty} \sin(\omega_l\hat{z})[E_l\hat{r}\mathrm{I}_1(\omega_l\hat{r}) + F_l\hat{r}^2\mathrm{I}_2(\omega_l\hat{r})] \\ + \sum_{m=1}^{\infty} \hat{r}\mathrm{J}_1(\chi_m\hat{r})[A_m\sinh(\chi_m\hat{z}) + B_m\cosh(\chi_m\hat{z}) + C_m\hat{z}\sinh(\chi_m\hat{z}) + D_m\hat{z}\cosh(\chi_m\hat{z})], \end{aligned} \tag{4.12}$$

where $A \sim F$ are constant coefficients. Substitute eq. (4.12) into boundary conditions eqs. (4.2) to (4.5), then apply the finite Fourier transformation eq. (2.16) when dealing with distribution in $\hat{z}$ direction, and apply the Hankel transformation (defined below) when dealing with distribution in $\hat{r}$ direction.

$$\mathcal{H}_m[\hat{\psi}] = \int_0^1 \hat{\psi} \mathrm{J}_1(\chi_m \hat{r}) \mathrm{d}\hat{r}. \tag{4.13}$$

The zero value for stream function on the wall,

$$\{E_l \mathrm{I}_1(\omega_l) + F_l \mathrm{I}_2(\omega_l)\}_i = 0. \tag{4.14}$$

The zero value for stream function on the front/rear ends of the plug,

$$\{B_m\}_i = 0,\ \{A_m \sinh(\chi_m \beta) + C_m \beta \sinh(\chi_m \beta) + D_m \beta \cosh(\chi_m \beta)\}_i = 0. \tag{4.15}$$

Continuity for velocity at two sides of the interface,

$$\begin{aligned}
&\{\frac{\mathrm{J}_2(\chi_m)^2}{2} \begin{pmatrix} \chi_m \cosh(\chi_m \beta_m) \\ \sinh(\chi_m \beta_m) + \chi_m \beta_m \cosh(\chi_m \beta_m) \\ \cosh(\chi_m \beta_m) + \chi_m \beta_m \sinh(\chi_m \beta_m) \end{pmatrix} \cdot \begin{pmatrix} A_m \\ C_m \\ D_m \end{pmatrix} \\
&\qquad + \sum_{l=1}^{\infty} \omega_l (-1)^l \begin{pmatrix} \int_0^1 \hat{r} \mathrm{J}_1(\chi_m \hat{r}) \mathrm{I}_1(\omega_l \hat{r}) \mathrm{d}\hat{r} \\ \int_0^1 \hat{r}^2 \mathrm{J}_1(\chi_m \hat{r}) \mathrm{I}_2(\omega_l \hat{r}) \mathrm{d}\hat{r} \end{pmatrix} \cdot \begin{pmatrix} E_l \\ F_l \end{pmatrix}\}_i \\
&= \{\frac{\mathrm{J}_2(\chi_m)^2}{2} \begin{pmatrix} \chi_m \\ 0 \\ 1 \end{pmatrix} \cdot \begin{pmatrix} A_m \\ C_m \\ D_m \end{pmatrix} + \sum_{l=1}^{\infty} \omega_l \begin{pmatrix} \int_0^1 \hat{r} \mathrm{J}_1(\chi_m \hat{r}) \mathrm{I}_1(\omega_l \hat{r}) \mathrm{d}\hat{r} \\ \int_0^1 \hat{r}^2 \mathrm{J}_1(\chi_m \hat{r}) \mathrm{I}_2(\omega_l \hat{r}) \mathrm{d}\hat{r} \end{pmatrix} \cdot \begin{pmatrix} E_l \\ F_l \end{pmatrix}\}_j.
\end{aligned} \tag{4.16}$$

The non-slip boundary on the wall

$$\{\frac{\beta \omega_l}{2} \begin{pmatrix} \mathrm{I}_0(\omega_l) \\ \mathrm{I}_1(\omega_l) \end{pmatrix} \cdot \begin{pmatrix} E_l \\ F_l \end{pmatrix} + \sum_{m=1}^{\infty} \chi_m \mathrm{J}_0(\chi_m) \begin{pmatrix} \int_0^\beta \sinh(\chi_m \hat{z}) \sin(\omega_l \hat{z}) \mathrm{d}\hat{z} \\ \int_0^\beta \hat{z} \sinh(\chi_m \hat{z}) \sin(\omega_l \hat{z}) \mathrm{d}\hat{z} \\ \int_0^\beta \hat{z} \cosh(\chi_m \hat{z}) \sin(\omega_l \hat{z}) \mathrm{d}\hat{z} \end{pmatrix} \cdot \begin{pmatrix} A_m \\ C_m \\ D_m \end{pmatrix}\}_i$$

$$= \{-\frac{1-(-1)^l}{\omega_l}\}_i \quad (4.17)$$

Continuity for viscous force at two sides of the interface,

$$\frac{\mu_i}{\mu_j}\{\begin{pmatrix} \chi_m^2 \sinh(\chi_m\beta) \\ 2\chi_m \cosh(\chi_m\beta) + \beta\chi_m^2 \sinh(\chi_m\beta) \\ 2\chi_m \sinh(\chi_m\beta) + \beta\chi_m^2 \cosh(\chi_m\beta) \end{pmatrix} \cdot \begin{pmatrix} A_m \\ C_m \\ D_m \end{pmatrix}\}_i = \{2\chi_m C_m\}_j. \quad (4.18)$$

By truncating both series, the infinity large system formed by eqs. (4.14) to (4.18) can be truncated into a system of $(N \times 5 \times 2) \times (N \times 5 \times 2)$, where N is the maximum order of the truncated series, and all $(N \times 5 \times 2)$ coefficients can be obtained by solving this linear system. To reduce the rank of the matrix, it is recommended to reorganize the equations starting from eqs. (4.14), (4.15) and (4.18), where the coefficients for one series are not tangled with these from the other one. Choose an independent variable from each series at an order, thus all the other 3 coefficients at this order can be expressed by them. Then, substitute into eqs. (4.16) and (4.18), and the system is reduced into $(N \times 2 \times 2) \times (N \times 2 \times 2)$. In the practice of this thesis, C_m, F_l are chosen as the two sets of independent variables, and then calculations for other three sets of coefficients are conducted after solving the system. This can save a considerate amount of calculation time.

After bounding the coefficients in eq. (4.12), the flow field as well as the skin friction coefficients for each plug can be calculated. Refer to chapter 2 for the procedures since they are basically identical.

$$\hat{u}_z = \sum_{l=1}^{\infty} \omega_l \sin(\omega_l \hat{z})[E_l \mathrm{I}_0(\omega_l \hat{r}) + F_l \hat{r} \mathrm{I}_1(\omega_l \hat{r})] \\ + \sum_{m=1}^{\infty} \chi_m \mathrm{J}_0(\chi_m \hat{r})[A_m \sinh(\chi_m \hat{z}) + C_m \hat{z} \sinh(\chi_m \hat{z}) + D_m \hat{z} \cosh(\chi_m \hat{z})], \quad (4.19)$$

$$\hat{u}_r = -\sum_{l=1}^{\infty} \omega_l \cos(\omega_l \hat{z})[E_l \mathrm{I}_1(\omega_l \hat{r}) + F_l \hat{r} \mathrm{I}_2(\omega_l \hat{r})]$$

$$- \sum_{m=1}^{\infty} \mathrm{J}_1(\chi_m \hat{r})\{[A_m \chi_m + C_m \chi_m \hat{z} + D_m] \cosh(\chi_m \hat{z}) + [C_m + D_m \chi_m \hat{z}] \sinh(\chi_m \hat{z})\}, \quad (4.20)$$

$$C_f = \frac{4}{\beta} \sum_{l=1}^{\infty} \omega_l [1 - (-1)^l][E_l \mathrm{I}_1(\omega_l) + F_l \mathrm{I}_0(\omega_l)]. \quad (4.21)$$

The sensitivity study is also carried out here. The objective is the averaged skin friction coefficient (eq. (4.23)). It is shown in fig. 4.3 that the averaged skin friction coefficient is stable after series number is larger than 61. Thus, 61 is chosen as the maximum series number.

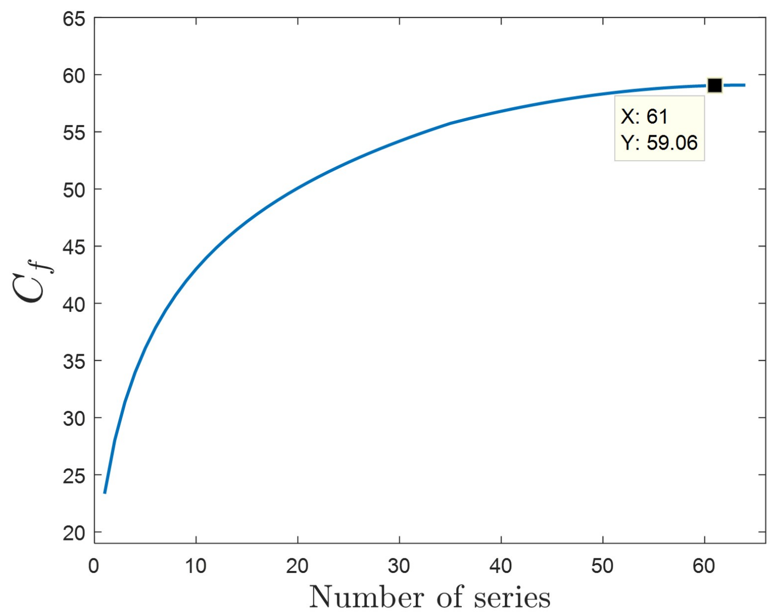

Figure 4.3: The sensitivity study for the analytical solution. Variation of averaged C_f with the growing series number. $\beta_1 = 1,\ \beta_2 = 1,\ \mu_2/\mu_1 = 16$.

4.2 Results and discussions

4.2.1 Validate using previous numerical study [1]

To validate the analytical solution, a case from [1] is chosen for comparison. The working liquid for plug 1 is n-butyl acetate ($l_1 = 3.0$ mm$, \mu_1 = 7.370 \times 10^{-4}$ Pa $\cdot$ s) while that for plug 2 is water ($l_2 = 2.4\,\mathrm{mm}, \mu_2 = 8.090 \times 10^{-4}\,\mathrm{Pa \cdot s}$). The inner diameter for the channel is 1.0 mm ($r = 0.5$ mm). Thus, the dimensionless parameters here is $\beta_1 = 6.0$, $\beta_2 = 4.8, \mu_2/\mu_1 = 1.2076$. The comparison between the results from [1] and from the analytical solution is plotted in the fig. 4.4. As it shows, no obvious difference can be seen in two subplots, most of the main characters such as well defined internal circulation and the turn around of streamlines near the ends of plugs are well captured by our analytical solution. Thus, it can be treated as an validation.

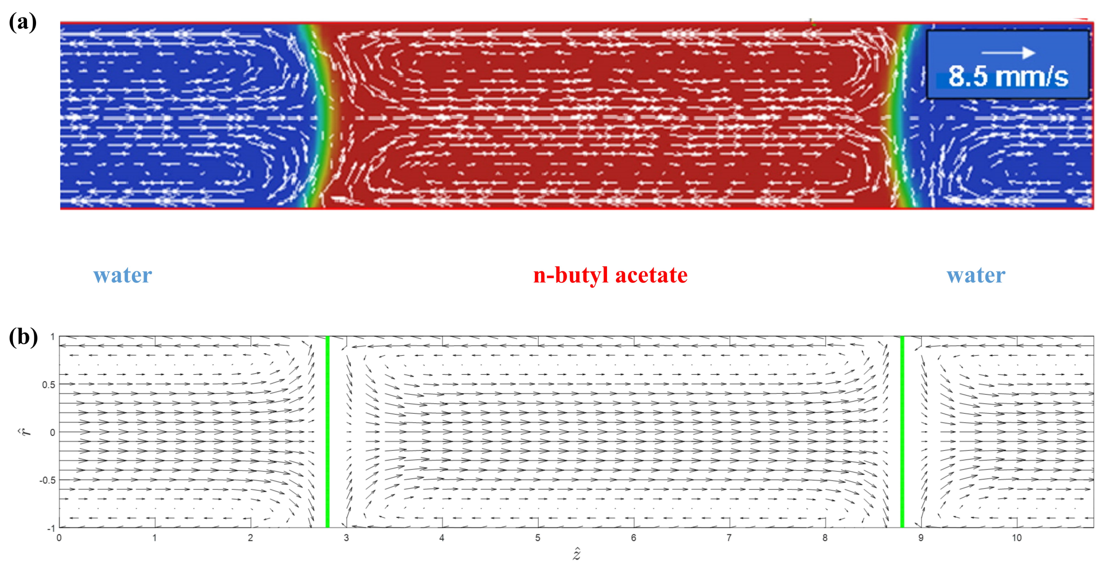

Figure 4.4: Comparison between plots of flow field (a) from simulation in [1] (re-printed with permission) and (b) from the analytical solution in this work. $\beta_1 = 6.0$, $\beta_2 = 4.8, \mu_2/\mu_1 = 1.2076$.

4.2.2 Validate using the existing gas-liquid model [2]

The gas-liquid plug flow model is a simplification of the liquid-liquid model, where the viscosity is neglected in the gas phase. Hence, two models should converge when $\mu2/\mu1$ is large enough and phase 1 becomes the gas phase in the liquid-liquid model.

The gas-liquid plug flow can either be obtained by setting the inner-outer radius ratio infinity close to 1 ($\eta \to 1$) in chapter 2 (though some numerical error will occur owing to the large value of Bessel function K near the inner wall). Thus, it is preferred to obtain the results from the previous work of Che, Wong, Neng and Nguyen [2] directly. The case for validate is $\beta = 2$ for the gas-liquid model and $\beta_1 = 1$, $\beta_2 = 2$, $\mu 2/\mu 1 = 64$ for the liquid-liquid model. The viscosity ratio $\mu 2/\mu 1 = 64$ is chosen because throughout my work, I find lots of variations with increasing viscosity ratio becomes stable when $\mu 2/\mu 1 > 64$ (These variations will be discussed in the next a few subsections).

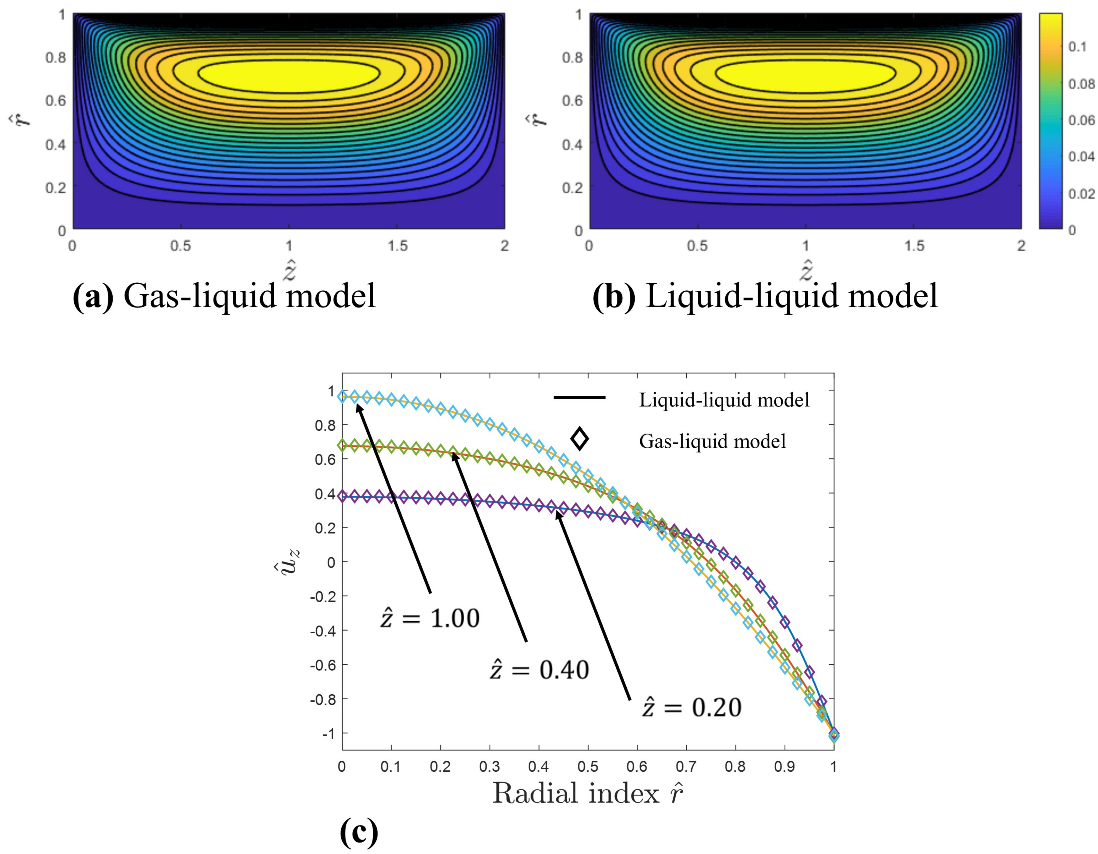

Figure 4.5: Comparison between contours of stream function (a) from the analytical solution of the gas-liquid model in [2] (here only the equations in this citation are used to plot the contour) and (b) from the analytical solution of liquid-liquid model in this work. (c) The distribution of axial velocity $\hat{u}_z$ on 3 sample lines $\hat{z} = 1.00,\ 0.40,\ 0.20$. $\beta_1 = 1, \beta_2 = 2, \mu_2/\mu_1 = 64$ ($\beta_1, \mu_2/\mu_1$ are not needed for (a)).

The comparison between two results is plotted in fig. 4.5. No obvious difference can be seen from two contour plots. The axial velocity distribution is also nearly identical. Thus, this can be treated as a validation under the condition when the viscosity ratio μ_2/μ_1 is far from 1.

4.2.3 Influence of viscosity ratio μ_2/μ_1

As mentioned in [57, 59], the gradient of $\hat{u}_r$ near the interface is the key for momentum transfer as well as for generating cap vortexes. When μ_2/μ_1 is larger than 1, the gradient of $\hat{u}_r$ is different at two sides of the interface owing to the continuity of shear force. The plug 1 with smaller viscosity will have larger $\partial\hat{u}_r/\partial\hat{z}$, this might lead to the transverse velocity near the interface because of the continuity of velocity, and in another word, might lead to secondary vortex near this interface. A demonstration is shown in fig. 4.6.

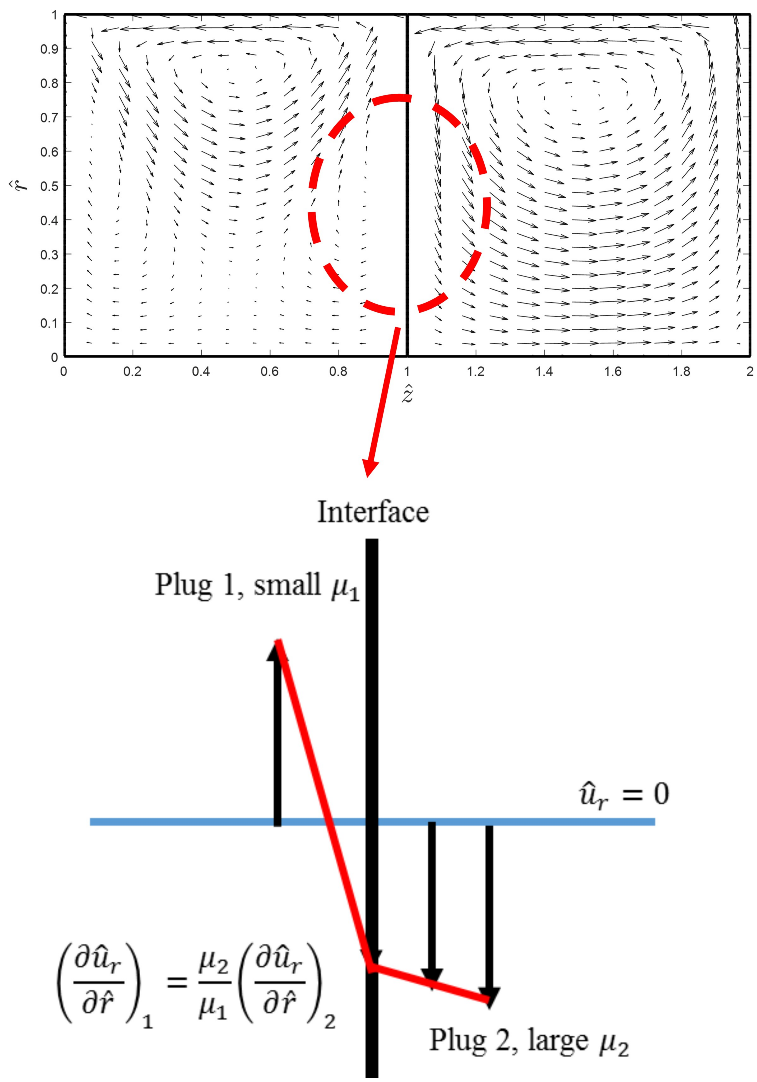

Figure 4.6: Schematic show of the reason for cap vortexes when μ_2/μ_1 is sufficiently large.

The most natural way of strengthening or weakening the shear force is to vary the viscosity ratio of two plugs μ_2/μ_1. In fig. 4.7, the influence of viscosity ratio μ_2/μ_1 of two plugs upon the flow pattern as well as secondary vortexes are presented, where the lengths of two plugs are mounted at $\beta_1 = 1$, $\beta_2 = 1$. In fig. 4.7 (a) when μ_2/μ_1 is 1, an well defined vortex (main vortexes) can be seen in each plug with a shape of bullet head (head is towards the center of channel $\hat{r} = 0$). The 'cache' zone can be seen near the interface of two fluids, where the velocity gradually becomes nearly zero in both plugs. In fig. 4.7 (b) when μ_2/μ_1 is 2, the shape of the main vortex in the plug 1 becomes like triangle with curved head and the 'cache' zone takes more space. The main vortex of plug 2 however expands, the head (at $\hat{r} = 0$) of the curved triangle becomes wider. The cap vortexes, which develop inside the 'cache' zone and firstly appear when μ_2/μ_1 approaches 4 as in fig. 4.7 (c), gradually become stronger when μ_2/μ_1 increases to 16 and squeeze the space of original main vortex as in fig. 4.7 (d).

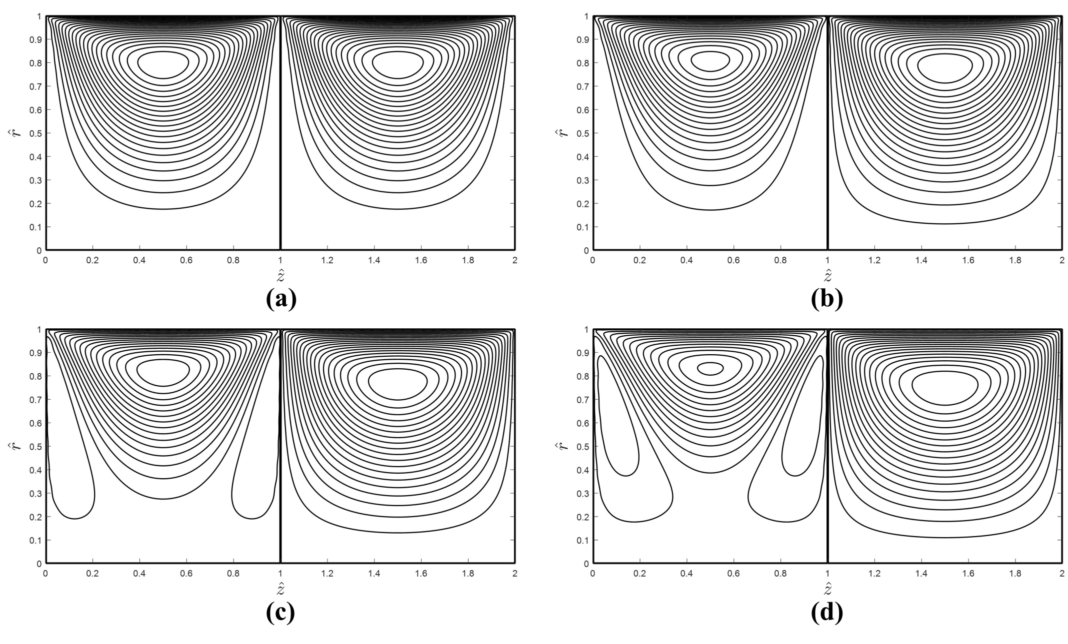

Figure 4.7: Sequence of stream lines with increasing $\mu_2/\mu_1 = (1, 2, 4, 16)$, where $\beta_1 = \beta_2 = 1$.

In fig. 4.8 (b), the intensity of secondary vortex center $\hat{\psi}_{min}$ is plotted against varying μ_2/μ_1. Since the negative symbol here means the rotation of the vortex, thus the decreasing of $\hat{\psi}_{min}$ in fig. 4.8 (b) yields the strengthening cap vortexes however in the inversed rotation as that of the main vortex. The decreasing trend of $\hat{\psi}_{min}$ is obvious when μ_2/μ_1 firstly increases because of stronger momentum transfer by shear force at the interface, and then it becomes stable when $\hat{\psi}_{min}$ reaches 64, where the plug 1 can be treated as a gas plug.

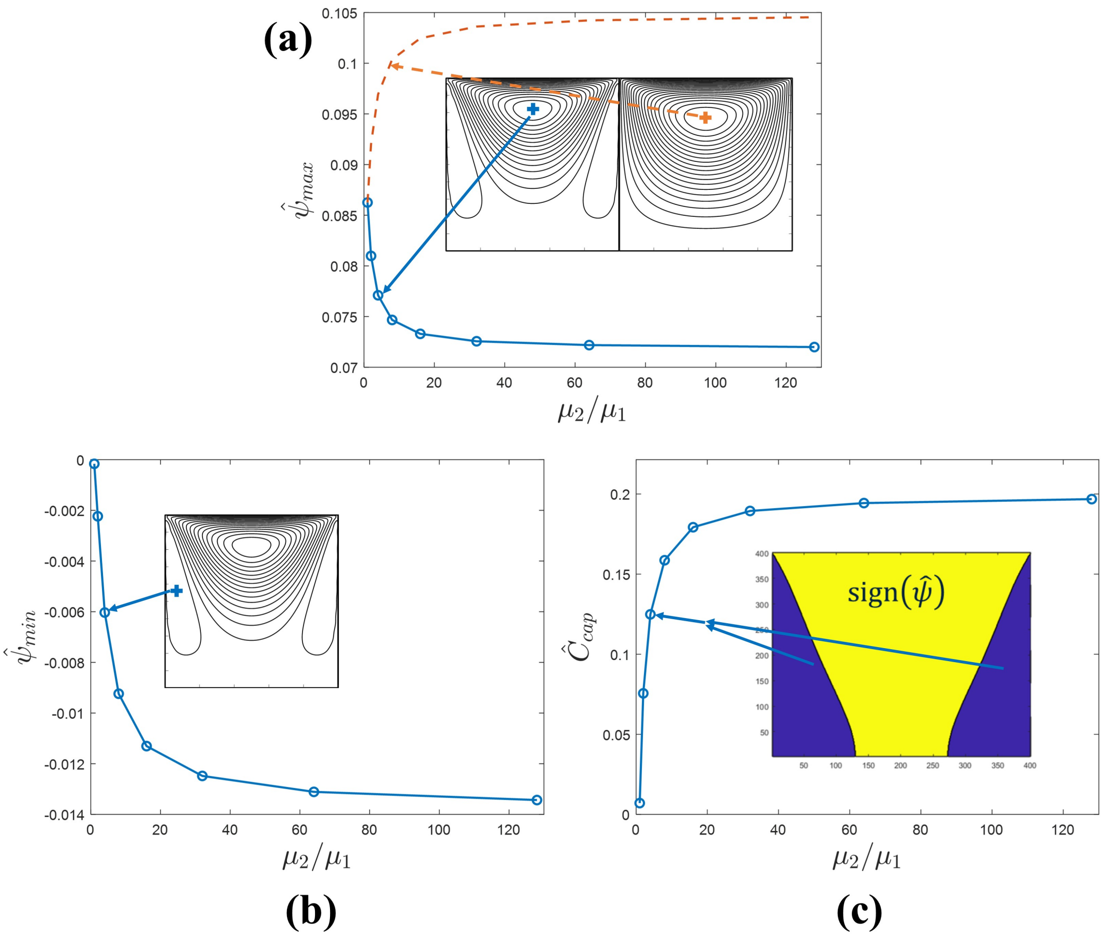

Figure 4.8: The influence of increasing μ_2/μ_1 upon (a) $\hat{\psi}_{max}$ the intensity of main vortex centers , (b) $\hat{\psi}_{min}$ the intensity of cap vortex centers in plug 1 and (c) $\hat{C}_{cap}$ the capacity (volume) of the cap vortex in plug 1.

Similarly, in fig. 4.8 (c) an increasing trend of the volume taken up by the cap vortexes $\hat{C}_{cap}$ (defined below) can be firstly observed, then it becomes stable when μ_2/μ_1 becomes larger than 64. The variation of the intensity of main vortexes $\hat{\psi}_{max}$ then can be easily understood as in fig. 4.8 (a). When μ_2/μ_1 increases, the 'cache' zone in plug 1 gradually develops and becomes cap vortexes which completes with its main vortex, thus $\hat{\psi}_{max}$ decreases until μ_2/μ_1 becomes 64. The inversed process and trending happen in plug 2 naturally.

$$\hat{C}_{cap} = \int_0^\beta \int_0^1 \frac{1-\mathrm{sgn}(\hat{\psi})}{2} \hat{r}\mathrm{d}\hat{r}\mathrm{d}\hat{z}. \tag{4.22}$$

4.2.4 Influence of plug lengths β_1, β_2

As discussed in chapter 2 the circulation inside the gas-liquid plug flow can be highly affected by the lengths or say aspect ratios of plugs. Thus, the influences of the length of plug 1 and plug 2 are investigated, respectively.

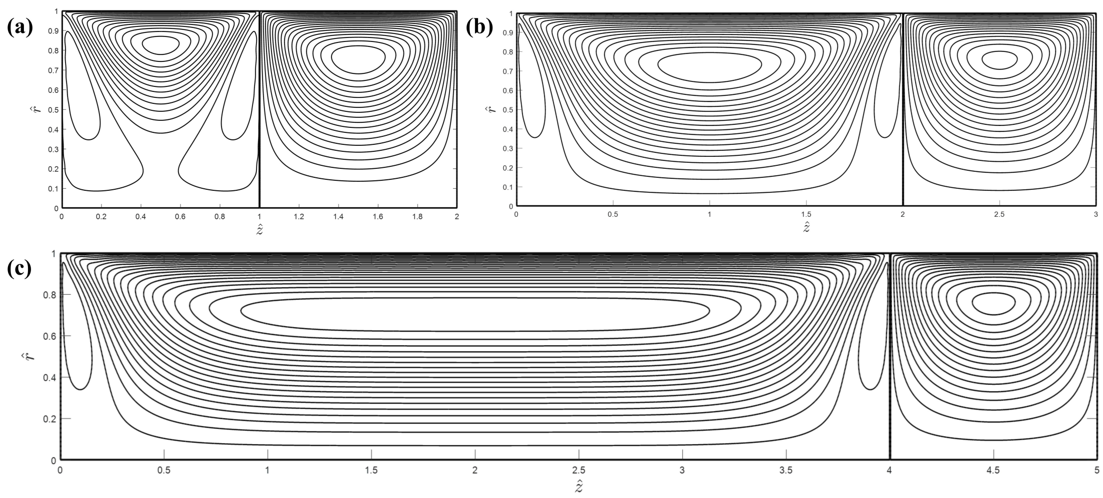

Figure 4.9: Sequence of stream lines with increasing β_1 = (1, 2, 4), where $\beta_2 = 1$ and $\mu_2/\mu_1 = 16$.

The sequence of streamlines of varying β_1 is plotted inside fig. 4.9, where $\beta_2 = 1$ and $\mu_2/\mu_1 = 16$. Two obvious findings are listed: 1. The cap vortexes shrink slightly in size and, thus 2. the shape of the main vortex in plug 1 varies from a triangle to a like trapezoid. However, no visible change can be observed in plug 2.

The detailed influences of β_1 are then plotted in fig. 4.10. From fig. 4.10 (a) it can be seen that the influence of β_1 upon the main vortex in plug 1 is like that in gas-liquid plug flow. $\hat{\psi}_{max}$ in plug 1 firstly increases, reaches the 1-d asymptotic limit and then becomes stable when β_1 increases. The influence upon $\hat{\psi}_{max}$ in plug 2 is not visible, which suit well to the observation made earlier in fig. 4.9. In fig. 4.10 (b) and (c) it can be seen that cap vortexes $\hat{\psi}_{min}$ become slightly weaker while its capacity $\hat{C}_{cap}$ firstly decreases when β_1

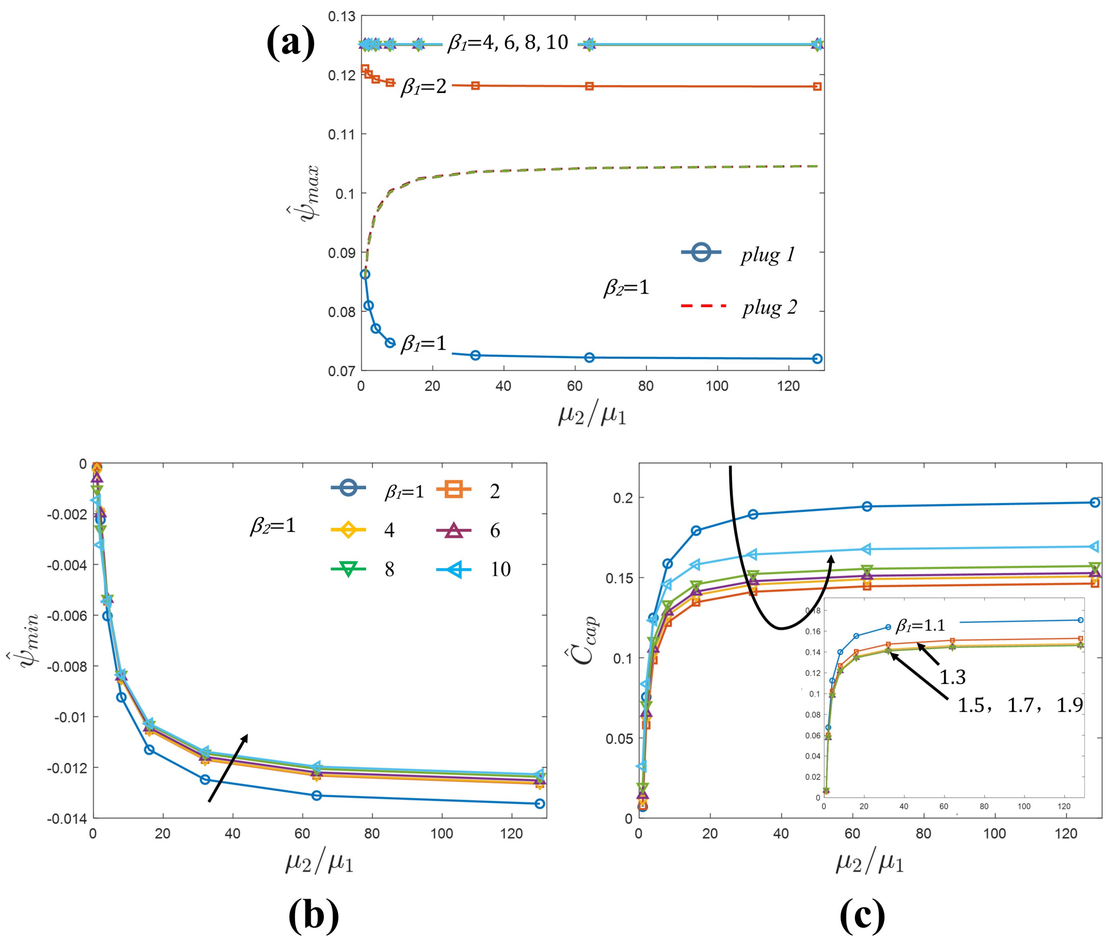

Figure 4.10: The influence of varying β_1 upon (a) $\hat{\psi}_{max}$ the intensity of main vortex centers , (b) $\hat{\psi}_{min}$ the intensity of cap vortex centers in plug 1 and (c) $\hat{C}_{cap}$ the capacity (volume) of the cap vortex in plug 1.

increases from 1 to 2, then increases again when β_1 increases from 2 to 10.

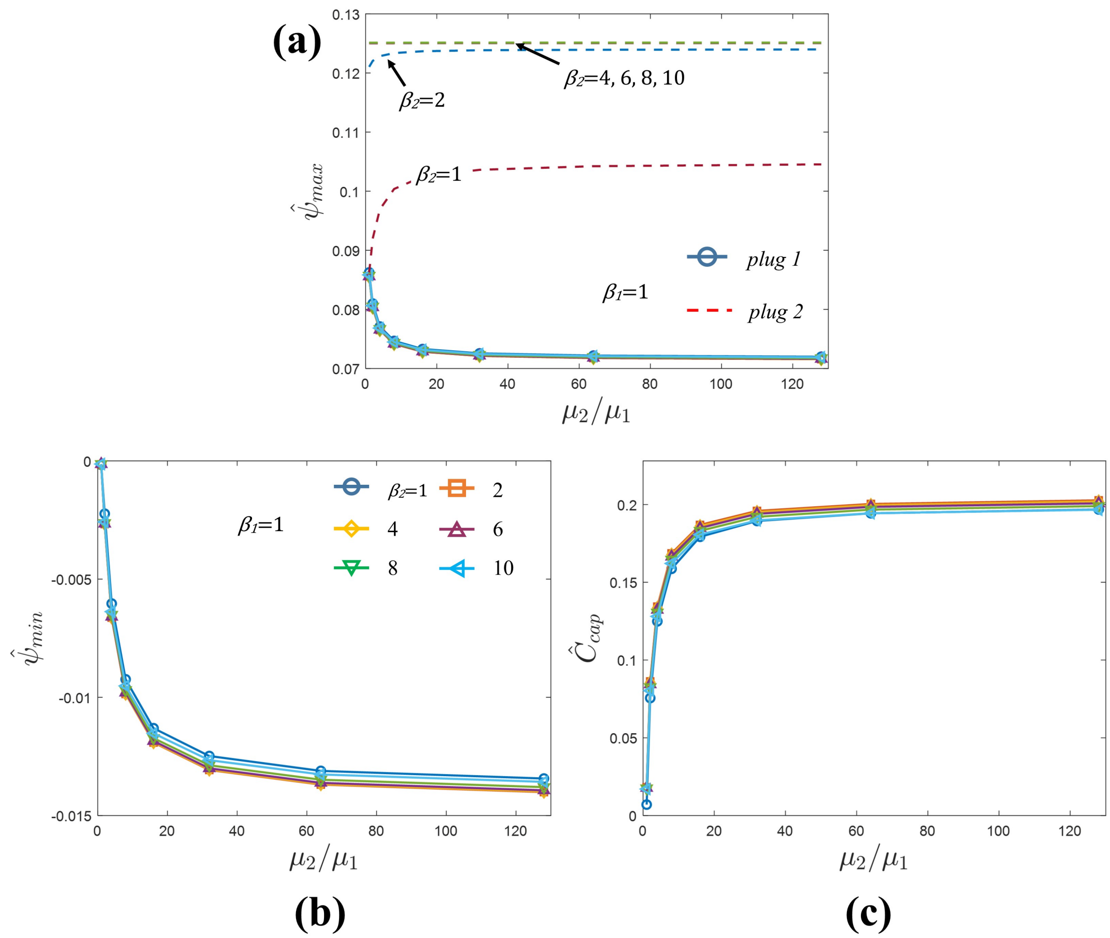

Figure 4.11: The influence of varying β_2 upon (a) $\hat{\psi}_{max}$ the intensity of main vortex centers , (b) $\hat{\psi}_{min}$ the intensity of cap vortex centers in plug 1 and (c) $\hat{C}_{cap}$ the capacity (volume) of the cap vortex in plug 1.

Similarly, the influences of varying β_2 are plotted out in fig. 4.10. However, no obvious influence of any is observed besides that upon the main vortex in plug 2 itself.

4.2.5 Skin friction coefficients C_f

The skin friction coefficients for two plugs can be quoted from eq. (4.21), respectively. The total pressure loss can be calculated by repeating the calculation for that introduced by each plug using their skin friction coefficients. However, an overall coefficient to evaluate the pumping power without calculating for multiple times is preferred. It is easily found out from the definition of skin friction coefficient that,

$$\Delta P \propto \mu\beta.$$

And since the total pressure loss is

$$\Delta P = \Delta P_1 + \Delta P_2.$$

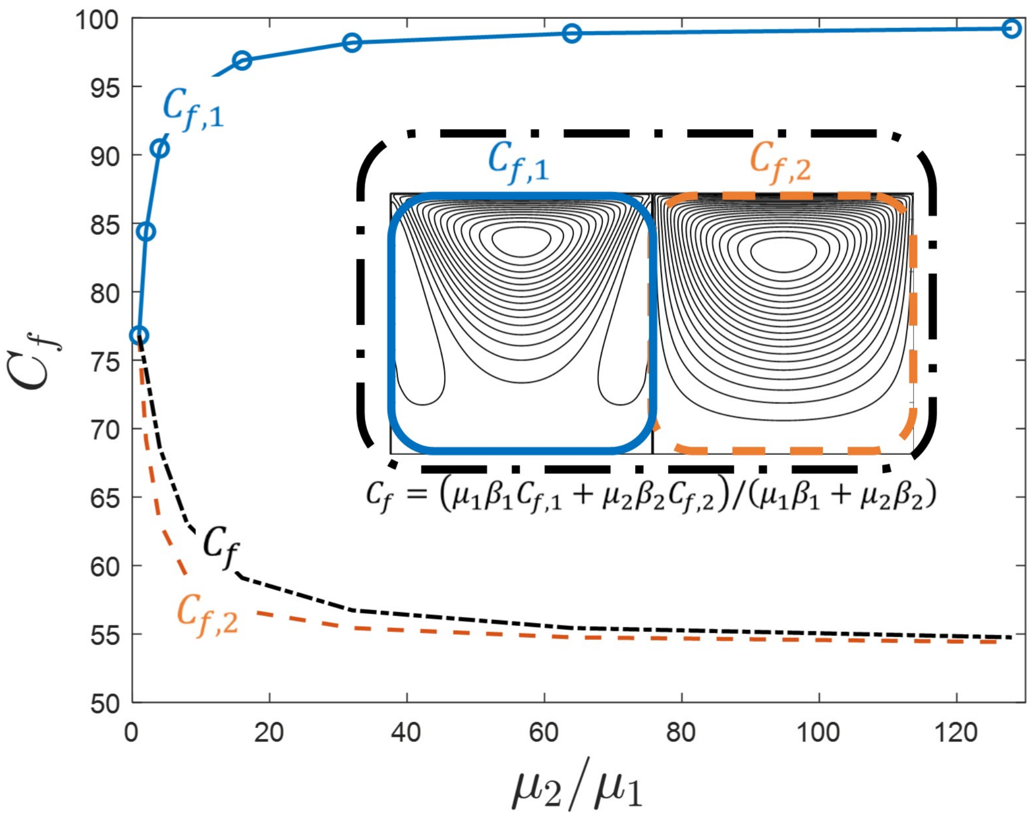

Figure 4.12: The skin friction coefficients for plug 1, plug 2 and their mean value with varying μ_2/μ_1, $\beta_1 = \beta_2 = 1$.

Thus, the definition of the overall friction coefficient is as below. In fig. 4.12, the friction coefficients for plug 1, plug 2 and their mean value are presented, where the plug lengths are mounted at $\beta_1 = \beta_2 = 1$. Identical value is obtained when $\mu_1 = \mu_2$ naturally. When μ_2/μ_1

increases from 1 to 128, $C_{f,1}$ increases from 76.81 to 99.22, while $C_{f,2}$ decreases from 76.81 to 54.41. The mean value for a two-plug period C_f is closer to the variation of $C_{f,2}$, which decreases from 76.81 to 54.76. The value of C_f at extremely high μ_2/μ_1 is very close to that of gas-liquid flow in [2], since here the flow field for plug 2 is already close to gas-liquid flow field with the same length β_2.

$$C_f = \frac{\mu_1\beta_1 C_{f,1} + \mu_2\beta_2 C_{f,2}}{\mu_1\beta_1 + \mu_2\beta_2}. \tag{4.23}$$

The detailed influences of plug lengths β_1 and β_2 are presented in fig. 4.13. In fig. 4.13 (a) It can be concluded that: 1. The mean skin friction coefficient C_f is a decreasing function of β_1. 2. The influence of β_1 is more obvious when the viscosity of two plugs are still comparable (μ_2/μ_1 is small). When μ_2/μ_1 is large, as have seen in fig. 4.12 the mean C_f can be close to $C_{f,2}$, and the influence caused by plug 1 is limited. 3. C_f is a decreasing function of μ_2/μ_1 when β_1 is small, while it becomes an increasing function of μ_2/μ_1 when $\beta_1 > 2$. The influence of β_2 is simple as in fig. 4.13 (b) that C_f is a decreasing function of both β_2 and μ_2/μ_1.

4.3 Summary of this chapter

The interaction between the interface of liquid-liquid plug flow caused by shear force can complicate the flow field. Secondary vortexes near the caps of the fluid with significantly smaller viscosity will be generated. In this chapter, 2 PDEs was setup simultaneously to model the liquid-liquid plug flow in microchannels with round cross-section. Detailed study of the relationship between main and cap vortexes was carried out, the influence of plug lengths and viscosity ratio upon flow pattern and skin friction coefficient were discussed. Findings are summarized as below:

- The cap vortexes would gradually appear when μ_2/μ_1 increases. It is formed owing to the velocity continuity on the interface, as well as the high gradient of velocity in the plug 1 with small viscosity caused by the continuity of shear force. The cap vortexes become stronger as μ_2/μ_1 increases, the capacity (volume) of which also expands simultaneously.

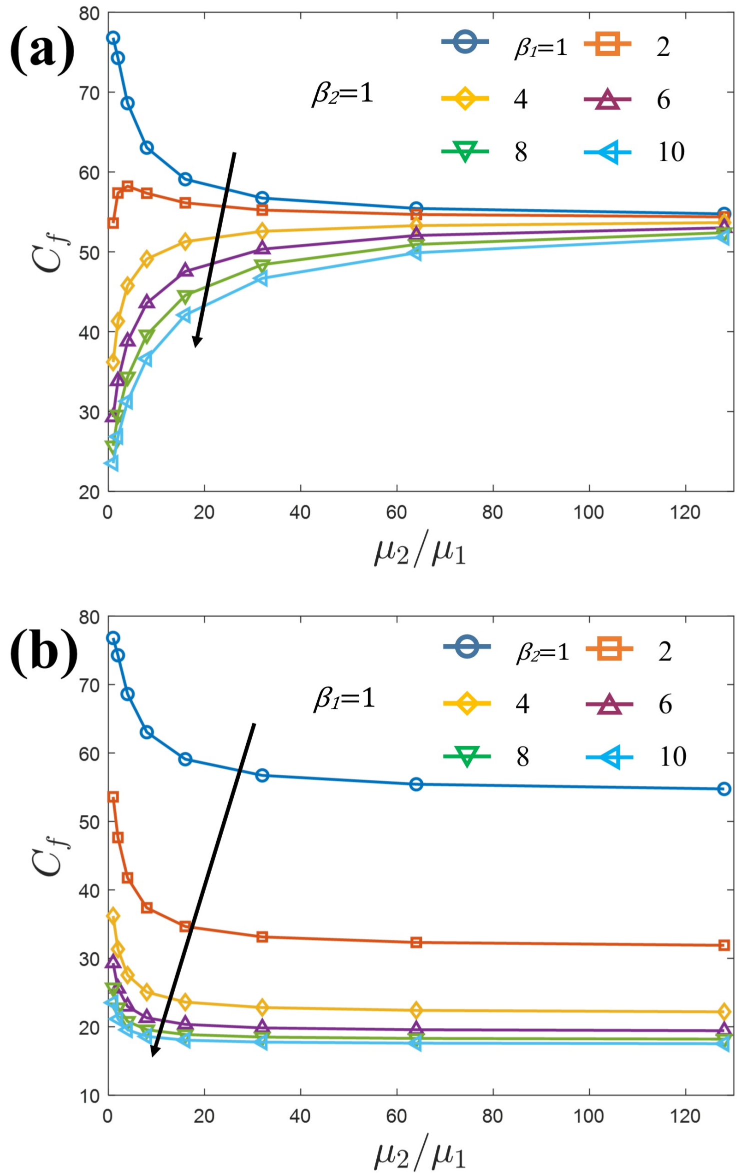

Figure 4.13: Variations of mean skin friction C_f coefficients with increasing μ_2/μ_1, $\beta_1 = \beta_2 = 1$ under (a)$\beta_2 = 1, \beta_1 = 1 \sim 10$, (b)$\beta_1 = 1, \beta_2 = 1 \sim 10$

- The intensity of main vortexes in two plugs show inversed trends to each other with increasing μ_2/μ_1. $\hat{\psi}_{max}$ in plug 1 drops since it competes with the cap vortexes inside, while that in plug 2 grows with increasing μ_2/μ_1 naturally.

- The lengths of plugs will mainly influence their main vortex. The length of the plug with small viscosity β_1 has an impact upon the cap vortexes in itself, while the length of another plug β_2 barely has an impact upon the cap vortexes.

- The skin friction coefficient C_f is a decreasing function of all β_1, β_2 and μ_2/μ_1 but for one case, where β_1 is large and where C_f becomes an increasing function of μ_2/μ_1.

- All of the trends mentioned here become stable when μ_2/μ_1 becomes large sufficiently and converges to that under the gas-liquid plug flow scenario with the same lengths, which is owing to infinitely small velocity gradient near the ends in plug 2, and hence its flow field is infinitely close to that in gas-liquid plug flow.

Chapter 5

Conclusions, limitations and potential future work

Plug flow creates well defined and stable vortexes, which are owing to the circulating fluid inside caused by interfaces between two immiscible fluids. It is very efficient in heat transfer enhancement comparing to single-phase flow. Meanwhile, it is also much easier to control compared to flow with phase change. Inside microchannel, the dominance of viscous force makes the momentum equation linear and solvable (the Stokes assumption), which can help save a considerable amount of time for the design work with a massive number of cases to search within.

In this thesis, I concentrated on finding analytical solutions to plug flow in microchannels with different geometry and find out two unrevealed series solutions in the end: 1. gas-liquid plug flow in the concentric microchannel and 2. liquid-liquid plug flow in the circular microchannel. Then I systematically investigated the influences of multiple inputs upon both flow pattern and skin friction coefficient in details.

An application of the gas-liquid plug flow field in the concentric tube, the heat transfer at three kinds of typical boundary conditions were simulated and investigated in detail. Enhancements by the plug flow heat transfer to single-phase flow heat transfer were revealed for all types of boundary types. Three simplified thermal networks of heat transfer at each boundary type were extracted and used to explain heat transfer performance under different working conditions. At the end of this numerical study, a simplified model used for the fully developed thermal field was extracted with the help of the control volume method. Around 12,000 cases were simulated in an acceptable amount of time, whose Nusselt numbers were stored for direct quoting to help the design work in the future.

However, there still stand some limitations of this work due to the limited time and facilities. I will talk about these limitations and give some suggestions to enhance the results of this thesis and to create new findings in the future.

First of all, though some validation and verification from either asymptotic cases or previous researches have been carried out, no experiment in the author's lab has been conducted relevant to this topic. As have illustrated in the introduction, there stand challenges to both advanced non-intrusive, micro-scale temperature measuring facilities and perfectly matched materials to avoid failure caused by optical refraction. Unfortunately, there were limited experienced hands relative to either at the beginning stage of this study, which led to the hard decision on not doing experiments. However, if one can accurately and quantitatively capture the plug flow field in complicated, non-straight microchannels, merely their methodology will be a significant contribution.

Secondly, by the very end of finishing this work, my supervisor and I found a correlation which can directly calculate the maximum/minimum stream functions. The correlation is not redundant to the analytical solution since it saves the time of calculating and searching the whole field and only focuses on the key of enhancing mixing or heat transfer. Under numerous working conditions, it was also found out the maximum/minimum stream functions (in fig. A.4) has a similar trend as the heat transfer enhancement at IFB and OFB (in fig. 3.8). Though the very dense database and quick simulation based upon simplified model is already great for engineering design need, this can still be a chance to reveal a quantitative connection between the plug flow field and thermal performance. Unfortunately owing to limited time (see details in appendix A), the correlation is only developed for the flow field. To build the connection between circulation flux and the heat transfer enhancement can be a focus in the future.

Lastly, the limitation of the analytical model has been mentioned earlier in chapter 2. The influence of surface tension cannot be included in the analytical modeling. However, I have come up with an idea (thanks to Dr. Brinkerhoff's hint) of treating the liquid film as a liquid-liquid interface, when the plug is not deformed too much. The boundary conditions here may not be interpreted as the non-slip moving wall anymore, however can still be described using a known distribution when the information about the liquid film is given such as the film thickness (which can set the calculation domain) and the slippery velocity compared to the wall (which can help to determine the first order and second order boundary conditions). Then by applying similar fashion in chapter 4 the analytical solution can still be obtained. The modification to heat transfer model can be even more straightforward since the flow is in laminar region, the heat transfer in the liquid film can be seen as a Greatz problem or even as pure conduction if the slippery is not strong. Overall, to include the liquid film in the current analytical modeling can be a potential point for the future work.

Bibliography

[1] A. Ghaini, A. Mescher, and D. W. Agar, "Hydrodynamic studies of liquid–liquid slug flows in circular microchannels," *Chemical engineering science*, vol. 66, no. 6, pp. 1168–1178, 2011.

[2] Z. Che, T. N. Wong, and N.-T. Nguyen, "An analytical model for plug flow in microcapillaries with circular cross section," *International Journal of Heat and Fluid Flow*, vol. 32, no. 5, pp. 1005–1013, 2011.

[3] ——, "Heat transfer enhancement by recirculating flow within liquid plugs in microchannels," *International Journal of Heat and Mass Transfer*, vol. 55, no. 7-8, pp. 1947–1956, 2012.

[4] V. Meleshko, "Steady stokes flow in a rectangular cavity," *Proc. R. Soc. Lond. A*, vol. 452, no. 1952, pp. 1999–2022, 1996.

[5] H. A. Stone, A. D. Stroock, and A. Ajdari, "Engineering flows in small devices: microfluidics toward a lab-on-a-chip," *Annu. Rev. Fluid Mech.*, vol. 36, pp. 381–411, 2004.

[6] S. Lansing, J. Víquez, H. Martínez, R. Botero, and J. Martin, "Quantifying electricity generation and waste transformations in a low-cost, plug-flow anaerobic digestion system," *ecological engineering*, vol. 34, no. 4, pp. 332–348, 2008.

[7] M. T. Kreutzer, F. Kapteijn, J. A. Moulijn, and J. J. Heiszwolf, "Multiphase monolith reactors: chemical reaction engineering of segmented flow in microchannels," *Chemical Engineering Science*, vol. 60, no. 22, pp. 5895–5916, 2005.

[8] S. Lansing, J. F. Martin, R. B. Botero, T. N. Da Silva, and E. D. Da Silva, "Methane

production in low-cost, unheated, plug-flow digesters treating swine manure and used cooking grease," *Bioresource technology*, vol. 101, no. 12, pp. 4362–4370, 2010.

[9] B. K. Yen, A. Günther, M. A. Schmidt, K. F. Jensen, and M. G. Bawendi, "A microfabricated gas–liquid segmented flow reactor for high-temperature synthesis: the case of cdse quantum dots," *Angewandte Chemie International Edition*, vol. 44, no. 34, pp. 5447–5451, 2005.

[10] R. Sista, Z. Hua, P. Thwar, A. Sudarsan, V. Srinivasan, A. Eckhardt, M. Pollack, and V. Pamula, "Development of a digital microfluidic platform for point of care testing," *Lab on a Chip*, vol. 8, no. 12, pp. 2091–2104, 2008.

[11] T. Dixit and I. Ghosh, "Review of micro-and mini-channel heat sinks and heat exchangers for single phase fluids," *Renewable and Sustainable Energy Reviews*, vol. 41, pp. 1298–1311, 2015.

[12] X. Gao and R. Li, "Effects of nozzle positioning on single-phase spray cooling," *International Journal of Heat and Mass Transfer*, vol. 115, pp. 1247–1257, 2017.

[13] J. Kim, "Spray cooling heat transfer: the state of the art," *International Journal of Heat and Fluid Flow*, vol. 28, no. 4, pp. 753–767, 2007.

[14] L. Lin and R. Ponnappan, "Heat transfer characteristics of spray cooling in a closed loop," *International Journal of Heat and Mass Transfer*, vol. 46, no. 20, pp. 3737–3746, 2003.

[15] K. Jambunathan, E. Lai, M. Moss, and B. Button, "A review of heat transfer data for single circular jet impingement," *International journal of heat and fluid flow*, vol. 13, no. 2, pp. 106–115, 1992.

[16] K. Daou, R. Wang, and Z. Xia, "Desiccant cooling air conditioning: a review," *Renewable and Sustainable Energy Reviews*, vol. 10, no. 2, pp. 55–77, 2006.

[17] S. Launay, V. Sartre, and J. Bonjour, "Parametric analysis of loop heat pipe operation: a literature review," *International Journal of Thermal Sciences*, vol. 46, no. 7, pp. 621–636, 2007.

[18] T. Bandara, N.-T. Nguyen, and G. Rosengarten, "Slug flow heat transfer without phase change in microchannels: A review," *Chemical Engineering Science*, vol. 126, pp. 283–295, 2015.

[19] M. Asadi, G. Xie, and B. Sunden, "A review of heat transfer and pressure drop characteristics of single and two-phase microchannels," *International Journal of Heat and Mass Transfer*, vol. 79, pp. 34–53, 2014.

[20] D. B. Tuckerman and R. F. W. Pease, "High-performance heat sinking for vlsi," *IEEE Electron device letters*, vol. 2, no. 5, pp. 126–129, 1981.

[21] A. Asthana, I. Zinovik, C. Weinmueller, and D. Poulikakos, "Significant heat transfer enhancement in microchannels with a segmented flow of two immiscible liquids," in *2010 14th International Heat Transfer Conference*. American Society of Mechanical Engineers, 2010, pp. 141–149.

[22] ——, "Significant nusselt number increase in microchannels with a segmented flow of two immiscible liquids: An experimental study," *International Journal of Heat and Mass Transfer*, vol. 54, no. 7-8, pp. 1456–1464, 2011.

[23] A. Bar-Cohen, M. Arik, and M. Ohadi, "Direct liquid cooling of high flux micro and nano electronic components," *Proceedings of the IEEE*, vol. 94, no. 8, pp. 1549–1570, 2006.

[24] M. Meis, F. Varas, A. Velázquez, and J. Vega, "Heat transfer enhancement in microchannels caused by vortex promoters," *International Journal of Heat and Mass Transfer*, vol. 53, no. 1-3, pp. 29–40, 2010.

[25] Y. Wang, F. Houshmand, D. Elcock, and Y. Peles, "Convective heat transfer and mixing enhancement in a microchannel with a pillar," *International Journal of Heat and Mass Transfer*, vol. 62, pp. 553–561, 2013.

[26] Y. Wang, A. Nayebzadeh, X. Yu, J.-H. Shin, and Y. Peles, "Local heat transfer in a microchannel with a pin fin—experimental issues and methods to mitigate," *International Journal of Heat and Mass Transfer*, vol. 106, pp. 1191–1204, 2017.

[27] W. Dean and J. Hurst, "Note on the motion of fluid in a curved pipe," *Mathematika*, vol. 6, no. 1, pp. 77–85, 1959.

[28] Y. Sui, C. Teo, P. S. Lee, Y. Chew, and C. Shu, "Fluid flow and heat transfer in wavy microchannels," *International Journal of Heat and Mass Transfer*, vol. 53, no. 13-14, pp. 2760–2772, 2010.

[29] G. Xia, J. Jiang, J. Wang, Y. Zhai, and D. Ma, "Effects of different geometric structures on fluid flow and heat transfer performance in microchannel heat sinks," *International Journal of Heat and Mass Transfer*, vol. 80, pp. 439–447, 2015.

[30] L. Chai, G. Xia, L. Wang, M. Zhou, and Z. Cui, "Heat transfer enhancement in microchannel heat sinks with periodic expansion–constriction cross-sections," *International Journal of Heat and Mass Transfer*, vol. 62, pp. 741–751, 2013.

[31] I. Mudawar and M. B. Bowers, "Ultra-high critical heat flux (chf) for subcooled water flow boiling—i: Chf data and parametric effects for small diameter tubes," *International Journal of Heat and Mass Transfer*, vol. 42, no. 8, pp. 1405–1428, 1999.

[32] D. Deng, W. Wan, Y. Qin, J. Zhang, and X. Chu, "Flow boiling enhancement of structured microchannels with micro pin fins," *International Journal of Heat and Mass Transfer*, vol. 105, pp. 338–349, 2017.

[33] S. Krishnamurthy and Y. Peles, "Flow boiling heat transfer on micro pin fins entrenched in a microchannel," *Journal of Heat Transfer*, vol. 132, no. 4, p. 041007, 2010.

[34] T. Y. Liu, P. Li, C. Liu, and C. Gau, "Boiling flow characteristics in microchannels with very hydrophobic surface to super-hydrophilic surface," *International Journal of Heat and Mass Transfer*, vol. 54, no. 1-3, pp. 126–134, 2011.

[35] C. Choi, J. S. Shin, D. I. Yu, and M. H. Kim, "Flow boiling behaviors in hydrophilic and hydrophobic microchannels," *Experimental Thermal and Fluid Science*, vol. 35, no. 5, pp. 816–824, 2011.

[36] A. Jaikumar and S. Kandlikar, "Pool boiling enhancement through bubble induced

convective liquid flow in feeder microchannels," *Applied Physics Letters*, vol. 108, no. 4, p. 041604, 2016.

[37] A. R. Betz and D. Attinger, "Can segmented flow enhance heat transfer in microchannel heat sinks?" *International Journal of Heat and Mass Transfer*, vol. 53, no. 19-20, pp. 3683–3691, 2010.

[38] J. Sivasamy, Z. Che, T. N. Wong, N.-T. Nguyen, and L. Yobas, "A simple method for evaluating and predicting chaotic advection in microfluidic slugs," *Chemical engineering science*, vol. 65, no. 19, pp. 5382–5391, 2010.

[39] P. Angeli and A. Gavriilidis, "Hydrodynamics of taylor flow in small channels: a review," *Proceedings of the Institution of Mechanical Engineers, Part C: Journal of Mechanical Engineering Science*, vol. 222, no. 5, pp. 737–751, 2008.

[40] Y. Lim, S. Yu, and N. Nguyen, "Flow visualization and heat transfer characteristics of gas–liquid two-phase flow in microtube under constant heat flux at wall," *International Journal of Heat and Mass Transfer*, vol. 56, no. 1-2, pp. 350–359, 2013.

[41] P. A. Walsh, E. J. Walsh, and Y. S. Muzychka, "Heat transfer model for gas–liquid slug flows under constant flux," *International Journal of Heat and Mass Transfer*, vol. 53, no. 15-16, pp. 3193–3201, 2010.

[42] Z. Che, T. N. Wong, and N.-T. Nguyen, "Heat transfer in plug flow in cylindrical microcapillaries with constant surface heat flux," *International Journal of Thermal Sciences*, vol. 64, pp. 204–212, 2013.

[43] S. T. Wereley and C. D. Meinhart, "Recent advances in micro-particle image velocimetry," *Annual Review of Fluid Mechanics*, vol. 42, pp. 557–576, 2010.

[44] D. Sinton, "Microscale flow visualization," *Microfluidics and Nanofluidics*, vol. 1, no. 1, pp. 2–21, 2004.

[45] D. Ross, M. Gaitan, and L. E. Locascio, "Temperature measurement in microfluidic systems using a temperature-dependent fluorescent dye," *Analytical chemistry*, vol. 73, no. 17, pp. 4117–4123, 2001.

[46] B.-J. Kim, Y. Z. Liu, and H.-J. Sung, “Micro piv measurement of two-fluid flow with different refractive indices,” *Measurement science and technology*, vol. 15, no. 6, p. 1097, 2004.

[47] V. Talimi, Y. Muzychka, and S. Kocabiyik, “A review on numerical studies of slug flow hydrodynamics and heat transfer in microtubes and microchannels,” *International Journal of Multiphase Flow*, vol. 39, pp. 88–104, 2012.

[48] R. Gupta, D. F. Fletcher, and B. S. Haynes, “On the cfd modelling of taylor flow in microchannels,” *Chemical Engineering Science*, vol. 64, no. 12, pp. 2941–2950, 2009.

[49] K. Fukagata, N. Kasagi, P. Ua-arayaporn, and T. Himeno, “Numerical simulation of gas–liquid two-phase flow and convective heat transfer in a micro tube,” *International Journal of Heat and Fluid Flow*, vol. 28, no. 1, pp. 72–82, 2007.

[50] Z. Dai, Z. Guo, D. F. Fletcher, and B. S. Haynes, “Taylor flow heat transfer in microchannels—unification of liquid–liquid and gas–liquid results,” *Chemical Engineering Science*, vol. 138, pp. 140–152, 2015.

[51] V. Talimi, Y. Muzychka, and S. Kocabiyik, “Slug flow heat transfer in square microchannels,” *International Journal of Heat and Mass Transfer*, vol. 62, pp. 752–760, 2013.

[52] J. Zhang, D. F. Fletcher, and W. Li, “Heat transfer and pressure drop characteristics of gas–liquid taylor flow in mini ducts of square and rectangular cross-sections,” *International Journal of Heat and Mass Transfer*, vol. 103, pp. 45–56, 2016.

[53] A. Günther, M. Jhunjhunwala, M. Thalmann, M. A. Schmidt, and K. F. Jensen, “Micromixing of miscible liquids in segmented gas- liquid flow,” *Langmuir*, vol. 21, no. 4, pp. 1547–1555, 2005.

[54] Z. Che, T. N. Wong, N.-T. Nguyen, and C. Yang, “Three dimensional features of convective heat transfer in droplet-based microchannel heat sinks,” *International Journal of Heat and Mass Transfer*, vol. 86, pp. 455–464, 2015.

[55] S. K. R. Cherlo, S. Kariveti, and S. Pushpavanam, “Experimental and numerical investigations of two-phase (liquid- liquid) flow behavior in rectangular microchannels,” *Industrial & Engineering Chemistry Research*, vol. 49, no. 2, pp. 893–899, 2009.

[56] Q. Li, K. H. Luo, Q. Kang, Y. He, Q. Chen, and Q. Liu, “Lattice boltzmann methods for multiphase flow and phase-change heat transfer,” *Progress in Energy and Combustion Science*, vol. 52, pp. 62–105, 2016.

[57] Z. Che, N.-T. Nguyen, T. N. Wong *et al.*, “Analysis of chaotic mixing in plugs moving in meandering microchannels,” *Physical Review E*, vol. 84, no. 6, p. 066309, 2011.

[58] M. Kashid, I. Gerlach, S. Goetz, J. Franzke, J. Acker, F. Platte, D. Agar, and S. Turek, “Internal circulation within the liquid slugs of a liquid- liquid slug-flow capillary microreactor,” *Industrial & engineering chemistry research*, vol. 44, no. 14, pp. 5003–5010, 2005.

[59] A. Abdollahi, R. N. Sharma, and A. Vatani, “Fluid flow and heat transfer of liquid-liquid two phase flow in microchannels: A review,” *International Communications in Heat and Mass Transfer*, vol. 84, pp. 66–74, 2017.

[60] Z. Che, T. N. Wong, N.-T. Nguyen, and C. Yang, “Asymmetric heat transfer in liquid–liquid segmented flow in microchannels,” *International Journal of Heat and Mass Transfer*, vol. 77, pp. 385–394, 2014.

[61] M. Shojaeian and A. Koşar, “Convective heat transfer of non-newtonian power-law slip flows and plug flows with variable thermophysical properties in parallel-plate and circular microchannels,” *International Journal of Thermal Sciences*, vol. 100, pp. 155–168, 2016.

[62] M. Shojaeian, M. Yildiz, and A. Koşar, “Heat transfer characteristics of plug flows with temperature-jump boundary conditions in parallel-plate channels and concentric annuli,” *International Journal of Thermal Sciences*, vol. 84, pp. 252–259, 2014.

[63] Y. Muzychka, E. Walsh, and P. Walsh, “Simple models for laminar thermally develop-

ing slug flow in noncircular ducts and channels," *Journal of Heat Transfer*, vol. 132, no. 11, p. 111702, 2010.

[64] Z. Che, T. N. Wong, and N.-T. Nguyen, "An analytical model for a liquid plug moving in curved microchannels," *International Journal of Heat and Mass Transfer*, vol. 53, no. 9-10, pp. 1977–1985, 2010.

[65] C. Meyer, M. Hoffmann, and M. Schlüter, "Micro-piv analysis of gas–liquid taylor flow in a vertical oriented square shaped fluidic channel," *International Journal of Multiphase Flow*, vol. 67, pp. 140–148, 2014.

[66] Cramer and Gabriel, *Introduction a l'analyse des lignes courbes algebriques par Gabriel Cramer...* chez les freres Cramer & Cl. Philibert, 1750.

[67] W. E. Langlois and M. O. Deville, *Slow viscous flow.* Springer, 1964.

[68] T. L. Bergman, F. P. Incropera, D. P. DeWitt, and A. S. Lavine, *Fundamentals of heat and mass transfer.* John Wiley & Sons, 2011.

Appendix

Appendix A

Correlations for long plugs ($\beta > 2$) in chapter 2

The analysis in this section will focus on long plugs, which have relatively large aspect ratios, i.e. $\beta > 2$. Because as shown in chapter 2, the influence of β upon the volume ratio of the two vortexes $\hat{V}_{in,v}/\hat{V}_{out,v}$ and the ratio of maximum and minimum stream functions $|\hat{\psi}_{min}/\hat{\psi}_{max}|$ are negligible when $\beta > 2$. Thus these two parameters are dependent on η only. We will derive the correlation for them when $\beta > 2$ with the help of the following figure,

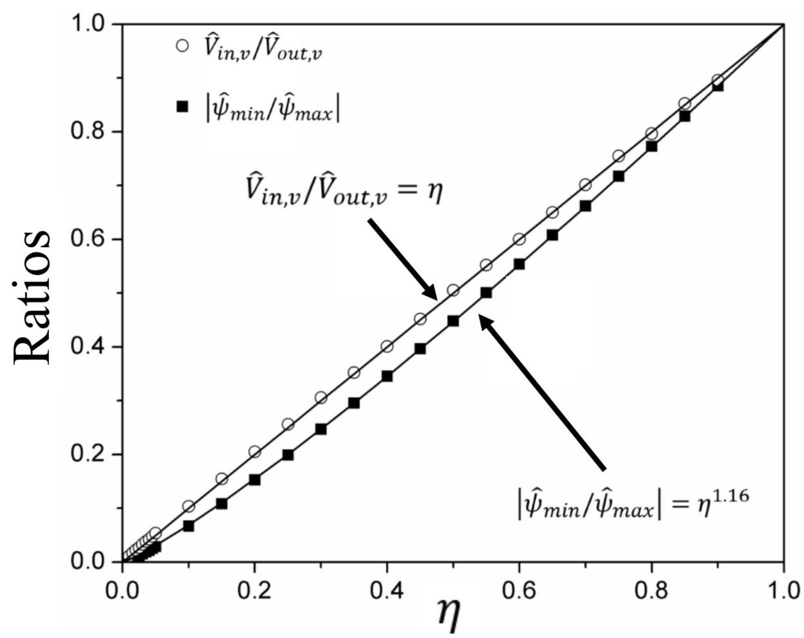

Figure A.1: The volume ratio of two vortexes $\hat{V}_{in,v}/\hat{V}_{out,v}$, and the ratio of max/min stream functions $|\hat{\psi}_{min}/\hat{\psi}_{max}|$ when $\beta > 2$. The solid lines are the correlations for the points obtained from analytical results in chapter 2.

The solid lines in fig. A.1 are the correlation made. The volume ratio $\hat{V}_{in,v}/\hat{V}_{out,v}$ shows a relationship with the radius ratio of the channel η, which is

$$\hat{V}_{in,v}/\hat{V}_{out,v} = \eta. \tag{A.1}$$

Similarly, fig. A.1 shows the ratio of max/min stream functions $|\hat{\psi}_{min}/\hat{\psi}_{max}|$ varies with η as below,

$$|\hat{\psi}_{min}/\hat{\psi}_{max}| = \eta^{1.16}. \tag{A.2}$$

To further derive the correlations, define the total volumetric recirculation rate of the plug using the summation of those of two vortexes, which is $|\hat{\psi}_{max}| + |\hat{\psi}_{min}| = \hat{\psi}_{max} - \hat{\psi}_{min}$.

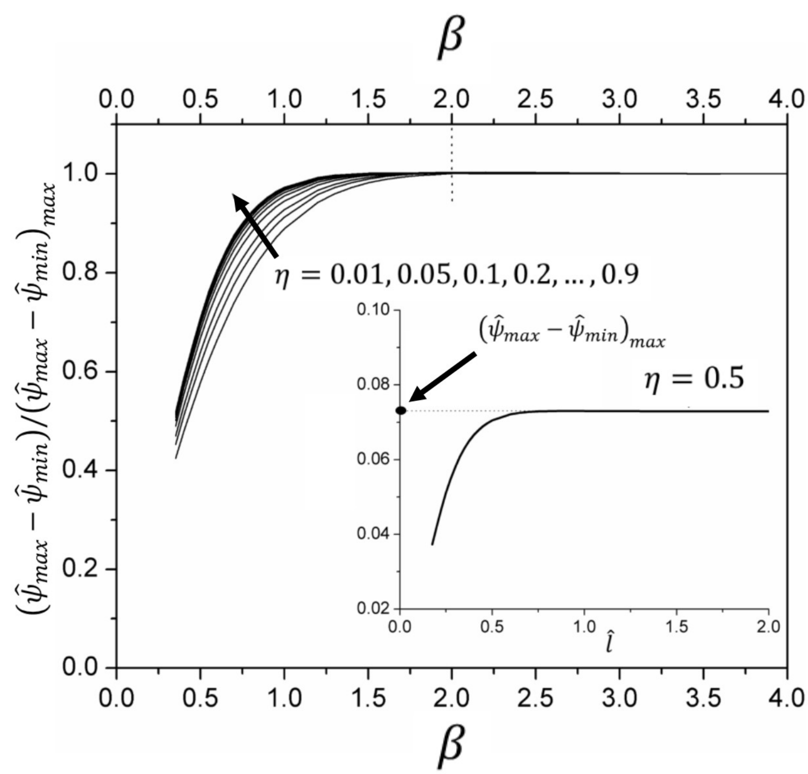

Figure A.2: The total of volumetric recirculation rate of two vortexes $\hat{\psi}_{max} - \hat{\psi}_{min}$ becomes independent of β when $\beta > 2$.

In the small subplot in fig. A.2 the total recirculation rate grows and then becomes stable when plug length $\hat{l}$ increases. This stable value is marked with a subscript $_{max}$. The ratio $(\hat{\psi}_{max} - \hat{\psi}_{min})/(\hat{\psi}_{max} - \hat{\psi}_{min})_{max}$ becomes infinity close to 1 as well when $\beta > 2$. Hence, $\hat{\psi}_{max} - \hat{\psi}_{min}$ can also be correlated using η only when $\beta > 2$.

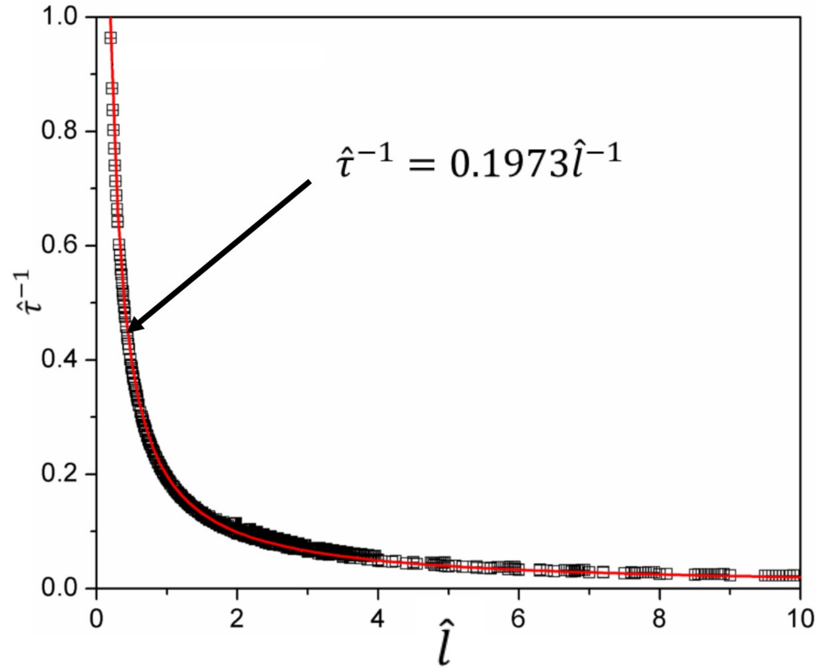

Figure A.3: The refresh frequency defined in eq. (A.3). The solid lines are the correlations for the points obtained from analytical results in chapter 2.

Define the refresh period $\hat{\tau}$ as below, which is the ratio between the volume of the whole plug $\hat{V}_{plug}$ and the total recirculation rate $\hat{\psi}_{max} - \hat{\psi}_{min}$, here the result in eq. (2.40) is used,

$$\hat{\tau} = \frac{\hat{V}_{plug}}{\hat{\psi}_{max} - \hat{\psi}_{min}} = \frac{(1-\eta^2)\hat{l}}{2(\hat{\psi}_{max} - \hat{\psi}_{min})}. \tag{A.3}$$

If $\hat{\tau}^{-1}$ is plotted against the plug length $\hat{l} = \beta(1-\eta)$ for multiple cases obtained from chapter 2 with $\beta > 2$ as in fig. A.3, it can be clearly concluded that $\hat{\tau}^{-1}$ is dependent on $\hat{l}$ only. A simple inverse model is adopted here,

$$\hat{\tau}^{-1} = 0.1973\hat{l}^{-1}. \tag{A.4}$$

Then the total recirculation rate $\hat{\psi}_{max} - \hat{\psi}_{min}$ is concluded from eqs. (A.3) and (A.4),

$$\hat{\psi}_{max} - \hat{\psi}_{min} = 0.0986(1-\eta^2). \tag{A.5}$$

The correlations for $\hat{\psi}_{max/min}$ are concluded by combining eqs. (A.2) and (A.5),

$$\hat{\psi}_{max} = \frac{0.0986(1-\eta^2)}{1+\eta^{1.16}}, \tag{A.6}$$

$$\hat{\psi}_{min} = -\frac{0.0986(1-\eta^2)\eta^{1.16}}{1+\eta^{1.16}}. \tag{A.7}$$

An important set of parameters for quantifying vortexes, the averaged recirculation flux by the two vortexes $(\hat{r}\hat{\bar{u}}_r)_{out,v/in,v}$ are defined in chapter 2. Thus they can be calculated by combining eqs. (2.42) and (A.6) or eqs. (2.42) and (A.7), respectively.

$$(\hat{r}\hat{\bar{u}}_r)_{out,v} = \frac{0.1973(1-\eta^2)}{(1+\eta^{1.16})\hat{l}}, \tag{A.8}$$

$$(\hat{r}\hat{\bar{u}}_r)_{in,v} = -\frac{0.1973(1-\eta^2)\eta^{1.16}}{(1+\eta^{1.16})\hat{l}}. \tag{A.9}$$

A comparison between the analytical results in chapter 2 and these from correlations eqs. (A.5) to (A.7) for long plugs ($\beta > 2$) is plotted as below. For the inner vortex, the correlation in eq. (A.7) shows good agreement with all analytical results. For the outer vortex, the correlation in eq. (A.7) agrees well with the data points except for plugs with small inner radius ($\eta <\sim 0.2$). As a result, eq. (A.5) predicts the total plug circulation rate with good accuracy except for small inner radius ($\eta <\sim 0.2$). Overall the correlations can well predict parameters such as maximum or minimum stream functions and the averaged recirculation flux, the appropriate range for applying these correlations is $\beta > 2 \wedge \eta >\sim 0.2$.

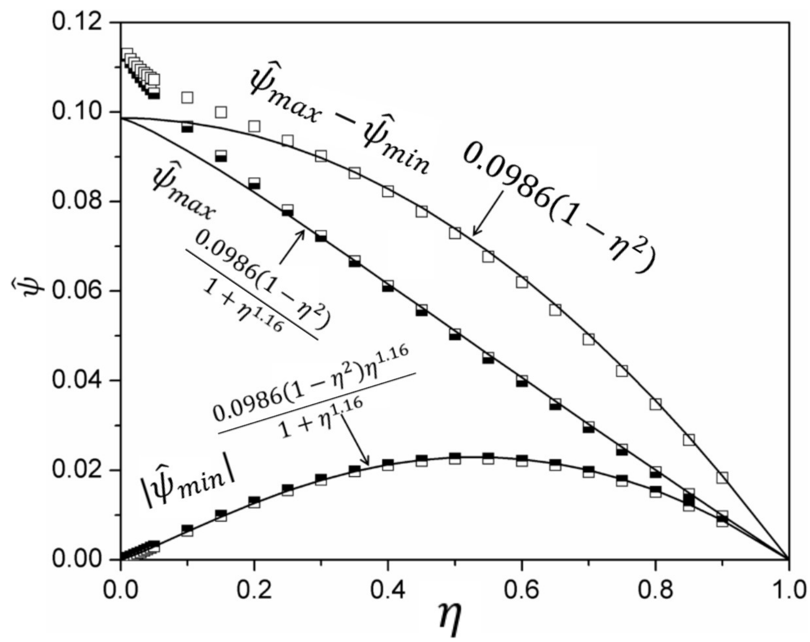

Figure A.4: Comparison between the correlation and the analytical results. The solid lines are the correlations for the points obtained from analytical results in chapter 2.